CRITERIA 3

3.7.1 – Collaborative Activities

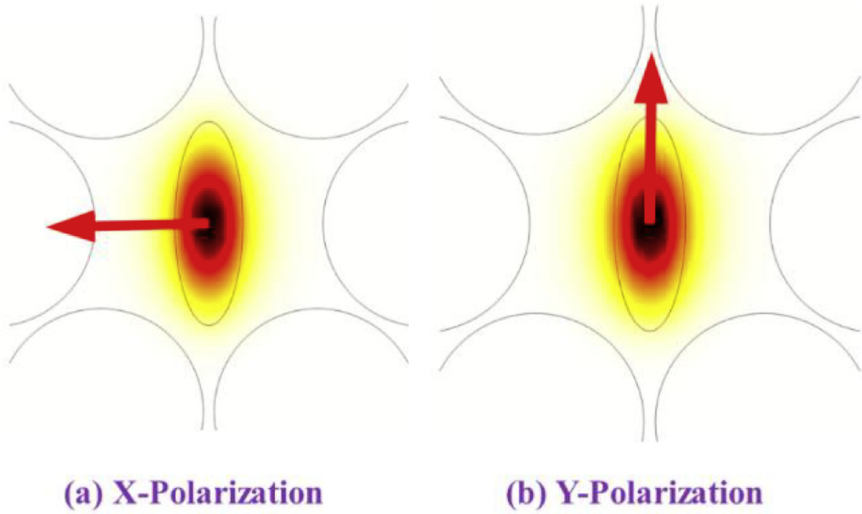

Fig. 2. The mode field distributions of the proposed structure (a) x-polarization and (b) y-polarization at operating wavelength λ = 1.55 µm.

cladding region gives high value of nonlinear coefficient. For all optical signal processing, super continuum generation, high power applications highly nonlinear PCFs are emergent. Dimensionless parameter NA can be estimated by the following equation (5)

$$Numerical\ Aperture\ (NA) = \sin\theta \approx \left[1 + \frac{\pi A_{eff}}{\lambda^2}\right]^{-\frac{1}{2}} \tag{5}$$

NA is indispensable is also for non-invasive medical imaging as well as OCT and many more practical applications.

The base material is silica. Due to some molecular density and non-uniform geometric configuration there exists some microscopic variation. Whereby, it produces some scattering loss as a result of such types of configuration light are scattered. The total loss of any fiber is led by the scattering loss. Total loss of fiber is a kind of channel impairment also plays a vital role. This impairment reduces the signal strength. The scattering loss can be calculated using the following equation no. (6) as follows for the proposed PCF

$$\alpha_R = C_R \times \left(\frac{1}{\lambda}\right)^4 \tag{6}$$

Where, C_R is the scattering coefficient of the background material and is the range from 0.8×10^{-5} to 1.0×10^{-5} (dB/cm). (µm)^4. The value of C_R is chosen 1.0×10^{-5} (dB/cm) (µm) ^{4} here in the investigation process.

Nonlinearity distributions are shown in Fig. 3 from 0.5 µm to 2.5 µm wavelength. The structure demonstrates extensive nonlinearity due to its small effective mode area. High nonlinear refractive index material gives the direct impact on enhancing nonlinearity. Confinement of light in the core region is proportional to the estimation of the nonlinearity. Nonlinearity of 33280.80352 $W^{-1} km^{-1}$ and 32813.42695 $W^{-1} km^{-1}$ are found at the same wavelength λ = 1.00 µm for both x-polarization and y-polarization, respectively. Maximum nonlinearity is found for x-polarization of 128873.1183 $W^{-1} km^{-1}$ and for y-polarization of 152134.1052 $W^{-1} km^{-1}$ at 0.5 µm. The estimated nonlinearity is undoubtedly superior to the previously reported standard article [11,13]. Details are shown in Table 1.

In Fig. 4, it is demonstrated that the effective area is small as expected for the proposed structure. From the conventional fiber this value is exceptionally smaller. The effective area of the proposed structure is small in the order of 10^{-13}. For the proposed structure, effective area of $9.73 \times 10^{-13}\ m^2$ and $8.89 \times 10^{-13}\ m^2$ are found for x-polarization and y-polarization, respectively, at the wavelength of 0.8 µm. In Fig. 5, Scattering loss is examined perspective to wavelength changes. It reveals that the light is tightly confined through the core and

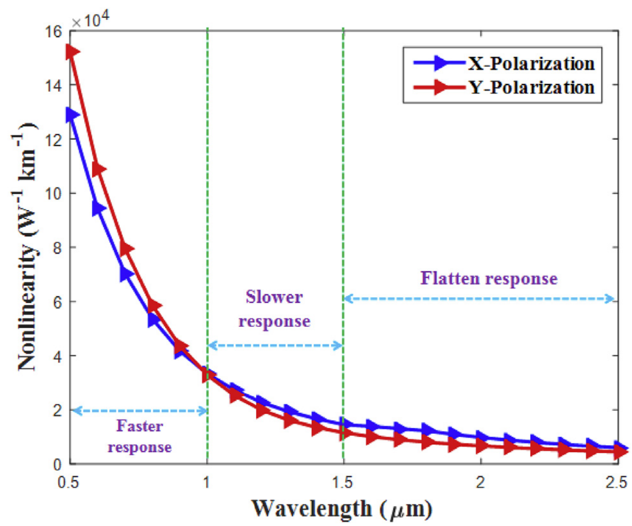

Fig. 3. Nonlinearity is a function of wavelength for both two fundamental orthogonal polarization modes (blue curve) y-polarization and (red curve) x-polarization. (For interpretation of the references to colour in this figure legend, the reader is referred to the Web version of this article.)

Table 1
Comparison among present work and recently published standard articles with essential optical parameters by controlling optical wavelength.

PCFs	Wavelength λ (µm)	Nonlinearity ($W^{-1} km^{-1}$)	NA	Confinement loss (dB/m)	Scattering loss (dB/km)
Ref [10]	1.40	7.28×10^4	–	–	–
Ref. [17]	1.00	6.34×10^4	0.56	–	1.33×10^{-8}
Ref [21]	0.50	2.75×10^2	–	–	–
Ref [22]	1.00	2.49×10^4	–	–	–
Ref [23]	0.65	9.85×10^3	–	–	–
Ref [24]	0.85	6.95×10^4	–	–	–
This work	0.50	1.52×10^5	0.36	1.47×10^{-5}	2.21×10^{-7}

induces low scattering loss. The low scattering loss is founded for the proposed structure of 1.64×10^{-07} dB/km and 1.65×10^{-07} dB/km for x-polarization and y-polarization, respectively, at the wavelength of 0.5 µm.

The power fraction inside core region of the proposed fiber is a function of controlling wavelength, which has been plotted in Fig. 6. From the figure, it is nicely visualized that almost maximum power goes

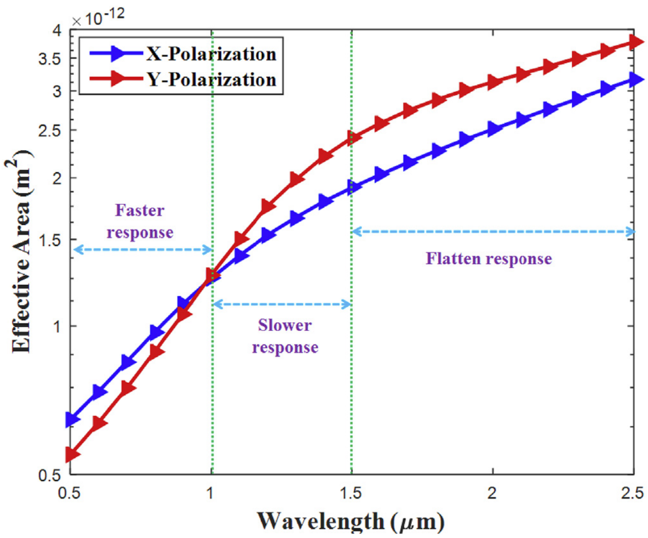

Fig. 4. Effective area or effective mode area as a function of wavelength for both two fundamental orthogonal polarization modes (blue curve) x-polarization and (red curve) y-polarization. (For interpretation of the references to colour in this figure legend, the reader is referred to the Web version of this article.)

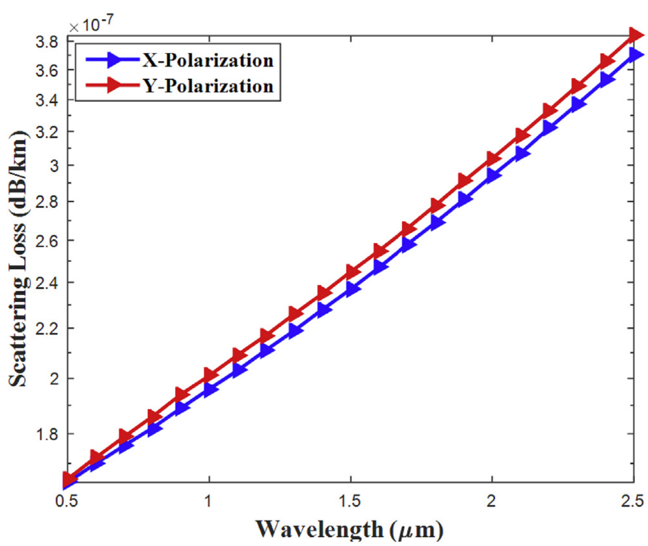

Fig. 5. Scattering loss as a function of wavelength for both two fundamental orthogonal polarization modes (blue curve) x-polarization and (red curve) y-polarization. (For interpretation of the references to colour in this figure legend, the reader is referred to the Web version of this article.)

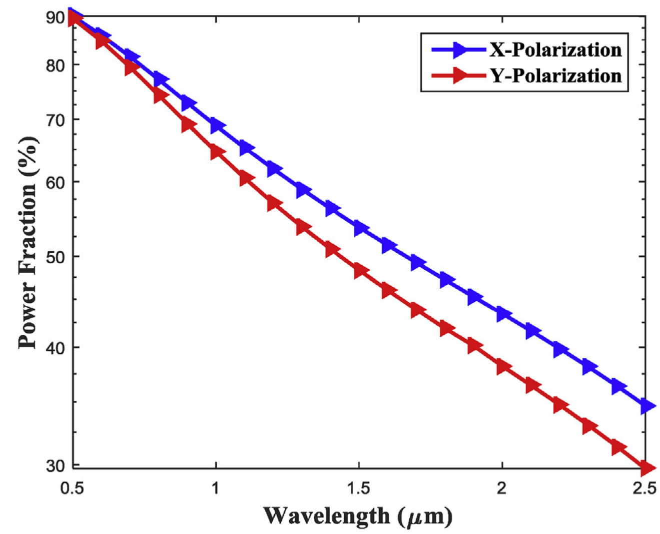

Fig. 6. Power distribution fractions of mode power as a function of wavelength for both two fundamental orthogonal polarization modes (blue curve) x-polarization and (red curve) y-polarization. (For interpretation of the references to colour in this figure legend, the reader is referred to the Web version of this article.)

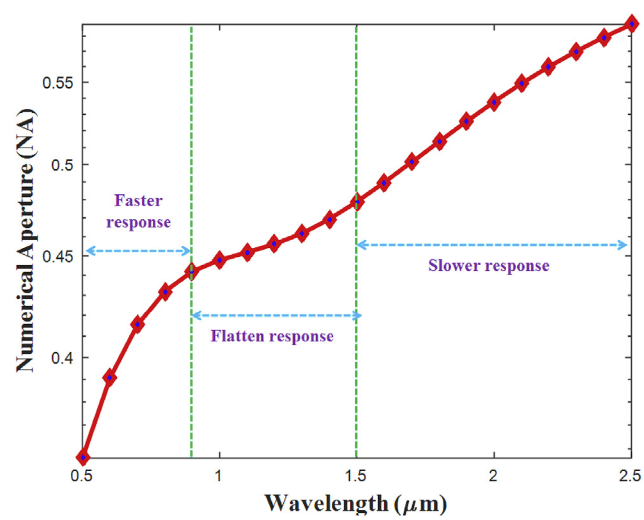

Fig. 7. Numerical aperture as a function of optical wavelength from 0.5 μm to 2.5 μm where the horizontal x axis, presenting wavelength and vertical y axis presenting NA.

into the core region. It is also notified that the relation of power fraction and wavelength is inversely proportional. For the proposed structure, maximum power goes into the core region at 0.5 μm wavelength with lower effective area and induces maximum nonlinearity. Fig. 7 demonstrates the highest NA of 0.57 and 0.59 for optimum structure for x-polarization and y-polarization respectively at 2.5 μm wavelength. The NA of more than 0.40 in silica based PCF is very rare. But, the proposed PCF shows the NA of more than 0.55. Moreover high values of NA are very desirable for many aspects of optical applications. So, this value is highly comparable with previously reported results [18–20]. The proposed PCF is also a potential candidate for medical imaging applications. Fig. 8 expresses the confinement loss of the proposed fiber which is found for the variation of the wavelength. The index contrasts between cladding and core of the proposed fiber is inconsiderable which demonstrates that, tightly confinement of light through the core and induces negligible confinement loss. Moreover, a comparison table has been presented between previously reported PCFs with proposed PCF.

From the above mentioned Table 1, it is transparent that the proposed PCF is a worthy candidate than all the PCF which are previously reported. If such type of PCF is manufactured and installed then the optical system will get a new level of excellence. Aiming to the fabrication intention essentials steps are strictly maintains, these steps are given below stepwise. Firstly, the PCF is fabricated with all air holes with the help of sol gel technique. After that a very popular chemical reaction (i.e. magnesiothermic reduction) is took place with the help of Magnesium (Mg). It extracts the oxygen for the silica (silicon dioxide SiO_2) and thereby produces silicon PCF. Finally, the chemical vapor deposition technique is employed to fill the core hole with silicon nano crystal.

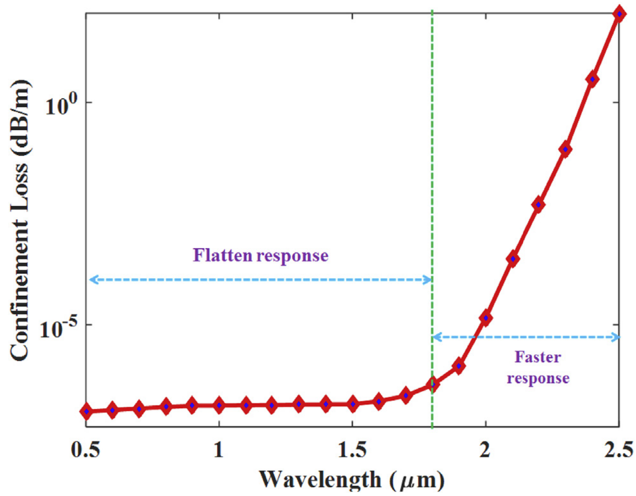

Fig. 8. Confinement loss as a function of wavelength for the proposed PCF structure.

4. Conclusion

With high nonlinearity and high NA, a novel design of circular hybrid hexagonal photonic crystal fiber (CH-PCF) is presented. The numerical results strongly demonstrate that the reported microstructure design offers high nonlinearity of 128873.1183 $W^{-1}km^{-1}$ and 152134.1052 $W^{-1}km^{-1}$ for both x-polarization and y-polarization, respectively, at the operating wavelength of 0.5 μm. At the operating wavelength of 2.50 μm, the highest numerical aperture of 0.57 and 0.59 are gained for both x-polarization and for y-polarization, respectively. In the session of the investigation module low loss is observed from the same structure. So, the proposed PCF will be a strong candidate in super continuum generation, optical parametric amplification, wavelength conversion, mid infrared fiber lasers, slow light generation, and nonlinear optics and so on.

Source of funding

No financial support was provided to any of the authors in the creation/writing of this research manuscript.

Competing interest

The authors declare that all the authors have no competing of interest.

Acknowledgment

The authors are grateful who have participated in this research. There is no financial supports for this research.

References

[1] A. Wang, B. Zhang, J. Hou, H. Wei, W. Tong, J. Luo, Z. Zhang, IEEE Photon. Technol. Lett. 24 (2012) 143–145.
[2] Y.P. Yatsenko, A.D. Pryamikov, J. Optic. Pure Appl. Optic. 9 (2007) 716.
[3] K. Goudarzi, A. Mir, Majlesi Journal of Electrical Engineering 9 (2015) 37–41.
[4] K. Goodarzi, A. Mir, Infrared Phys. Technol. 68 (2015) 193–196.
[5] F. Ali, A. Mir, Z. Sharifpour, Appl. Surf. Sci. 453 (2018) 358–364.
[6] A. Wang, B. Zhang, J. Hou, H. Wei, W. Tong, J. Luo, Z. Zhang, IEEE Photon. Technol. Lett. 24 (2012) 143–145.
[7] L. Tian, L. Wei, F. Guoying, Optic Commun. 334 (2015) 196–202.
[8] J.M. Hsu, Optic Commun. 361 (2016) 104–109.
[9] N. Karasawa, Optic Commun. 364 (2016) 1–8.
[10] J. Liao, T. Huang, Opt. Fiber Technol. 22 (2015) 107–112.
[11] T. Huang, J. Liao, S. Fu, M. Tang, P. Shum, D. Liu, IEEE Photonics Journal 6 (2014) 1–7.
[12] P. Li, J. Zhao, Optic Express 21 (2013) 5232–5238.
[13] J. Liao, J. Sun, M. Du, Y. Qin, IEEE Photon. Technol. Lett. 26 (2014) 380–383.
[14] M.N. Amin, M. Faisal, Appl. Optic. 55 (2016) 10030–10037.
[15] J. Hou, D. Bird, A. George, S. Maier, B.T. Kuhlmey, J.C. Knight, Optic Express 16 (2008) 5983–5990.
[16] K. Saitoh, K. Kakihara, S. Varsheney, M. Koshiba, Conference on Lasers and Electro-Optics (CLEO) (2008) 1–2.
[17] B.K. Paul, M.G. Moctader, K. Ahmed, M.A. Khalek, Results Phys. 10 (2018) 374–378.
[18] S. Sen, M.S. Islam, B.K. Paul, M.I. Islam, S. Chowdhury, K. Ahmed, S. Asaduzzaman, J. Opt. Commun. (2017), https://doi.org/10.1515/joc-2017-0104.
[19] J. Sultana, M.S. Islam, M.R. Islam, D. Abbott, Electron. Lett. 54 (2017) 61–62.
[20] S. Chowdhury, S. Sen, K. Ahmed, S. Asaduzzaman, Optik 142 (2017) 541–549.
[21] X. Li, Z. Xu, W. Ling, P. Liu, Appl. Optic. 53 (2014) 6682–6687.
[22] B. Jiten, T.S. Saini, R.K. Sinha, J. Nanophotonics 11 (2017) 036002.
[23] S. Revathi, S. Inabathini, R. Sandeep, Opt. Appl. 45 (2015) 15–24.
[24] S. Revathi, S.R. Inbathini, R.A. Saifudeen, Adv. Optoelectron. 2014 (2014) 4643911–6.

Optical Fiber Technology 45 (2018) 115–121

Contents lists available at ScienceDirect

Optical Fiber Technology

journal homepage: www.elsevier.com/locate/yofte

Detection of moisture content in transformer oil using platinum coated on D-shaped optical fiber

S.F.A.Z. Yusoff[a], M.H. Mezher[a], I.S. Amiri[b,c,*], N. Ayyanar[d], D. Vigneswaran[e], H. Ahmad[a], R. Zakaria[a]

[a] Photonics Research Centre, Department of Physics, Faculty of Science, University of Malaya, Lembah Pantai, 50603 Kuala Lumpur, Malaysia
[b] Computational Optics Research Group, Advanced Institute of Materials Science, Ton Duc Thang University, Ho Chi Minh City, Viet Nam
[c] Faculty of Applied Sciences, Ton Duc Thang University, Ho Chi Minh City, Viet Nam
[d] Department of Electronics and Communication Engineering, National Institute of Technology, Tiruchirappalli 620015, India
[e] Department of Electronics and Communication Engineering, Sri Krishna College of Technology, Coimbatore 641 042, India

ARTICLE INFO

Keywords:
Power response
Transformer oil
Platinum coating
D-shaped optical fiber

ABSTRACT

The presence of moistures in transformer deteriorates transformer insulation. These effects decrease both electrical and mechanical strength of the transformer. Water in transformer oil also brings the risk of bubble formation when desorption of water increases the local concentration of gases in the oil. The water content in the insulating oil (or transformer oil) needs to be less than 10 ppm at normal temperature or contradictory, it will affect the efficiency of the power transformer system. Here, we report a D-shaped optical fiber sensor coated with a platinum thin layer with a thickness of 25 nm was designed to detect the response of transverse electric field (TE) power towards the content of moisture in the insulating oil. A Simulative based investigation using COMSOL Multiphysics has also been carried out to study the relation between analyte on the materials at different refractive index and the simulation study follows the finite element method (FEM). Four samples of aged oil were tested from actual transformer oil with different values of water contents of 15 ppm, 16 ppm, 18 ppm, and 21 ppm. The oil samples were dropped on the sensing region of the fiber and resulting in the drop of TE power from the initial value. It was observed that higher values of water percentages in the oil caused large fluctuations in TE power. On top of that, the changes in TE power show that the sensor is having fast response and good sensitivity.

1. Introduction

Power of transformer is one of the important elements in electrical transmission and distribution (T&D) system. Monitoring the function of a high-power transformer has become crucial and the maintenance of the transformer need to be kept right since the performance of the transformer is a vital element in the system. Dielectric strength or breakdown voltage of the insulating oil or transformer oil, in particular, is a critical parameter in transformer system and it is important for engineers and researchers to cunning that the dielectric strength of new transformer oil is several times better than the aged and contaminated oil. The incremental of energy used has become a demand among the society nowadays and exposes transformers to excessive stress and overloads, which resulting in the low integrity and performance of the transformer in a long run. The importance of moisture presence in oil systems has been recognized since the 1920s.

During the operation of the transformer, there are several factors that will influence the gradual production which include the moisture contamination [1,2], impurities particles, acidity and also pressure in the insulating oil [3,4]. In electricity grid, the power transformer is the most important and costly elements, where the use of power transformer will facilitate the efficient transmission and distribution of the electricity with respect to the different level of voltage. The reliability of the entire network can be affected by any malfunction of the power transformer element, where this may have a significant economic impact on the system [5,6]. Thus, it is important to maintain the level of moisture in the insulation system as it will slow down the aging process of the paper insulation and conserve the system. In order to control the quality of insulating oil, a periodic oil test is performed, following the international standards and a frequent maintenance need to be done which depend on the condition of the transformers. Another important monitoring process which is partial discharge (PD) measurement,

* Corresponding author at: Ton Duc Thang University, Ho Chi Minh City, Viet Nam.
E-mail address: irajsadeghamiri@tdt.edu.vn (I.S. Amiri).

https://doi.org/10.1016/j.yofte.2018.07.011
Received 3 April 2018; Received in revised form 25 May 2018; Accepted 2 July 2018

continuous voltage monitoring of AC and temperature control at certain points of the transformer still need to be characterized in order to affirm the performance of the system [7,8]. According to the international standards, units for water content are in mg of water per kg of oil or ppm for all types of transformers are based on the levels of a voltage of the transformers. New insulating oil normally has water content lower than 10 ppm at normal temperature. There are two main causes that alter the amount of water content in the insulating oil which is moisture activity with the environment and also moisture that generates due to chemical reactions.

A few years back, devices for moisture monitoring of transformer oil has become a trend among the researchers. An electrical moisture sensor was created based on the electrochemical techniques, but have a lot of drawbacks including low sensitivity and it tends to generate electromagnetic and noise interference, making them unhandy for online application [9]. Besides, since the electrochemical technique used to detect moisture need the existence of electrolytes so that the conduction of the system will be improved, the original transformer oil sample need to be modified which require complex extraction procedures [10]. Recently, fiber optic sensor has been designed to play an important role in the various important fields which includes environmental monitoring, medical diagnostic, food safety and security since they offered a great advantage of fast response, immune to electromagnetic interference and high sensitivity. Tae et al. reported the use of fiber optic sensor using Mach-Zehnder interferometry to monitor acoustic wave propagation and sound attenuation properties in aged transformer oil [11]. The use of the bare and bent optical fiber has been reported by S. Laskar [2], where the measurement of the refractive index and also the temperature of a transformer oil sample have been performed.

In this paper, D-shaped optical fiber with a platinum thin layer on top layer have been fabricated and numerically modeled with the help of finite element studies to observe the moisture contained in the transformer oil. The advantage of using side polished or D-shaped fiber is that the evanescent field of the fiber can be exposed to the surrounding which will create the sensing region easily. The platinum thin film is used since it is a noble metal which can act as catalysts that can react to the water adsorption [12]. In addition, platinum is considered as a vital element in fuel cell technology, since platinum can be functioned as electrocatalysts for oxygen reduction reaction and also fuel oxidation reaction [13]. Sensitivity and fast response are used to characterize the performance of the sensor.

2. Modeling of D-shaped fiber

To investigate the performance of the D-shaped optical fiber sensor, we modeled the simulation using the Finite Element Method (FEM) utilities of COMSOL Multiphysics software. The Maxwell's equations are presented as follow, where the electromagnetic field is existing in the optical fibers in the absence of the currents or any external electrical charges.

$$\nabla \times E(r,t) = -\frac{\partial B(r,t)}{dt} \tag{1}$$

$$\nabla \times H(r,t) = -J(r,t) + \frac{\partial D(r,t)}{dt} \tag{2}$$

$$\nabla .\, D(r,t) = \rho B(r,t) \tag{3}$$

$$\nabla .\, B(r,t) = 0 \tag{4}$$

The electric field is presented by E, the magnetic field is H, D is the electric flux density and the B is representing the magnetic induction field. The current density is defined by J, the charge density is ρ, where the spatial coordinate is shown by r and t is referring to the time.

The wave equation for the Fourier components for electric field stated as:

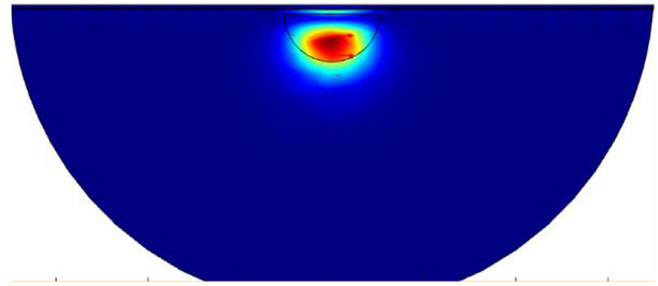

Fig. 1. Electric field distribution shows mode confinement in the core without platinum coating.

$$\nabla \times (\nabla \times E(r,\omega) - k_o{}^2[\varepsilon_r'(r,\omega)E(r,\omega)] = 0 \tag{5}$$

Similarly is the magnetic field:

$$\nabla \times [\varepsilon_r'(r,\omega)]^{-1}\nabla \times H(r,\omega) - k_0{}^2 H(r,\omega) = 0 \tag{6}$$

where $c = \sqrt{\varepsilon_0\mu_0}$ is the speed of light, and $k = \omega c^{-1}$ is defined as mode wave number. The complex term of the relative dielectric function is presented by $\varepsilon_r'(r,\omega) = \varepsilon_r(r,\omega) - j\sigma(r,\omega)/\omega\varepsilon_0$, where it constitutes of terms such as $\varepsilon_r$as the relative permittivity which is material-dependent (real valued) and the $\sigma(r,\omega)$ as the Ohmic conductivity of the material [14].

Both electric and magnetic fields change according to the angular frequency (Eqs. (5) and (6)) as well as the refractive index of the materials. Fig. 1 illustrated the intensity of the electric field using the function of "mode Analyses" from COMSOL Multiphysics for the structure of D-shape optical fiber. The mode field distribution of glass and analyte liquid is shown in Fig. 1 which gives the mode propagation of the incident energy with the function of wavelength. The wavelength of the light used was in the range of 1150–1350 nm. This study acknowledged the single-mode behavior propagation in the optical fiber. Fig. 2 depicts the mode propagation with the presence of platinum coating with a thickness of 25 nm. As the absorption property of the metal is greater than the glass material, it induces the more losses.

The sensing principle is followed by the coupling energy between the core and analyte layer. Since the analyte layer is taken on the top of the platinum layer, the TE mode coupling is considered between the core and platinum materials. When the coupling begins, the energy transfer has been started from the core to analyte layer and analyte to the core layer. When it couples at the particular wavelength, the maximum of absorption will be inferred and its corresponding wavelength is known as resonance wavelength. For different analytes, the resonance wavelength also varies on the right or left side shift in the absorption spectrum. After the coupling point, the core mode energy is shifted to the analyte layer and vice versa as shown in Fig. 3.

The loss spectrum (inset c) in Fig. 3 shows that shift occurring at a different position of a wavelength at 1240 nm for the refractive index of 1.44 and 1280 nm for material with refractive index 1.46. Each shift contains the maximum of loss value as well as resonance wavelength. Each point of resonance in the shift denotes that the energy transfer

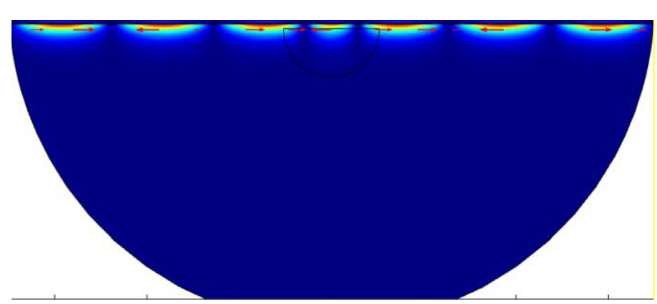

Fig. 2. Electric field distribution on mode confinement of the fiber core with a platinum coating with a thickness of 25 nm.

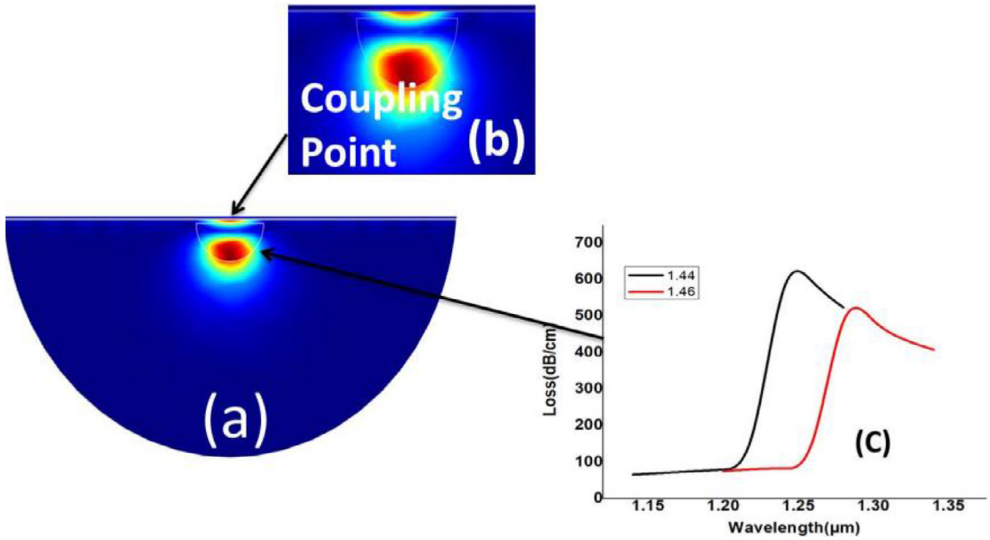

Fig. 3. (a) Mode coupling between the core and (b) mode coupling between analyte materials and (c) shows its loss spectrum with a different refractive index of 1.44 and 1.46.

between the core and analyte material is coupled. Such coupling points give the condition to satisfy the phase matching and sensitivity could be calculated. The following section includes the fabrication process of D shaped optical fiber and its experimental measures for oil moisture sensing.

Based on the simulation results obtained from COMSOL Multiphysics, the effective refractive index n_{eff} of the sensor can be computed, with the transmission coefficient T as the function of the wavelength λ, the external refractive index next with the thickness of the metal d_m, accordingly to the expression:

$$T(\lambda, n_{ext}, d_m) = e^{-2n_{eff}(,n_{ext},d)k_0L} \tag{7}$$

3. Optical sensor fabrication and experimental setup

3.1. Preparation of D-shaped optical fiber

A single mode optical fiber (SMF-28, Corning) was used to fabricate the D-shaped probe in this research. The diameter and refractive index of the core is 8.2 μm and 1.4682 respectively, while for the cladding, the diameter is 125 μm with lower refractive index compared to the core. The process of fabrication begins by placing the fiber on a clean glass slide using epoxy and was left in the open air to cure. After curing, the fiber that mounted on the slide was polished using fiber polishing film repeatedly. The polishing film was placed on the polisher machine in order to get a consistent and smooth polishing. Several repetitions of this stage may be needed as the fiber is polished manually and tend to break easily.

The determination of desired polishing depth was done manually by observing a leakage of red light during polishing process (Fig. 4). Red light is fed to the optical fiber during the process and the polishing is stopped once the light is observed at the polished core. The polished core is then observed by using an optical microscope to see the D-shaped structure of the fiber. The power loss of the fiber was measured before and after the polishing process in order to get a better estimation of the actual distance of polished core. The distance of polished core, h is estimated to be 20% of the core diameter to ensure the evanescent wave gets excited at the sensing region. The illustration of fiber optic attached on the glass slide is shown in Fig. 5.

3.2. Deposition of platinum (Pt) thin layer

After polishing process is complete, the D-shaped fiber was coated using sputter coating (Auto Fine Coater JFC-1600) technique. It is based on the fiber coated with a thin layer of metal, in this case, platinum on top of it, placed on a photoresist spinner inside a vacuum chamber and a constant speed is set as shown in Fig. 6. The coating was varied accordingly to the time of coating with a thickness of Pt set as 15 nm, 25 nm, and 35 nm. This technique produces a smooth and uniform coating on the fiber which the thickness can be adjusted by determining the coating period. The SEM image and illustration of Pt layer coated on the D-shaped fiber are shown in Fig. 7.

3.3. Experimental setup for sensor characterization

Fig. 8 shows the experimental setup used to characterize the fiber

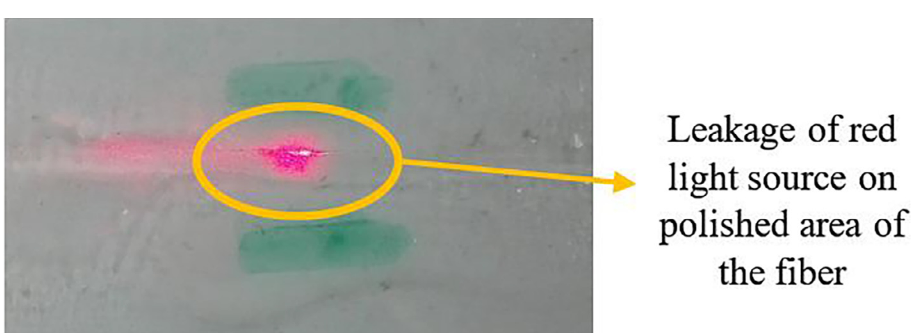

Fig. 4. Condition of the polished region on the fiber with leakage of red light on the polished area.

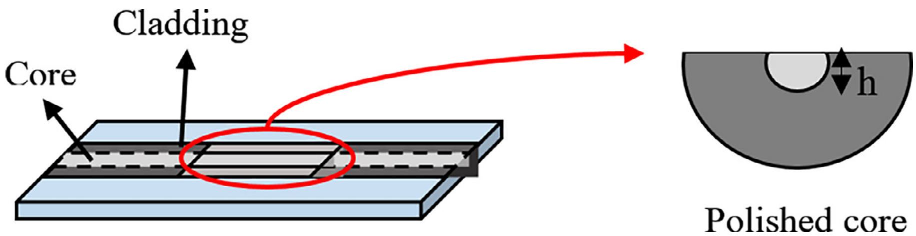

Fig. 5. Illustration of D-shaped fiber attached on a glass slide.

Fig. 6. Platinum (Pt) deposition using sputter coating machine.

optic sensor. Four samples of aged oil from actual transformer containing a different concentration of water (15 ppm, 16 ppm, 18 ppm and 21 ppm) were dropped (about 2590 µL) on the polished surface of the optical fiber. The samples were tested at appointed research laboratory that specifically does oil test for industrial companies in order to know the values of water content inside the aged oil. The transmittance was recorded to analyze the effect of the moisture towards changes on the measured power.

4. Results and discussion

Table 1 shows the analysis of Energy-dispersive X-ray spectroscopy (EDX) and based on the table, the presence of carbon (C), silicon (Si) and Oxygen (O) atoms represents the substrate used in this experiment, which is a D-shaped fiber optic. Moreover, the presence of platinum (Pt) by 11.79% proved that Pt particles had been successfully deposited on the fiber surface. Fig. 9 shows the changes in TE power after oil sample has been dropped on the sensing region of the fiber. Fig. 9 shows the comparison of the power drop of water content from bare fiber, 15 nm and 25 nm thickness of Pt coating. It is worth noted that there is no fluctuations could be recorded for the coating with a thickness of 35 nm due to there is no interaction of evanescent wave for the over-thick sample. Fig. 9 depicts transmission power measurement was carried out over a period of 100 s with 1-second intervals. All readings are normalized to the transmitted power of the Pt coating before transformer oil is applied. Fig. 9(a) shows the response of the D-shape fiber to the moisture in transformer oil samples without the coating was first measured. The result is shown in Fig. 9(a), which can be seen that the transmitted power decreases almost immediately after transformer oil droplet is applied onto the sensing region (at the10th second). This indicates that the refractive index of transformer oil is higher than the optical fiber core, thus causing light leakage into the transformer oil covering on the D-fiber region. Consequently, the output power loss through the cladded guide decreases [15]. Also, the transmitted power level of the D-fiber when transformer oil samples are applied shows large fluctuation over time, which is indicated by the vertical error bars in Fig. 10(a). This makes transmitted power change between transformer oil with different water content is not distinguishable. Fig. 9(b) shows the transformer oil taken fresh from its container is used as a reference. Upon application of the "fresh" transformer oil on the sensor, the transmitted power dropped by 2.0 dB. Transformer oil is applied at about 10 s after power measurement starts. It can be seen that the transmitted power decreases after the oil sample is applied onto the sensing region (at the 10th second). For transformer oil with 15–21 ppm of water content, transmission power decreases to a maximum and stabilizing at a lower power level after 10 s, respectively. Stabilized transmission power level increases with the amount of water content. Oil sample with 15 ppm of water content causes a transmission power decrease of 5.6 dB, while oil sample with 21 ppm of water content showed the largest decrease of 7.4 dB. As a comparison, the result

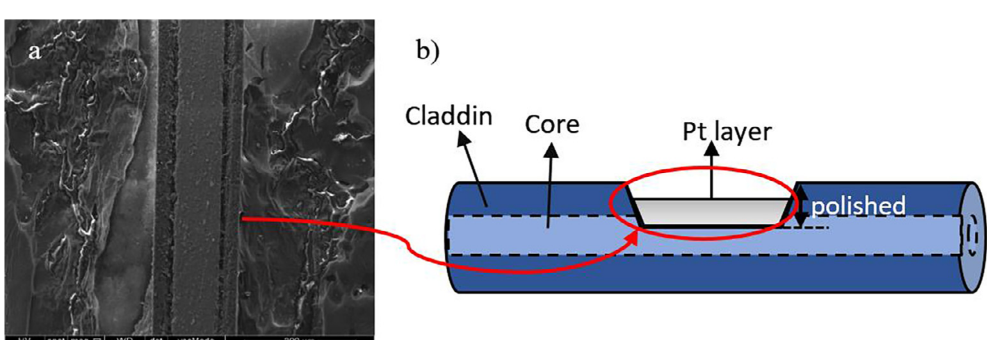

Fig. 7. a) SEM image of Pt thin layer coated on D-shaped fiber, b) Illustration of Pt thin layer on the D-shaped fiber.

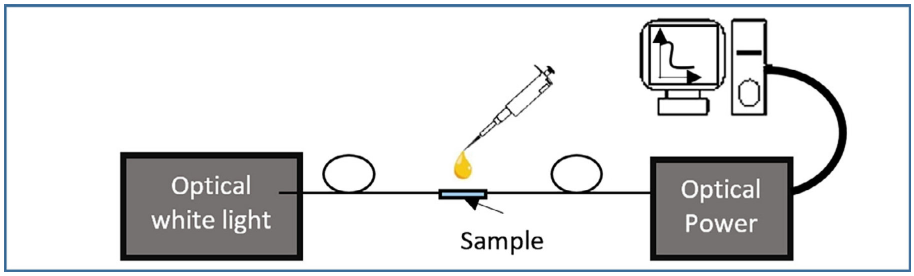

Fig. 8. Experimental setup for the sensor characterization.

Table 1
EDX analysis of platinum coated on the D-shaped fiber optic.

Element	Weight (%)
C (Carbon)	12.53
O (Oxygen)	44.15
Pt (Platinum)	11.79
Si (Silica)	31.53

indicates that water in the oil samples permeates into the Pt coating, which results in an increased transmission loss of the Pt-coated D-shaped fiber.

The decreasing in the power loss is believed to be due increasing the Pt thickness that reduces the leakage of the light, which allows the evanescent field of the fiber core to interact with the transformer oil inside the PT coating. Fig. 9(c) shows the change in transmitted power when oil sample was drop on the sensing region of the fiber. From the plots, the response time for transmitted power changed to lower values

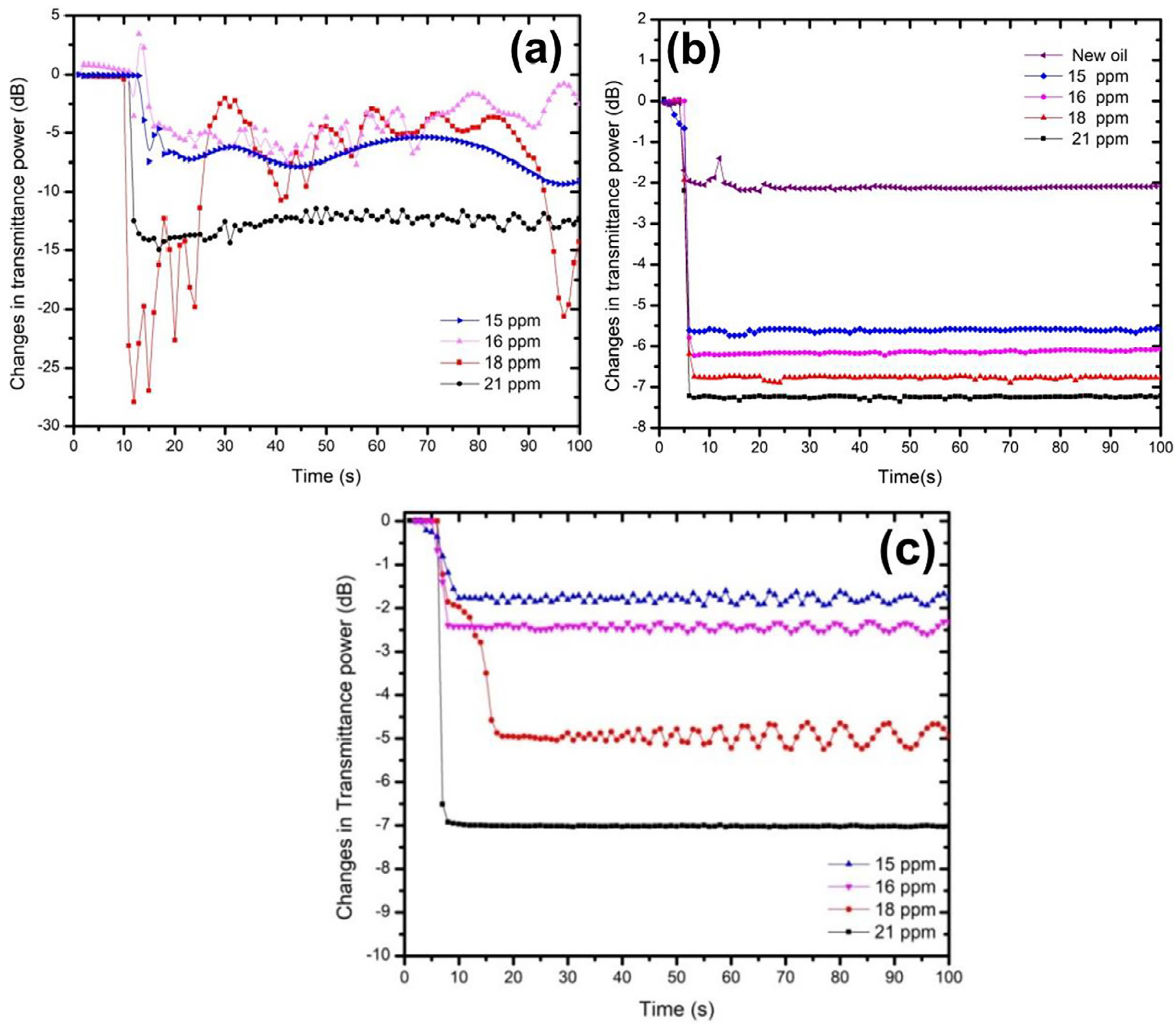

Fig. 9. Temporal response of transmitted power level to transformer oil samples with different dissolved water using (a) bare fiber without Pt coating (b) Pt thickness of 15 nm and (c) Pt thickness of 25 nm.

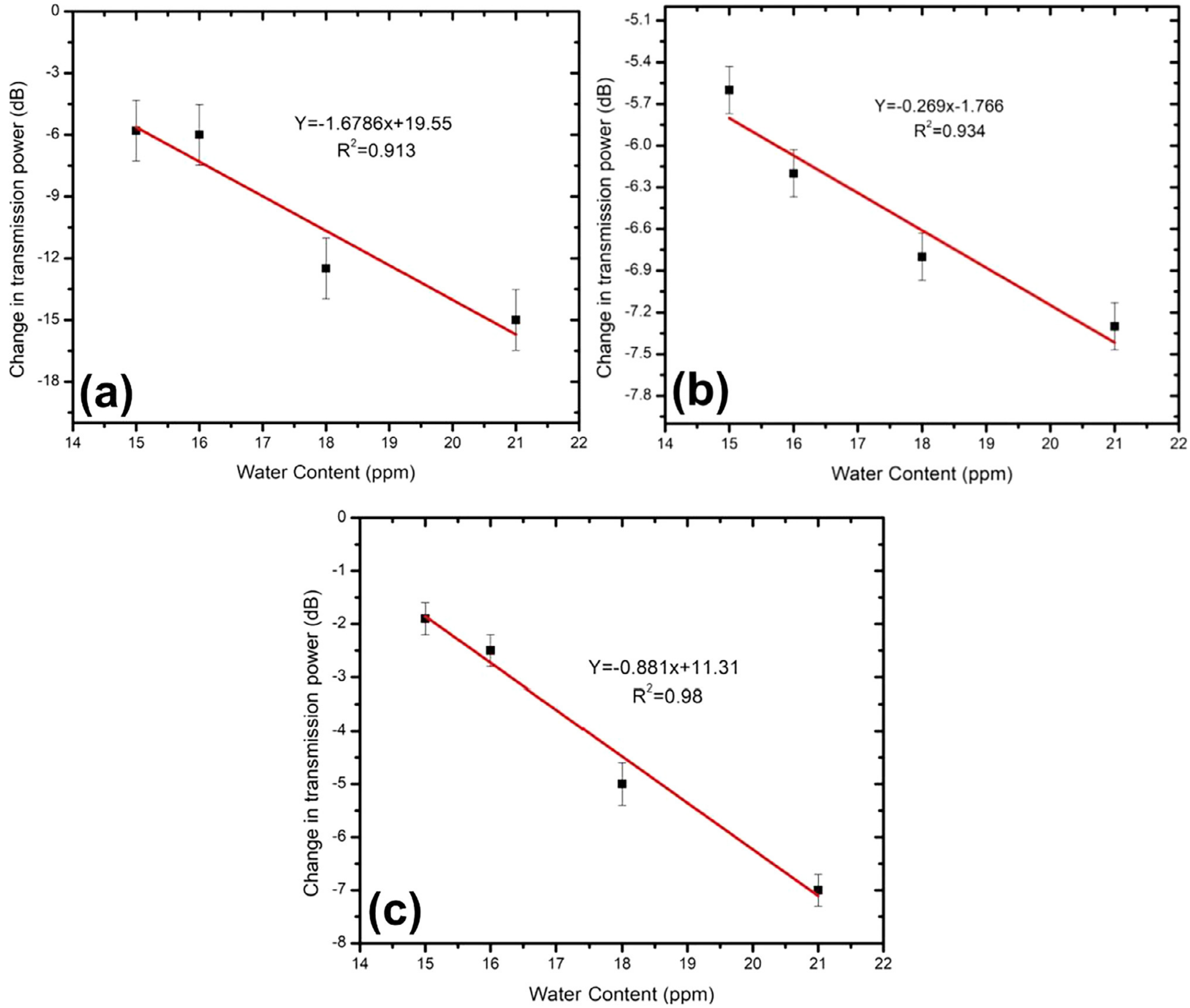

Fig. 10. Change in TE power (dB) after four samples of oil drop on the sensing region of the fiber.

shows that the sensor is having a fast response and high sensitivity. This observation could be due to the rapid adsorption rate of the sensor as the water molecules from the transformer oil react with the platinum surface in an equilibrium environment. It is clearly seen that for oil sample with water content range from 15 ppm to 21 ppm, transmitted power level changes from 1.8 dB to 7.0 dB.

Mahanta et al. demonstrated the detection of water content in transformer oil using a polymer optical fiber sensor. It was reported that when water content changes from 20 ppm to 65 ppm, the transmitted power of the fiber sensor, measured in voltage, decreases from 88 mV to 57 mV [16]. Further demonstrations of the measurement of water content in transformer oil using optical sensors are reported by Laskar et al. [17] and Banerjee et al. [18], where both reports the change in light propagation behavior due to the change in water content in the transformer oil under test. Though the exact value of change was not reported, it is believed that water content in transformer oil has a profound effect on the refractive index of the transformer oil, thus enabling response from the optical sensors used.

From the plots, the response time for TE power altered to lower values shows the sensor is having a fast response and high sensitivity. This observation could be due to the rapid adsorption rate of the sensor as the water molecules from the transformer oil when reacting with the platinum surface in an equilibrium environment. It is clearly seen that for oil sample with a low concentration of water (15 ppm), the changes in TE power is small compared to the oil sample with the water concentration of 21 ppm. This is due to the changes in refractive index of the platinum layer when oil samples were dropped onto the metal layer. In addition, the samples also have different refractive index values because of the different concentration of water consists in it. Meanwhile, when single-mode fiber was polished to form a cross-section of D-shaped, a slight curvature was seen on the fiber and this could increase the sensitivity of the sensor. The major fluctuation observed on TE power of every sample suggests that there might be an existence of unwanted element inside the oil such as dissolved gas.

Fig. 10 shows the average of power drop as a function of water content values (ppm). It can be seen that a decrease in the power has occurred with the increment in water content values (ppm). It can be summarized that there is a good linear behavior of TE power when oil samples dropped on the sensing region of the fiber. Fig. 10 shows the change in transmitted power for different water content in the oil sample. The fluctuation in power during 100 s may not give an accurate reading, but we can take the average of the power. It shows a relationship between water content in oil and the change in transmitted power within the range of 15–21 ppm. The sensitivity of the proposed sensor to water content dissolved in transformer oil is calculated to be -1.6 dB/ppm of water for bare fiber shown in Fig. 10(a). Fig. 10(b) describes sensitivity of the proposed sensor to water content dissolved in transformer oil is calculated to be −0.269 dB/ppm of water for the sensor with a thickness of Pt as 15 nm. For a sensor with a thickness of Pt coating as 25 nm (Fig. 10(c)) shows the sensitivity of the sensor to water content dissolved in transformer oil is calculated to be −0.88 dB/ppm of water. Higher values of water content inside the oil samples are similar to the percentage of relative humidity. It indicates that the linear decrease in TE power with increasing water concentration in the oil sample proves the compatibility of the platinum D-shaped fiber for humidity sensing application. The drop in TE power is quite significant due to the adsorption of water molecules by the Pt layer as the oil samples were dropped onto the surface. Since the platinum thin layer was added on the fiber, a great surface area on the surface of the fiber is possessed which provide more area for the detection of power changes.

5. Conclusion

This paper describes an instrumentation system to measure moisture content in a transformer oil sample using manipulating the effects of platinum metal-coating on D-shape optical fiber. Conventional test methods for evaluating the condition of transformer oil have certain limitations. We demonstrate that evanescence wave-based sensor provides better sensitivity in comparison to the intensity of bare optical fiber. The effect of moisture on the TE power was investigated experimentally using a set of four aged oil samples with a different ppm of water content. The experimental results have confirmed that the TE power of the D-shaped fiber changed significantly to the lower value when insulating oil with different water content is sensed. The changes in TE power are higher with the increasing water content. It is proved that the electrical strength of the transformer system has highly depending on the moisture level in the insulating oil. Even though a detailed work is necessary to determine the correlation between the exact amount of water content measurable in the laboratory and the extent to which the transformer oil has aged, it is shown that the contamination of transformer oil can be detected by fiber optic sensors with integrating of metallic thin layer as platinum is a good catalyst in fuel cell research. The presented research and obtained results can be useful for the current utilities due to the need of lower maintenance cost, higher transformer's life, better operation safety, avoid power failures and lower energy cost especially for the energy consumers.

Acknowledgments

This work was supported by University Malaya Postgraduate Research Grant (PG215-2016A) and FLC 001C-14AET.

References

[1] A.V.M.Y. Du, B.C. Lesieutre, M. Zahn, S.H. Kang, Moisture solubility for differently conditioned transformer oils, IEEE Trans. Dielectr. Electr. Insul. 8 (2001) 805.
[2] S. Laskar, S. Bordoloi, Monitoring of moisture in transformer oil using optical fiber as sensor, J. Photonics 2013 (2013) 7.
[3] D. Hazarika, D.S. Pegu, Micro-controller based air pressure monitoring instrumentation system using optical fibers as sensor, vol. 19, 2013.
[4] M.R.S. EL-Sayed, M.M. EL-Refaie, A. Wael, Prediction of the characteristics of transformer oil under different operation conditions, World Acad. Sci. Eng. Technol. Int. J. Electr. Computer Eng. vol, (2009) 3.
[5] E.M.G.R. Radu Godina, João C.O. Matias, João P.S. Catalão, Effect of loads and other key factors on oil-transformer ageing: sustainability benefits and challenges, Energies 8 (2015) 12147–12186.
[6] C. Dervos, C. Paraskevas, P. Skafidas, P. Vassiliou, A complex permittivity based sensor for the electrical characterization of high-voltage transformer oils, Sensors 5 (2005) 302.
[7] B. Buerschaper, O. Kleboth-Lugova, T. Leibfried, The electrical strength of transformer oil in a transformerboard-oil system during moisture non-equilibrium, in: 2003 Annual Report Conference on Electrical Insulation and Dielectric Phenomena, 2003, pp. 269–272.
[8] O.E. Gouda, G.M. Amer, W.A.A. Salem, Predicting transformer temperature rise and loss of life in the presence of harmonic load currents, Ain Shams Eng. J. 3 (2012) 113–121 2012/06/01/.
[9] N. Cennamo, L. De Maria, G. D'Agostino, L. Zeni, M. Pesavento, Monitoring of low levels of furfural in power transformer oil with a sensor system based on a POF-MIP platform, Sensors 15 (2015) 8499–8511.
[10] T. Bosworth, S. Setford, R. Heywood, S. Saini, Pulsed amperometric detection of furan compounds in transformer oil, Anal. Chim. Acta 450 (2001) 253–261.
[11] J.-E. Kim, K.S. Suh, Tae-Young Kim, On-line monitoring of transformer oil degradation based on fiber optic sensors, Sensors Mater. 20 (vol. 2008,) 201–209.
[12] L. Árnadóttir, E.M. Stuve, H. Jónsson, Adsorption of water monomer and clusters on platinum (111) terrace and related steps and kinks: I. Configurations, energies, and hydrogen bonding, Surf. Sci. 604 (2010) 1978–1986.
[13] H.A. Gasteiger, S.S. Kocha, B. Sompalli, F.T. Wagner, Activity benchmarks and requirements for Pt, Pt-alloy, and non-Pt oxygen reduction catalysts for PEMFCs, Appl. Catal. B 56 (2005) 9–35.
[14] S. Singh, R.S. Kaler, Performance analysis of evanescent wave absorption plasmonic optical sensor with COMSOL FEM method simulation, Procedia Comput. Sci. 125 (2018) 376–381 2018/01/01/.
[15] A. Banerjee, S. Mukherjee, R.K. Verma, B. Jana, T.K. Khan, M. Chakroborty, et al., Fiber optic sensing of liquid refractive index, Sens. Actuators, B 123 (2007) 594–605 2007/04/10/.
[16] D.K. Mahanta, S. Laskar, Water quantity based quality measurement of transformer oil using polymer optical fiber as sensor, IEEE Sens. J. (2017).
[17] S. Laskar, S. Bordoloi, Monitoring of moisture in transformer oil using optical fiber as sensor, J. Photonics 2013 (2013).
[18] A. Banerjee, S. Mukherjee, R.K. Verma, B. Jana, T.K. Khan, M. Chakroborty, et al., Fiber optic sensing of liquid refractive index, Sens. Actuators, B 123 (2007) 594–605.

Journal of Superconductivity and Novel Magnetism
https://doi.org/10.1007/s10948-018-4628-5

ORIGINAL PAPER

Optical Properties of New Type of Superconductor-Semiconductor Metamaterial Photonic Crystals

Arafa H. Aly[1] **· Doaa Mohamed**[1] **· Hussein A. Elsayed**[1] **· Dhasarathan Vigneswaran**[2]

Received: 25 December 2017 / Accepted: 26 February 2018

Abstract

Based on the fundamentals of the characteristic matrix method, we theoretically investigate the optical properties of onedimensional superconductor metamaterial photonic crystals. The photonic crystals are composed of a superconductor layer and two semiconductor metamaterial layers of $In_{0.53}Ga_{0.47}As$ with different doping densities. The numerical results show negative values in permittivity of the metamaterial layer along a broad band of the incident radiation. The negative values show a significant effect on the optical properties of the present structure. Moreover, the optical properties of our design can be controlled by different parameters such as thicknesses of the layers, the operating temperature and the doping density. Our results may be suitable for different applications in the optical community.

Keywords Superconductor · Photonic crystals · Metmaterial · Optical properties

1 Introduction

In 1968, Veselago predicted an artificial material which has the negative index of refraction called negative index material (NIM). Also, NIM known as the double negative material which has negative permeability and negative permittivity, the material only with negative permittivity is called epsilon negative material (ENG), and the material only with negative permeability is known as mu-negative material (MNG) [1, 2]. Within the eights of the past century, the concept of photonic crystals (PCs) was first investigated by Yablonovitch and John [3, 4]. PCs became the main spring in many applications due to their unique electromagnetic properties. PCs are investigated due to their importance in the existence of photonic band gaps (PBGs), a frequency region in which the electromagnetic field could not be able to propagate [4]. The main parameters around the appearance of those PBGs are due to the periodic modulation of the refractive index in constituent materials of PCs. Thus, many researchers intended to demonstrate the superior properties of PCs with metamaterials for more applications in the optical community. It attracts more attention in recent years due to their potential applications such as subdiffraction imaging, cloaking, confinement, etc. [5]. In particular, the inclusion of dispersive media such as semiconductors, metals, and superconductors gives a promising impression toward the achievements of such applications. One of the designs that offer negative refraction is the semiconductor metamaterial (SMM) [6]. This is a nonmagnetic structure that consists of two thin layers of different semiconductors, which exhibit its anisotropic properties having different permittivities for the normal and parallel polarization of electromagnetic waves [7]. Since the first SMM was developed [8], there has been a dispute between scientists whether this structure really demonstrates negative refraction. Based on the novel properties of metamaterials and PCs, we intend to investigate the reflectance properties of one-dimensional PCs in the visible wavelength regions. The present structure is consisting of a high-temperature superconductor material and SMM that is repeated for N periods. Here, we choose the high-temperature superconductor material to be $BaSrCaCuO_7$, and metamaterial is designed from two thin layers of $In_{0.53}Ga_{0.47}As$ with different doping density. The theoretical modeling mainly depends on the characteristic matrix method. Our target is to investigate

✉ Arafa H. Aly
arafa.hussien@science.bsu.edu.eg; arafa16@yahoo.com

1 Physics Department, Faculty of Science, Beni-Suef University, Beni-Suef, Egypt

2 Department of ECE, Sri Krishna College of Technology, Coimbatore, 641 042, India

theoretically the negative permittivity of the SMM in the visible light regions by means of doping density variations. Then, we intend to study the effect of this negative permittivity on the reflectance properties of our structure. The numerical results show the appearance of the Fabry Perot resonator that is significantly affecting the properties of the constituent materials of the PCs.

2 Basic Equations

In this section, we discuss the theoretical analysis of the work. Here, we use the well-known characteristic matrix method to obtain the reflectance characteristics of our periodic structure. As shown in Fig. 1, the structure is designed as $(ABC)^N$, wherein layer A represents the high-temperature superconductor layer ($Bi_2Sr_2CaCuO_8$) [11]. Then, layers B and C describes the SMM ($In_{0.53}Ga_{0.47}As$) with different doping density. From the twofluid model, the relative permittivity of the superconductor material can be expressed as [12–17].

$$\varepsilon_r = 1 - \frac{1}{\omega^2\,\mu_0\varepsilon_0\lambda_l^2} \tag{1}$$

where λ_l is the temperature-dependent penetration depth and can be written in the form:-

$$\lambda_l\,(T) = \frac{\lambda_0}{\sqrt{1 - F(T)}} \tag{2}$$

where λ_0 is the London penetration depth at $T =$ K and the Groter-Casimir expression for $F(T)$ is written in the following form:

$$F\,(T) = \left(\frac{T}{T_c}\right)^p \tag{3}$$

where T_c is the superconducting critical temperature and T is the operating temperature. The exponent (p) depends on the type of superconductor material, at high-temperature superconducting materials $p = 2$ [18], while for low-temperature superconductors $p = 4$. The permittivity of semiconductor metamaterial, InGaAs can be expressed based on the basics of the plasma model, wherein:

$$\varepsilon = \varepsilon_\infty\varepsilon_0\left(1 - \frac{\omega_p^2}{\omega^{2+j\Gamma_e\omega}}\right) \tag{4}$$

where ε_0 and ε_∞ are the vacuum and the background permittivity, respectively, ω is the incident electromagnetic wave frequency, Γ_e is the damping frequency and ω_p is plasma frequency that can be expressed as:

$$\omega_p = \frac{n_d e^2}{m_{eff}\varepsilon_\infty\varepsilon_0} \tag{5}$$

whereas, m_{eff} is the electron effective mass, e is the electron charge, and n_d is the doping density. Then, the parallel and the perpendicular components of the metamaterial permittivity can be described as:

$$\varepsilon_\perp = \frac{2\varepsilon_1\varepsilon_2}{\varepsilon_1 + \varepsilon_2},\quad \varepsilon_\parallel = \frac{\varepsilon_1 + \varepsilon_2}{2} \tag{6}$$

where ε_1 and ε_2 represent the permittivities of the two semiconductor layers (B and C) which are obtained from (4). Now, the characteristic matrix method that describes the interaction of the incident electromagnetic waves with our design is expressed as [13–15]:

$$M = \begin{pmatrix} M_{11} & M_{21} \\ M_{21} & M_{22} \end{pmatrix} = D_0^{-1}\left(D_1P_1D_1^{-1}D_2P_2D_2^{-1}D_3P_3D_3^{-1}\right)D_s \tag{7}$$

with,

$$M_l = \begin{pmatrix} \cos\,(k_{lz}d_l) & jq_l^{-1}\sin\,(k_{lz}d_l) \\ jq_l\sin\,(k_{lz}d_l) & \cos\,(k_{lz}d_l) \end{pmatrix} \tag{8}$$

where M_l is the matrix for individual layer l ($l =$ A, B, and C). Then, the transmittance can be obtained based on the matrix elements of (7) as:

$$T = |2p \div ((M_{11} + M_{12}p)\,p + M_{21} + M_{22}p)|^2 \tag{9}$$

with,

$$p = \sqrt{k_0^2 - k_x^2} \div k_0 = \cos\,(\theta_o) \tag{10}$$

Thus, the reflectance is given by:

$$R = 1 - T \tag{11}$$

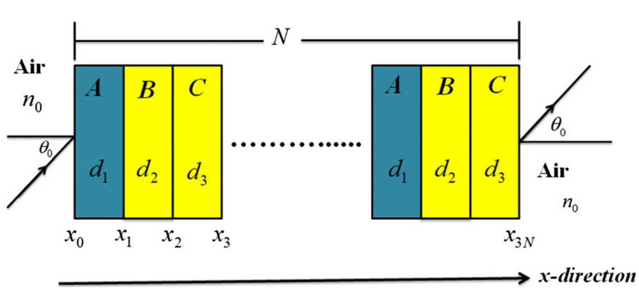

Fig. 1 Schematic representation of the one-dimensional superconductor-semiconductor metamaterial, PCs composed of three layers and the surrounding medium is air

3 Results and Discussions

For the numerical analysis, we consider the superconductor layer to be $Bi_2Sr_2CaCuO_8$ with ($T = 4.2$ K, $T_c = 95$ K, $\lambda_o = 150$ nm) [19] and $d_1 = 0.1\,\mu$m. The semiconductor metamaterial is designed from two layers of $In_{0.53}Ga_{0.47}As$

with different doping densities. $In_{0.53}Ga_{0.47}As$ is characterized with $m_{\rm eff} = 0.0425\,m_0$, where m_0 is the free electron mass, $\varepsilon_\infty = 12.15$, and $\Gamma_e = 10\,\text{THz}$. Then, the doping density of layer (B) is set to be $7.5 \times 10^{18}\,\text{cm}^{-3}$ while the doping density of layer (C) is $17.7 \times 10^{18}\,\text{cm}^{-3}$. Also, we consider the thicknesses of the two semiconductor layers to be ($d_2 = 0.01\,\mu$m, $d_3 = 0.01\,\mu$m). Here, the number of periods is set to be $N = 15$. The numerical results are presented in two stages. First, we discuss the response of the metamaterial permittivity within the visible light. Then, we investigate the reflectance properties under the influence of the parameters of the constituent materials such as the thickness of the layers, the operating temperature of the superconductor and the doping density of the semiconductors. Figure 2 demonstrates the parallel component ($\varepsilon_{\rm p}$) and the perpendicular component ($\varepsilon_{\rm V}$) of the permittivity in the regions of visible light and near infrared. It can be seen that both parallel and perpendicular permittivities are decreasing with wavelength. For the wavelengths greater than 0.5 µm, the parallel and the perpendicular components take almost negative values. In addition, the parallel component is more negative than the perpendicular. This figure investigates that there are negative values for the permittivity of semiconductor metamaterial which could offer the tools for producing the electromagnetic waves in evanescent modes.

In the second stage, we demonstrate the reflectance characteristics of our structure. Figure 3 shows the appearance of narrow transmission bands in the range between 0.23 and 0.89 μm. It indicates that the electromagnetic wave can only propagate through these regions. The appearance of such bands could be due to the negative permittivity of metamaterial. For wavelengths greater than 0.89 μm, the electromagnetic waves are evanescent and get reflected as shown in Fig 2 This is due to the increase in permittivity of metamaterial with the increase of wavelength of the incident radiation as concluded from Fig. 3.

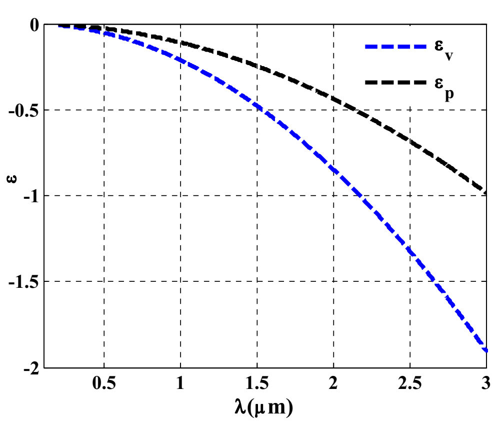

Fig. 2 The response of the parallel and perpendicular component of the metamaterial permittivity versus wavelength at two different values of the doping impurity concentration

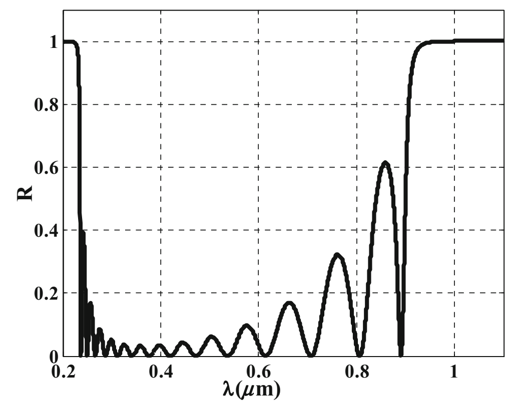

Fig. 3 Reflectance spectra of one-dimensional superconductor-semiconductor metamaterial PCs for TM waves at normal incidence

Then, we discuss the effect of thickness variation on the reflectance properties of our structure. Figure 4 shows the reflectance spectra at different thicknesses of the superconductor layer. At $d_1 = 0.1$ µm, Fig. 4 shows the appearance of the transmission band that extended from 0.2 to 0.9 µm. At the thickness of the superconductor layer increased to 0.2, 0.3 and 0.4 µm, there are many narrow PBGs that begin to appear in the wavelength regions from 0.2 to 0.9 µm. Thus, the number of these narrow PBGs is increasing with the increments of the thickness of the superconductor layer. Thus, the variation of superconductor layer thickness has a significant effect on the reflectance

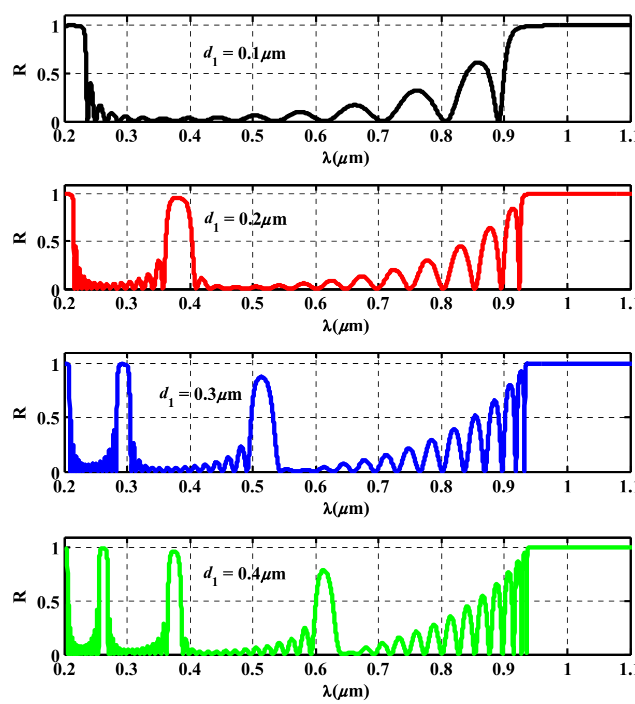

Fig. 4 The reflectance spectra of our structure at different values of the superconductor layer thickness

spectra of our structure and could be effective in using this structure as a multichannel filter.

On the other hand, the variation in thicknesses of two semiconductor layers could offer an additional control on the reflectance properties of our structure as shown in Fig. 5. Here, the thicknesses of the two layers are increased together from (d_2 = 0.01 µm, d_3 = 0.01 µm) to (d_2 = 0.04 µm, d_3 = 0.04µm), (d_2 = 0.08 µm, d_3 = 0.08 µm) and (d_2 = 0.1 µm, d_3 = 0.1 µm) at d_1 = 0.1 µm. At d_2 = 0.01 µm and d_3 = 0.01 µm, the transmission band appears at wavelength region from 0.22 to 0.9 µm. By increasing the thickness of metamaterial layers gradually to (d_2 = 0.04 µm, d_3 = 0.04µm), (d_2 = 0.08 µm, d_3 = 0.08 µm) and (d_2 = 0.1 µm, d_3 = 0.1 µm), respectively, the transmission band shrinking to be narrow transmission band in the range between 0.41 and 0.78 µm as shown in Fig. 5. Moreover, the dips present in the transmission band behave like localized pass bands which are used in designing Fabry Perot resonator without breaking the periodicity of the structure.

Now, we study the effect of increasing the operating temperature of the superconductor layer on our structure. The results are plotted in Fig. 6, in which d_1 = 0.1 µm, d_2 = 0.05 µm and d_3 = 0.05 µm. The figure shows that the transmission band is widened toward the long wavelength regions with the increase of the operating temperature. The reason around the variation in transmission band

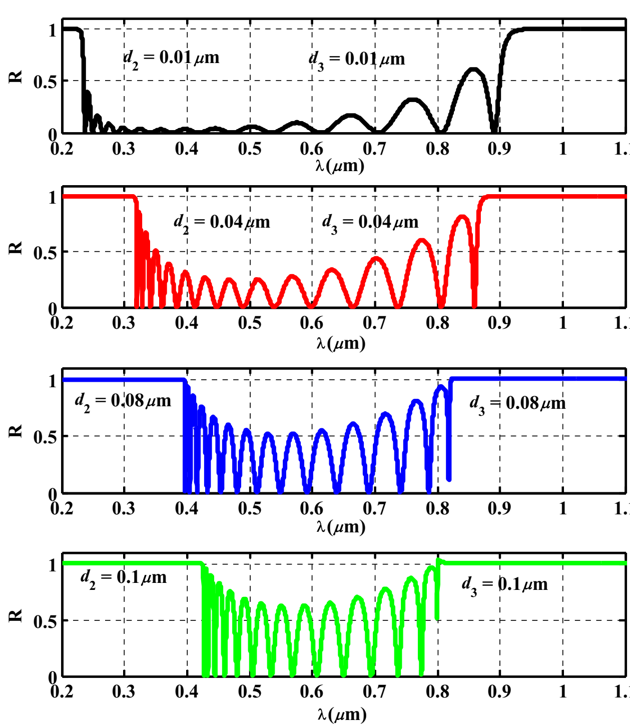

Fig. 5 The reflectance spectra of $(ABC)^N$ structure with the increasing of the thicknesses of two semiconductor layers

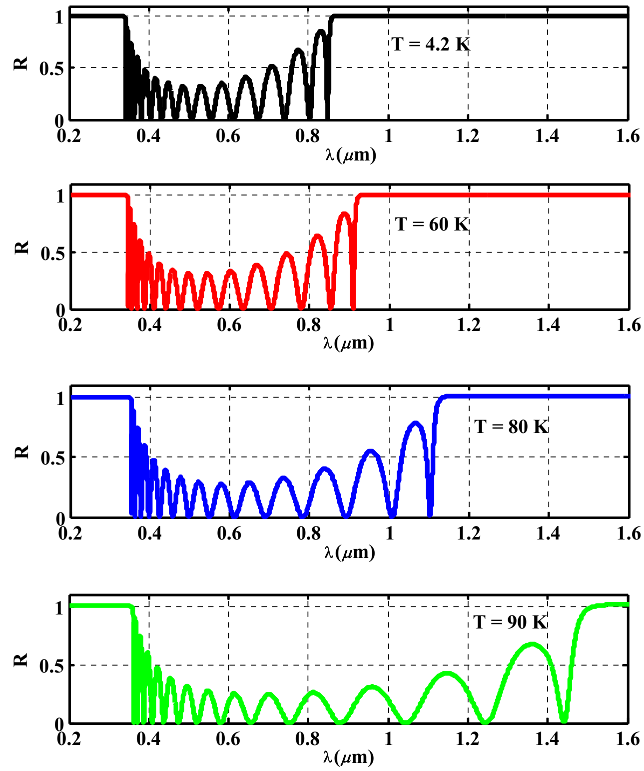

Fig. 6 The reflectance spectra at different values of the operating temperature

with the operating temperature can be simply understood from the equations (1) and (2). As the operating temperature increases, the value of the London penetration depth varies which will be effective on the permittivity of the superconductor layer. Therefore, the width of the transmission band changes due to the variations in permittivity of the superconductor layer. This effect may offer a new way to control the reflectance properties of our design.

Finally, we investigate in Fig. 7 the dependence of the reflectance properties on the doping density of the semiconductor material. Here, the doping density of the second semiconductor layer (layer C) is kept constant at 17.7×10^{18} cm^{-3}, wherein the doping density of the first semiconductor layer (layer B) is changed. To achieve a negative permittivity in metamaterial layer, the doping density of the second layer is to be kept constant and it increases with the change of the doping density of another layer of metamaterial. As the doping density of layer B increased from 7.5×10^{18} cm^{-3} to 40×10^{18} cm^{-3}, 70×10^{18} cm^{-3}, and 110×10^{18} cm^{-3}, the transmission bands are affected with the increase of doping density and its width gets decreased in the wavelength range from 0.23 to 0.62 µm. This means that the transmission bands are localized in the visible and near-ultraviolet region.

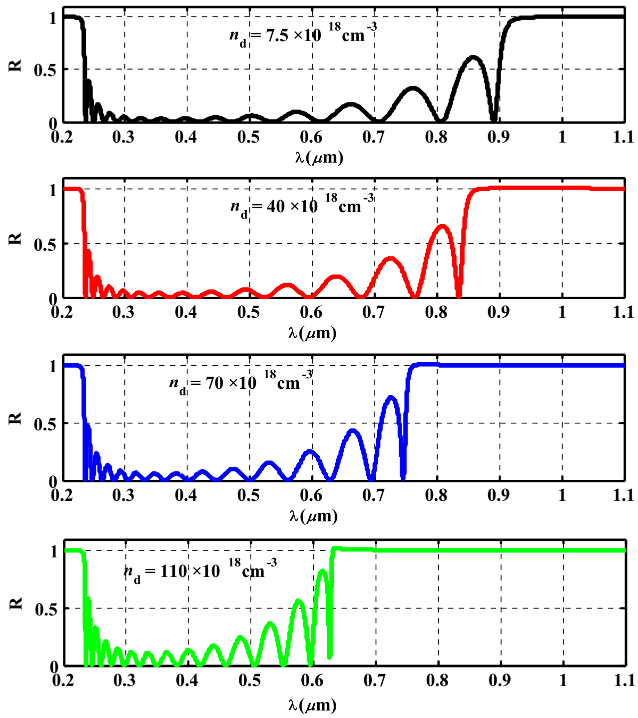

Fig. 7 The reflectance spectra at different values of the doping density of layer B

4 Conclusion

In this paper, we have investigated the reflectance properties of one-dimensional superconductor-semiconductor metamaterial PCs. The numerical results obtained are based on the characteristic matrix method. The numerical results show that the two layers of $In_{0.53}Ga_{0.47}As$ of different doping densities could produce a metamaterial with a negative permittivity along the visible and nearIR regions. The negative values of permittivity could control the evanescent modes of the incident electromagnetic radiations. Moreover, the parameters of the constituent materials such as the thicknesses of the layers, the operating temperature and the doping density can produce more facilities toward the control of the reflectance properties. The present work may be of potential use in many applications such as multichannel filter and Fabry-Perot resonator.

References

1. Wang, L., Wang, Z., Sang, T.: Chinese Opt. Lett. **6**(3), 198 (2008)
2. Aly, A.H., et al.: Int. J Advan. Appl. Phys. Res. **4**, 14–21 (2017)
3. Yablonovitch, E.: Phys. Rev. Lett. **58**, 2059 (1987)
4. Li, X., Xie, K., Jiang, H.: Chinese Opt. Lett. **6**(2), 130 (2008)
5. Shelby, R.A., Smith, D.R., Schultz, S.: Science **292**, 77 (2001)
6. Podolskiy, V.A., Narimanov, E.E.: Phys. Rev. B. **71**, 201101 (2005)
7. Ilic, I., Belicev, P.P., Milanovic, V., Radovanovic, J., Hadzievski, L.: J. Electromagn Waves Appl. **26**, 2323 (2012)
8. Hoffman, A.J., Alekseyev, L., Howard, S.S., Franz, K.J., Wasserman, D., Podolskiy, V.A., Narimanov, E.E., Sivco, D.L., Gmachl, C.: Nature Mater. **6**, 946 (2007)
9. Markel, V.A.: Opt. Express. **16**, 19152 (2008)
10. Markel, V.A., Schotland, J.C.: J. Opt. **12**, 015104 (2010)
11. Aly, A.H., Mohamed, D.: J. Supercond. Nov. Magn. **18**, 1699 (2015)
12. Aly, A.H., Hsu, H.T., Yang, T.J., Wu, C.J., Hwangbo, C.K.: J. Appl. Phy. **105**, 083917 (2009)
13. Aly, A.H., Sayed, W.: J Supercond. Nov. Magn. **29**, 1981–1986 (2016)
14. Aly, A.H., Sabra, W., Elsayed, H.A.: Int. J. Mod. Phys. B **31**, 1750123 (2017)
15. Aly, A.H., et al.: Published online in Int. J. Mod. Phys. (2018). https://doi.org/10.1142/S021797921850056X
16. AH Aly, H.-T., Hsu, T.-J., Yang, C.-J., Hwangbo, C.K.: J. Appl. Phys. **105**, 083917-6 (2009)
17. Born, M., Wolf, E.: Principles of Optics. Cambridge, London (1999)
18. Aly, A.H., Elsayed, H.A., Malek, C.: Accepted in Optica Applicata, will publish in 2018
19. Vendik, O.G., Vendik, I.B., Kaparkoy, D.I.: IEEE Trans. Micro wave Theory Tech. **46**, 469 (1998)

Results in Physics 11 (2018) 1087–1093

Contents lists available at ScienceDirect

Results in Physics

journal homepage: www.elsevier.com/locate/rinp

Dual wavelength optical duobinary modulation using GaAs–AlGaAs microring resonator

I.S. Amiri[a,b], R. Zakaria[c,*], T. Anwar[d], M. Bahadoran[e], D. Vigneswaran[f], P. Yupapin[a]

[a] Computational Optics Research Group, Advanced Institute of Materials Science, Ton Duc Thang University, Ho Chi Minh City, Viet Nam
[b] Faculty of Applied Sciences, Ton Duc Thang University, Ho Chi Minh City, Viet Nam
[c] Photonics Research Centre, University of Malaya, 50603 Kuala Lumpur, Malaysia
[d] Department of Computer and Information Science (DCIS), Faculty of Science and Information Technology (FSIT), Universiti Teknologi Petronas (UTP), 32610 Seri Iskandar, Malaysia
[e] Department of Physics, Shiraz University of Technology, 31371555 Shiraz, Fars, Iran
[f] Department of Electronics and Communication Engineering, Sri Krishna College of Technology, Coimbatore 641 042, India

ARTICLE INFO

Keywords:
Optical duobinary modulation technique
Dual-wavelength
Microring resonators

ABSTRACT

In this article, optical duobinary modulation technique has been used for modulating the dual-wavelength optical signal generated by the microring resonator system. The optical signals are de-multiplexed to two different optical signals with center wavelength of 1540 and 1545 nm afterward, these are modulated and transmitted over an optical fiber communication system, where the high performance of the transmitted signals is obtained. The NRZ binary signals are used to modulate the optical signals. The high-quality factor and performance of the system has been investigated by applying an optimization through the system parameters, where significant improvement could be obtained and highest quality factor of 32.871 shows the successful transmission. The second wavelength of the dual-wavelength has undergone the same modulation technique and has experienced the optical transmission after the system optimization has been performed, where the quality factor for the received optical signal at 1545 nm center wavelength is 39.282. These results show the introduced modulation technique is suitable to apply for the optical signals generated by the microring resonators.

Introduction

Optical ring waveguide resonators are emerged in aspects of optical MUX/DEMUX, filtering, the resonance wavelength, pulse switching [1] and splitting efficiency applications [2]. The basic functional parameters such as ring diameter, waveguide thickness are the main features of the resonator system [3]. With that significant property, low bending loss is achieved by the interface region among air-semiconductor-air structures [4,5]. In this low bending analysis, there was a miracle finding in mode propagation and it was thought of 1000 times better than the weakly guiding approximation of ring waveguide having 1–2 µm of diameters [6]. The propagation properties have confirmed that the light is enhanced and tuned for the resonant point inside the ring facet which is extended for all optical communication applications [7], optical switching [8], emission of optical energy [9] and nonlinear optics signal processing [10]. Here we present the demonstration of GaAs–AlGaAs waveguide microring resonators for application in optical signal modulation and transmission over an optical fiber communication. We have also shown that such resonators can be used to generate ultra-wide free spectral range (FSR) pulses with THz spacing, providing THz photonics communication signals. In this research we have utilized the microring resonator to generate dual-wavelength at center frequencies of 1540 and 1545 nm. We have applied the optical duobinary modulation technique to the optical signals (dual-wavelength) before undergoing a transmission through an optical fiber transmission link. It is possible to stabilize the spectral property by indirectly monitoring the bandwidth adjustment which tends to reduce the dispersion effect for the better modulation system for data communication [11,12]. The system can be presented by following building block (Fig. 1).

The line coding configuration of the duobinary code is identical to the RZ line coding format [13]. If the data sequences defined as D_m and encoded data named as P_m, then the duobinary modulation is performed by comparing the output of precoder with the input to the precoder. The combination of precoder and modulo 2 operation blocks is known as differential precoder where the error possibility during the data propagation is minimized. The reduced symbol interference then is applied as an input into the optical modulator as shown in Fig. 1. This

* Corresponding author.
E-mail addresses: irajsadeghamiri@tdtu.edu.vn (I.S. Amiri), rozalina@um.edu.my (R. Zakaria).

https://doi.org/10.1016/j.rinp.2018.11.016
Received 12 October 2018; Received in revised form 4 November 2018; Accepted 7 November 2018
Available online 13 November 2018

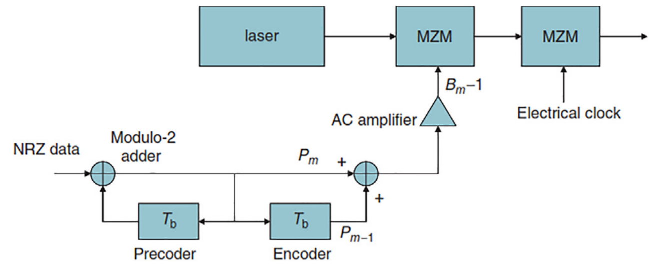

Fig. 1. Functional block of duobinary modulation scheme, The MZM is Lithium Niobate (LiNbO3) Mach Zehnder modulator.

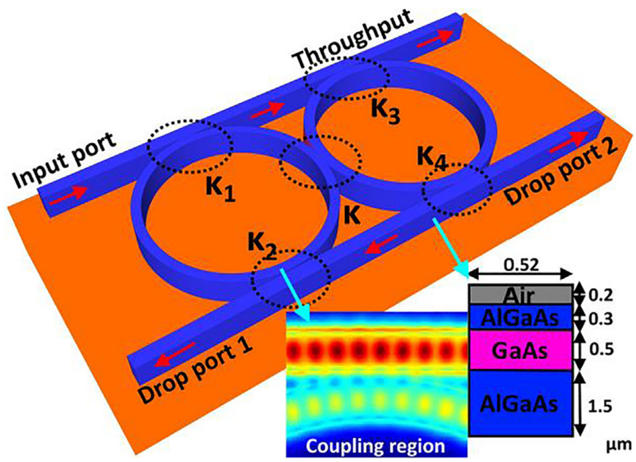

Fig. 2. Microring resonator structure, *R*: Radius, *κ*: Coupling coefficient.

modulation format is taken as the unique one as it may be extended in distance to send the data with free propagation loss without regenerator and repeaters [14,15]. Earlier, this modulation scheme was utilized for the 40 Gbps direct detection method [16]. The another challenge to send the data for long distance without presence of intersymbol interference is crucial [17] which is resolved by providing a delay in the bit slot [18]. The present work also shows that significance of duobinary modulation function with help of ring resonator laser source.

Microring resonator system

The proposed system for dual-wavelength generation is shown in Fig. 2. A Gaussian laser beam with power of 1 W is used as input. The two microring resonators have a same radius of 6.36 µm, and coupling coefficients as $\kappa = 0.482$, $\kappa_1 = \kappa_2 = \kappa_3 = \kappa_4 = 0.02$.

The structure is modelled of GaAs–AlGaAs with GaAs core whose refractive index is 3.368 surrounded by AlGaAs (refractive index is 3.135). The nonlinear refractive index is $2.7 \times 10^{-16}\,\mathrm{cm^2/W}$ for wavelengths around 1550 nm. The other dimension for the given layer is scaled as follows,

Air cap (0.2 µm)
AlGaAs cladding (0.3 µm) ($n = 3.135$)
GaAs core (0.5 µm) ($n_0 = 3.368$)
AlGaAs buffer (1.5 µm) ($n = 3.135$)
Substrate (5 µm)

This system consists of two coupled microring resonators. Further application of the proposed structures also has been used for optical comb generations with minimum of power consumption [18,19]. Moreover, the material of III–V material compound for semiconductor is used for many nonlinear optical applications [20–24]. The transmission property and its functional behavior of the proposed structure is detailed in Ref. [25] and also it is exhibited to reduce inter-channel interference in optical communication networks and on-chip interconnects [26].

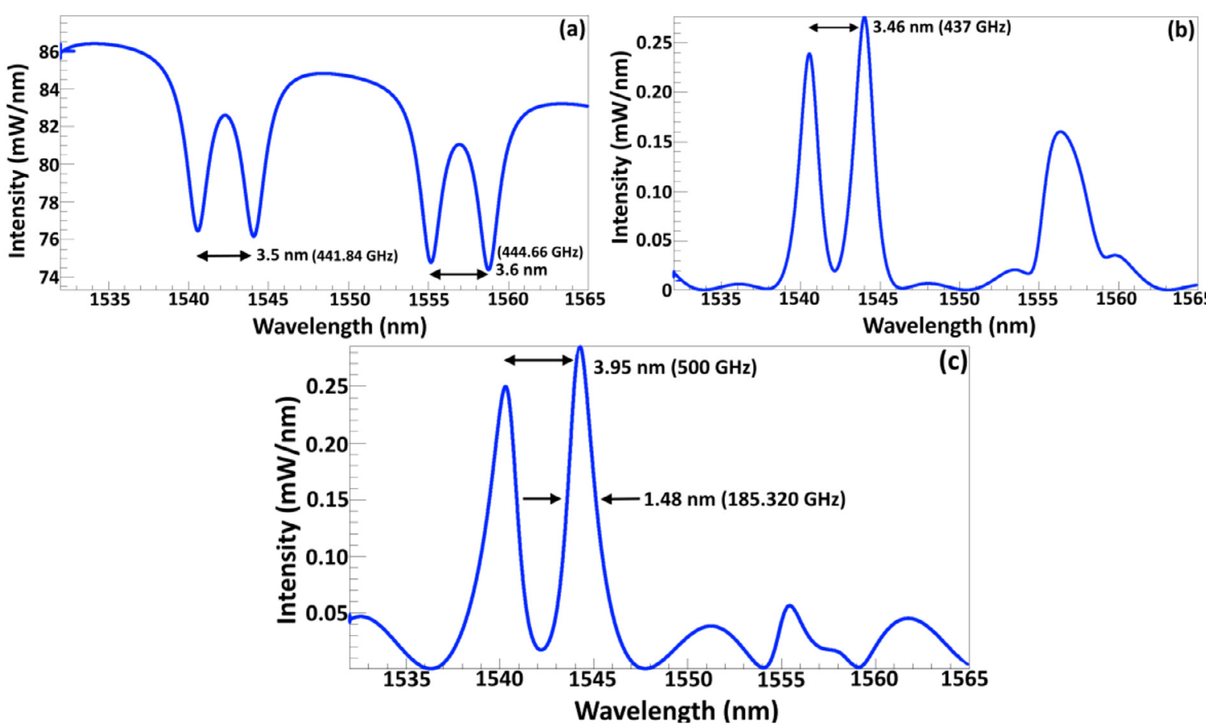

Fig. 3. (a) Throughput outputs, dual-wavelength optical signals with free spectral range (FSR) = 3.5 nm and 3.6 nm corresponding to 441.84 GHz and 444.66 GHz respectively, (b) Drop port (1) outputs, dual-wavelength optical signal with FSR = 3.46 nm corresponds to 437 GHz, (c) Drop port (2) outputs, dual-wavelength optical signal with FSR = 3.95 nm corresponds to 500 GHz.

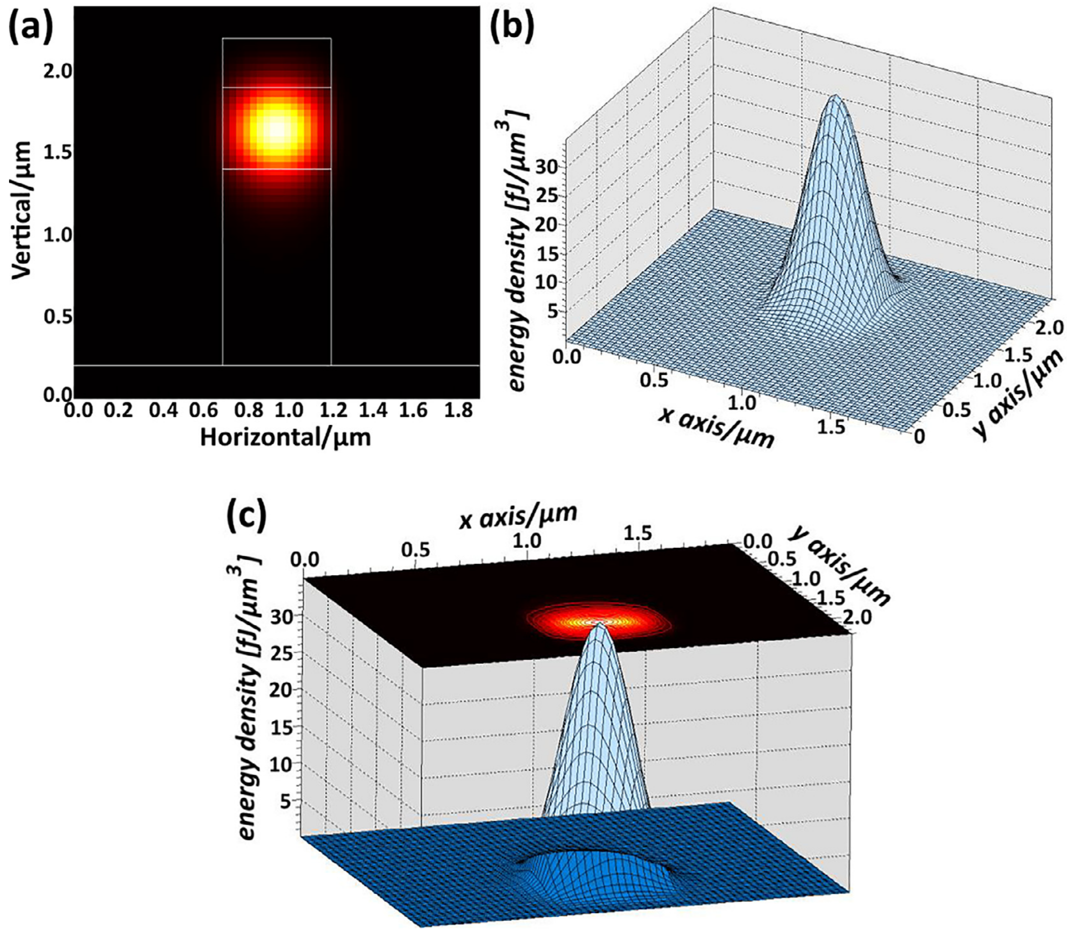

Fig. 4. (a) Mode propagating along the core guidance of waveguide. (b) Energy density plot of the mode profile (c) 3D view. Effective index = 3.07, group index = 3.50, dispersion (ps/nm/km) = −27, mode confinement factor = 0.80, effective area = 0.344 μm^2.

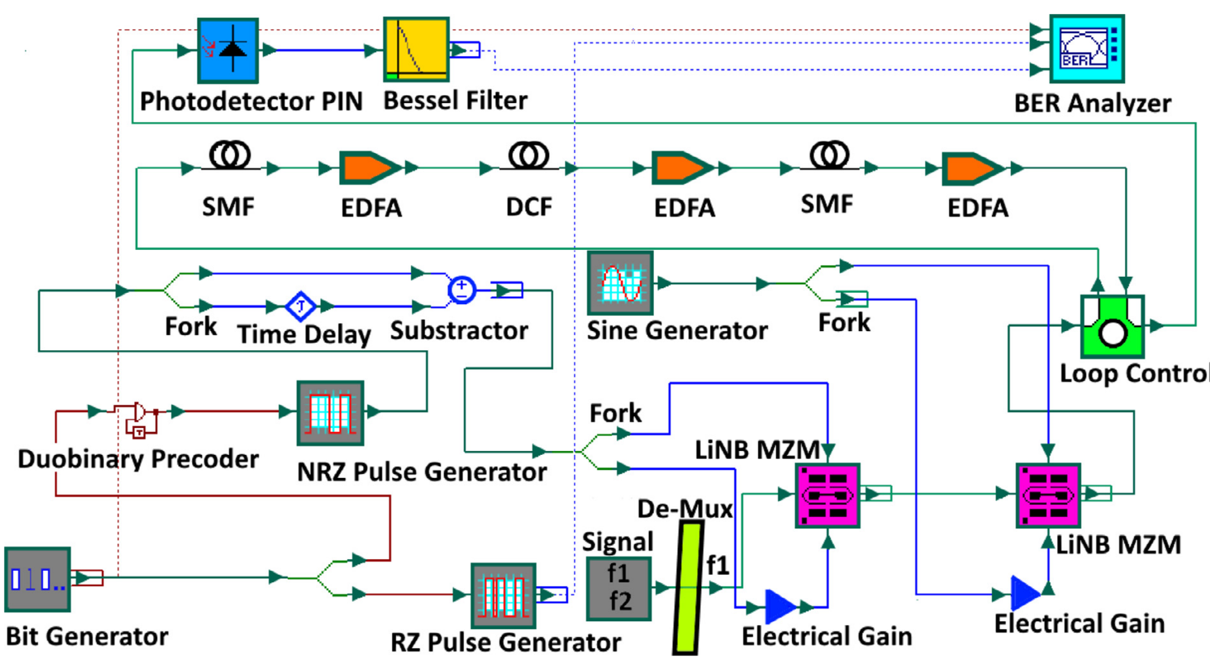

Fig. 5. System design of the optical duobinary modulation technique applied to modulate and transmit the optical signals (dual-wavelength) generated by the microring resonator shown in Fig. 3(c). The signals are generated using the microring resonator. A demultiplexer (de-Mux) is used to separate the two wavelengths from the dual-wavelength to perform two individual transmissions, SMF (single mode fiber), BER (bit error rate), EDFA (Erbium doped fiber amplifier), DCF (dispersion compensating fiber), MZM, NRZ (Non-return-to-zero).

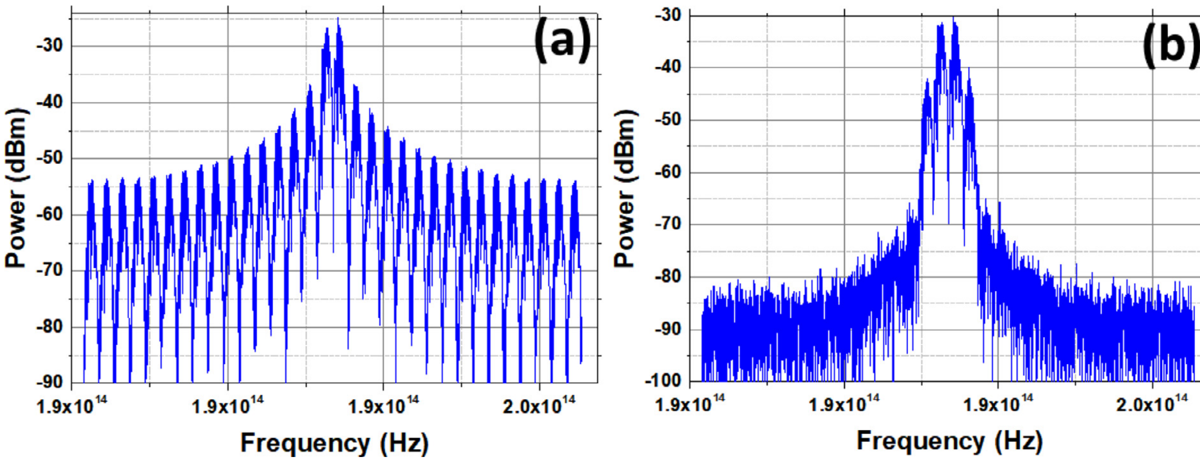

Fig. 6. (a) modulated optical signal after the first MZM, (b) after the second MZM.

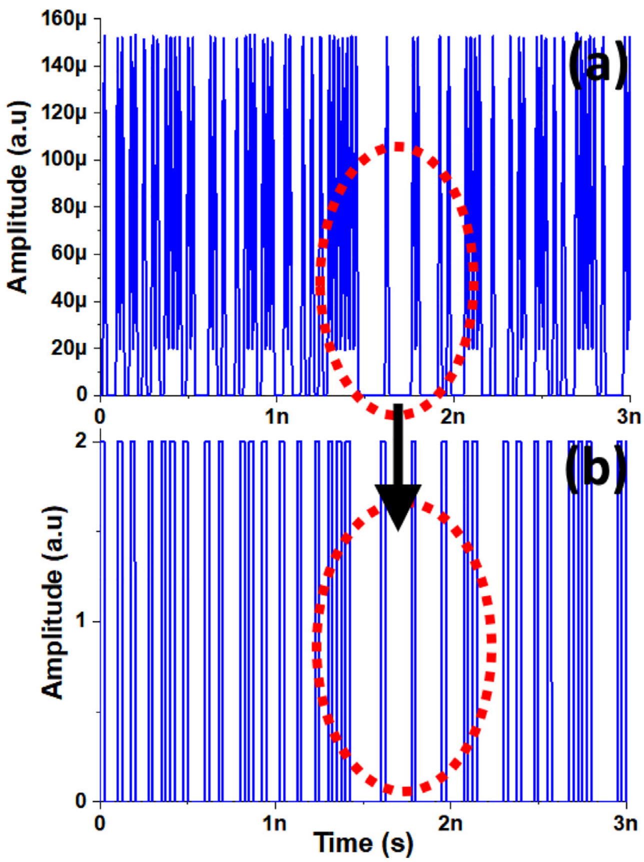

Fig. 7. Time domain results (a) initial modulating signals, (b) transmitted binary signals.

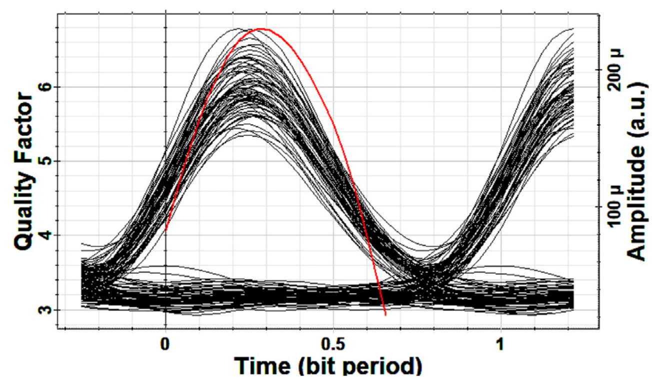

Fig. 8. Eye diagram of the transmitted signal at center wavelength 1540 nm for the input power 0.24 mW (−6.19 dBm), the quality factor is 6.78.

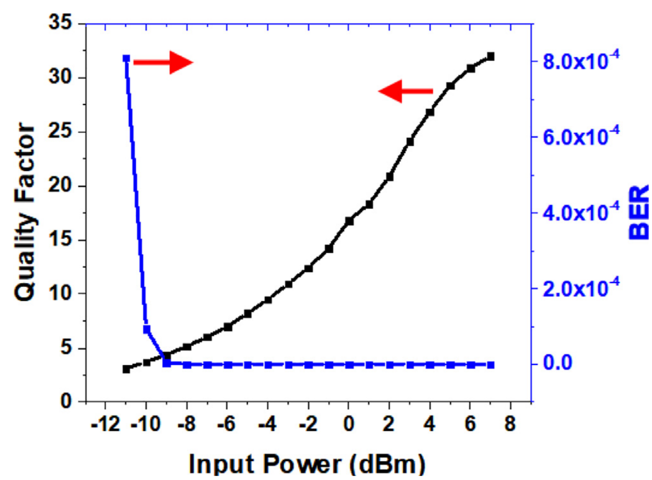

Fig. 9. Optical signal power versus quality factor and BER.

Results and discussion of the optical signals generated by microring resonator system

Fig. 3 shows the generated results from throughput, drop (1) and drop (2) ports. Dual-wavelength generation is performed within 33 nm range, where the THz free spectral range could be obtained. The drop port (2) output contains a dual-wavelength generated within 33 nm wavelength range, having a linewidth of 1.48 (185.320 GHz) and FSR of 3.95 nm (500 GHz). The simulations are carried over by photonic circuit simulator PICWave, where the PICWave employs flexible Time Domain Travelling Wave (TDTW) model from which the results presented in this paper are derived.

The rectangular waveguide (RWG) is used to describe waveguides or any guide by a modest number of rectangles. Similarly, the SWG (1D-slab waveguide structure) can be designed by the vertical profile of a slice, as like as SWG panel slices. The mode finder panel is located to monitor the intensity mode propagation as well as its corresponding mode profiles. Fig. 4 shows the fundamental mode propagation in the cross-sectional view of the waveguide.

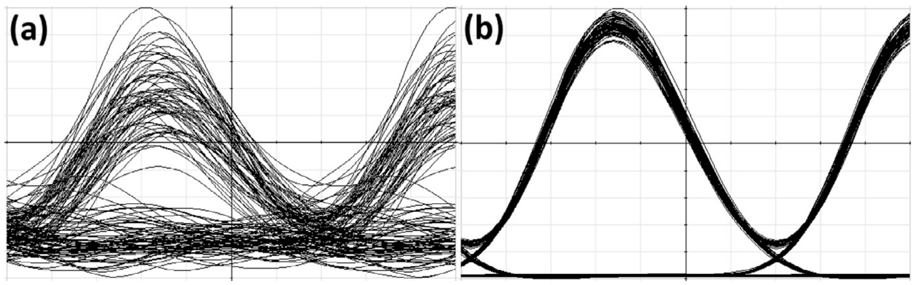

Fig. 10. Eye diagrams for (a) lowest input power (−11 dBm) and (b) highest input power (7 dBm).

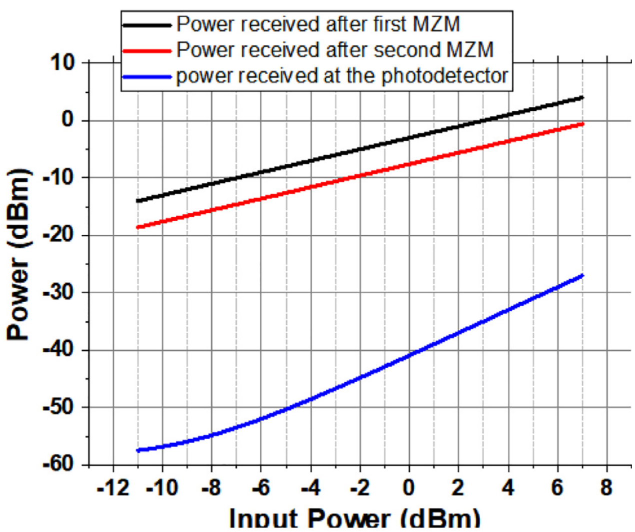

Fig. 11. Input power versus powers measured after the first MZM, second MZM and after the photodetector.

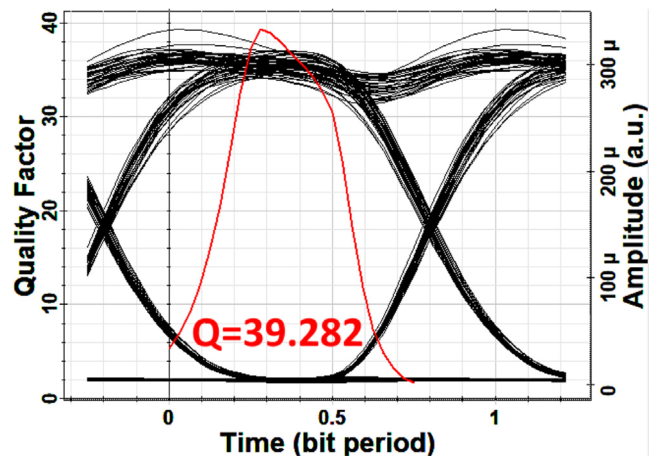

Fig. 13. Eye diagram of the transmitted second wavelength of the generated dual-wavelength shown in Fig. 3(c).

Proposed optical duobinary modulation technique

The system design is shown in Fig. 5. The bit rate of the bit sequence generator is 40Gbps, and the NRZ pulse generator has amplitude of 1(a.u). The NRZ pulse enters the electrical time delay with 1 bit time delay. The optical signal generated by the microring resonator has center wavelength of 1540 nm and 0.24 mW power as indicated in Fig. 3(c). Then the optical signal enters the first MZM to be modulated by the binary information signal, where the MZM has an extinction ratio of 100 dB. In the second MZM, the extinction ratio is 50 dB. Afterward the modulated optical signal will propagate through the optical fibers which have a length of 25 km, 0.2 dB/km of loss, 17 ps/nm/km of group velocity dispersion, dispersion group delay of 0.2 ps/km, a nonlinear refractive index of 2.6×10^{-20}, effective area of 70 μm^2, and a nonlinear phase shift of 5 mrad. The DCF is used to cancel

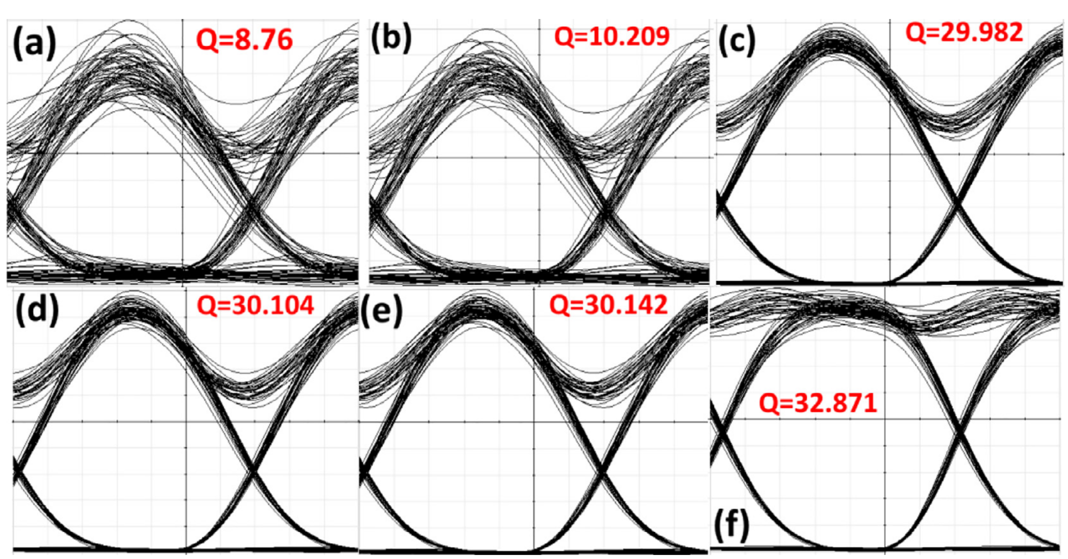

Fig. 12. System design optimization through applying different system parameters, (a) by reducing the sinusoidal pulse generator power, (b) by reducing the noise figure of the amplifiers, (c) by reducing the loops of the loop control, (d) by increasing the nonlinear refractive index of the first fiber link, (e) by increasing the nonlinear refractive index of the second fiber link, (f) replacing the sinusoidal pulse generator with a DC bias pulse generator.

out the created dispersion from the optical fibers and it has a length of 10 km, attenuation of 0.5 dB/km, and an ignorable dispersion index. The EDFAs is installed to reshape the pulse propagation along the provide optical link.

The optical signal generated by the microring resonator which is modulated by duobinary signaling scheme as presented well in [16] and later the modulated data will be detected by the PIN photo detector. Generation of modified duobinary pulses and its system configuration is shown in Fig. 1. The error free data modulation is succeeded by the presence of precoder and modulo 2 adder. During the detection process, the reshaping filtering center frequency is assigned as 32 GHz.

Results and discussion

The optical signal modulated by the information signals as generated duobinary signals is presented in Fig. 6. The optical signal is the first wavelength of the dual-wavelength generated by the microring resonator at wavelength 1540 nm.

The time domain of the initial and transmitted modulating binary signals is presented in Fig. 7. The result show that a very small-time delay occurs due to the fiber and other physical components, where the induced time delay is ignorable, and it does not affect the total performance of the system.

The eye diagram and the quality factor of the first modulated optical signal generated by the microring resonator at wavelength 1540 nm is shown in Fig. 8. The optical system has an average quality factor of 6.78 which is acceptable and shows an average performance of the system.

The quality factor of the system can be increased significantly by increasing the power of the optical signal generated by the microring resonator. The enhancement of the quality factor due to increasing the power of the optical signal is presented in the Fig. 9 as the BER is almost zero for the higher applied input powers. Fig. 10 shows the eye diagrams for the minimum and maximum input powers. The obtained quality factors are “0” and 32.3 respectively.

We have calculated the power received at the end of the first MZM, second MZM and the photodetector with respect to the variable input power of the optical signal. The result is shown in Fig. 11.

In the presented design system, the power degrades as the optical signal propagates along the optical fibers. In order to have better performance of the system the losses should be compensated either by the design optimizations or using the different modulation techniques. The used modulation technique as optical duobinary modulation is an efficient technique to perform the modulation especially for the optical systems and optical fiber transmission, therefore we perform further power and quality enhancements by the system optimizations. In the following section we have detailed the step by step optimization applied to the transmission system.

System optimizations and transmission of the second optical signal

Further optimization has been performed through the fiber link by changing the system parameters. The first optimization has been done by reducing the power of the sinusoidal pulse generator to 1(a.u) from 2(a.u) (shown in Fig. 12(a). The input power of the optical signal is fixed to 0.24 mW which is the power presented in the Fig. 3(c) for the wavelength center 1540 nm. We perform the optimizations without increasing the power of the optical signal but through the design parameters. We have reduced the noise figure of the amplifiers to 5 dB and could obtained much improved quality factor of 10.209 as shown in Fig. 12(b). The loop control has significant contribution to the quality factor performance of the system as we have decreased the number of the loops from 6 to 1 which leads to obtain very high-quality factor of 29.982 as shown in Fig. 12(c). The loop control can be utilized in systems which include amplifiers and the number of the loop will determine how many times the power can be amplified. It can be used to control the dispersion and prevents unnecessary usage of many amplifiers for a very long-distance transmission. The quality factor remains the same as the dark current of the photodetector changes. As the nonlinearity of the fiber is $2.6 \times 10^{-20}\,m^2/W$, we have done the optimization through changing the parameter. If the nonlinearity parameter increases to $3 \times 10^{-20}\,m^2/W$ the quality factor will increase to 30.104 as shown in Fig. 12(d). We have further improved the quality factor by increasing the nonlinearity of the second fiber to $7 \times 10^{-20}\,m^2/W$ shown in Fig. 12(e). We have found that if we replace the sinusoidal pulse generator with a DC bias pulse generator as electrical signal input into the second MZM the quality factor can be enhanced to 32.871 shown in Fig. 12(f).

We have examined the second wavelength of the generated dual-wavelength shown in Fig. 3(c) which has power of 0.29 mW and a center wavelength of 1545 nm. The eye diagram of the transmitted modulated optical signal is presented in Fig. 13. The maximum quality factor obtained for the second wavelength transmission is 39.282 as an advantage, a higher output power has been obtained compared to the first wavelength transmission.

The transmission of the second wavelength has been performed after the optimization has been applied to the optical fiber transmission system. In this case the BER is almost zero which means a very high-quality transmissions of the optical signals generated by the microring resonator has been performed through the optical fiber communications using the optical duobinary modulation scheme.

Conclusion

We have conducted a research to perform the optical duobinary modulation technique to transfer two wavelengths (optical signals) from a generated dual-wavelength in microring resonator systems. The two generated wavelengths have center wavelengths of 1540 and 1545 nm where these have been modulated by the duobinary signals using the Lithium Niobate (LiNbO3) Mach Zehnder modulator (MZM). The received modulated optical signals show a high-quality signal and these have high quality factor and lowest BER which are necessary to evaluate an optical communication system. The modulation can be performed by using differential precoding and electrical or optical filtering. The generated results show a high performance for optical signal transmission in an optical fiber communication. The high-quality factor could be achieved by performing the system optimization, where the highest quality factor of 39.282 has been obtained for the optimized design for the optical signal modulation and transmission at wavelength 1545 nm.

Acknowledgment

Dr. Zakaria would like to acknowledge the financial support from FRGS Grant FP034-2017A.

References

[1] Bruck R, Mills B, Thomson DJ, Troia B, Passaro VM, Mashanovich GZ, et al. Picosecond optically reconfigurable filters exploiting full free spectral range tuning of single ring and Vernier effect resonators. Opt Express 2015;23:12468–77.
[2] Yu J, Jin S, Wei Q, Zang Z, Lu H, He X, et al. Hybrid optical fiber add-drop filter based on wavelength dependent light coupling between micro/nano fiber ring and side-polished fiber. Sci Rep 2015;5:7710.
[3] Ranjan S, Mandal S. Performance analysis of triple asymmetrical optical micro ring resonator with 2× 2 input-output bus waveguide. Braz J Phys 2018;48:74–84.
[4] Sarrigan G, Matori K, Amiri I, Ahmad H, Fadaeifard F. Dual-wavelength generation with terahertz spacing using GaAs–AlGaAs microring resonator waveguides. J Comput Theor Nanosci 2017;14:330–4.
[5] Ji X, Barbosa FA, Roberts SP, Dutt A, Cardenas J, Okawachi Y, et al. Ultra-low-loss on-chip resonators with sub-milliwatt parametric oscillation threshold. Optica 2017;4:619–24.
[6] Amiri I, Bunruangses M, Chaiwong K, Udaiyakumar R, Maheswar R, Hindia M, et al. Dual-wavelength transmission system using double micro-resonator system for EMI healthcare applications. Microsyst Technol 2018:1–9.
[7] Amiri I, Alavi S, Soltanian M, Fisal N, Supa'at A, Ahmad H. Increment of access

points in integrated system of wavelength division multiplexed passive optical network radio over fiber. Sci Rep 2015;5:11897.
[8] Pelc JS, Rivoire K, Vo S, Santori C, Fattal DA, Beausoleil RG. Picosecond all-optical switching in hydrogenated amorphous silicon microring resonators. Opt Express 2014;22:3797–810.
[9] Noury A, Le Roux X, Vivien L, Izard N. Enhanced light emission from carbon nanotubes integrated in silicon micro-resonator. Nanotechnology 2015;26:345201.
[10] Camacho-Morales R, Rahmani M, Kruk S, Wang L, Xu L, Smirnova DA, et al. Nonlinear generation of vector beams from AlGaAs nanoantennas. Nano Lett 2016;16:7191–7.
[11] Kaur R, Dewra S. Duobinary modulation format for optical system-a review. Int J Adv Res Electr Electron Instrum Eng 2014;3:11039.
[12] Abbood ANA, Al-Raweshidy H. Reduction of bandwidth requirement in DRoF systems using optical duobinary modulation. Computer science and electronic engineering (CEEC) 2017. IEEE; 2017. p. 116–21.
[13] Vishwakarma S, Dutta M. Generation of spectral efficient modulation format for fiber transmission by hybridization of duo binary and Manchester. Communication and computing systems: proceedings of the international conference on communication and computing systems (ICCCS 2016), Gurgaon, India, 9–11 September, 2016. CRC Press; 2017. p. 347.
[14] Sun C, Bae SH, Kim H. Transmission of 28-Gb/s duobinary and PAM-4 signals using DML for optical access network IEEE Photon. Technol Lett 2017;29:130–3.
[15] Krishna VR, Tiwari V. Comparison of duobinary and modified duobinary modulation schemes for optimized transmission at 40 Gbps, Wireless and Optical Communications Networks (WOCN), 2015 Twelfth International Conference on, IEEE, 2015, pp. 1–4.
[16] Ye Z, Li S, Cheng N, Liu X. Demonstration of high-performance cost-effective 100-Gb/s TWDM-PON using 4× 25-Gb/s optical duobinary channels with 16-GHz APD and receiver-side post-equalization, Optical Communication (ECOC), 2015 European Conference on, IEEE, 2015, pp. 1–3.
[17] Sabapathi T, Gayathri R. Simultaneous reduction of four wave mixing and stimulated raman scattering using duobinary modulation format in DWDM Fiber Optic Communication System. Int J Sci Eng Technol 2014;3:634–7.
[18] Kippenberg T, Spillane S, Vahala K. Kerr-nonlinearity optical parametric oscillation in an ultrahigh-Q toroid microcavity. Phys Rev Lett 2004;93:083904.
[19] Del'Haye P, Schliesser A, Arcizet O, Wilken T, Holzwarth R, Kippenberg T. Optical frequency comb generation from a monolithic microresonator. Nature 2007;450:1214–7.
[20] Amiri IS, Ariannejad M, Azzuhri S, Anwar T, Kouhdaragh V, Yupapin P. Vertical Ge photodetector base on InP taper waveguide. Results Phys 2018;9:576–9.
[21] Ariannejad M, Amiri IS, Ahmad H, Yupapin P. A large free spectral range of 74.92 GHz in comb peaks generated by SU-8 polymer micro-ring resonators: simulation and experiment Laser. Physics 2018;28:115002.
[22] Amiri IS, Anwar T, Zakaria R, Yupapin P. TE-like mode analysis of microsystem InGaAsP/InP semiconductor resonator generating 20 GHz repetition rate pulse trains. Results Phys 2018;10:980–6.
[23] Amiri IS, Alizadeh F, Ariannejad M, Amini R, Yupapin P. Computation of Ion exchange buried microring resonator waveguide for THz communication applications. Results Phys 2018.
[24] Amiri IS, Ariannejad M, Daud S, Yupapin P. High sensitive temperature sensor silicon-based microring resonator using the broadband input spectrum. Results Phys 2018;9:1578–84.
[25] Lévêque G, Mathevet R, Weiner J, Des Francs GC, Girard C, Quidant R, et al. Modelling resonant coupling between microring resonators addressed by optical evanescent waves. Nanotechnology 2004;15:1200.
[26] Amiri I, Ahmad H, Ghasemi M, Ismail M, Aidit S, Soltanian M, et al. Silicon-based microring resonators for multi-solitons generation for THz communication. Opt Quant Electron 2016;48:415.

Results in Physics 11 (2018) 306–314

Contents lists available at ScienceDirect

Results in Physics

journal homepage: www.elsevier.com/locate/rinp

Performances and procedures modules in micro electro mechanical system packaging technologies

Iraj S. Amiri[a,b,*], M.M. Ariannejad[c], D. Vigneswaran[d], C.S. Lim[e], P. Yupapin[a]

[a] Computational Optics Research Group, Advanced Institute of Materials Science, Ton Duc Thang University, Ho Chi Minh City, Viet Nam
[b] Faculty of Applied Sciences, Ton Duc Thang University, Ho Chi Minh City, Viet Nam
[c] Photonics Research Centre, University of Malaya, 50603 Kuala Lumpur, Malaysia
[d] Department of Electronics and Communication Engineering, Sri Krishna College of Technology, Coimbatore 641 042, India
[e] Department of Mechanical, Materials and Manufacturing Engineering, University of Nottingham Malaysia Campus, Jalan Broga, 43500 Semenyih, Selangor Darul Ehsan, Malaysia

ARTICLE INFO

Keywords:
Micro electro mechanical system (MEMS)
Die-level packaging
Thin-film packing
Vacuum package

ABSTRACT

This paper presents the challenging issues in micro electro mechanical system (MEMS) packing technologies. The MEMS package includes a MEMS device and a signal conditioning electronic circuit. In one viewpoint, MEMS application is categorized by the type of sensor, actuator, and structure. MEMS technology applications in general domains are automotive, consumer, industrial, biotechnology and commercial applications. Few methods such as the low power oven, vacuum, and silicon glass packages were discussed. The major technique as die level and wafer level of packing including thin-film packing were reviewed in this paper. The problem of several failure mechanisms and challenges and their solutions were discussed in this review.

Introduction

Similar to IC technologies, many processes are required to do the electromechanical system (MEMS) packaging. These can be such as environmental and mechanical supports and management paths. The electrical signal paths can be redistributed by performing the packaging as it can be changed to the larger and more manageable interconnection opportunities from tight pad dimensions. The damages from stress and solidity can be avoided by the mechanical supports. In an ideal packaging scheme, the power distribution is an important issue. In order to sustain function over the product lifetime, the heat transport should be managed and controlled efficiently by the thermal management [1–3].

Many applications are included in the MEMS technologies, as it is a building synergy between many un-relevant technologies such as biology and micro-electronics and recent technologies such as those in nanoscience and nanotechnology. This approach can be used to emerge in many new applications and therefore expending the research which is identified currently. Mechanical protection parts are used widely for research fields such as bio-MEMS, where the microfabrication is required to pursue the biological investigations. The electronic components can be utilized to move objects in the sub-millimeter scale, therefore, providing radio frequency functionality which is applicable in radio frequency microelectromechanical systems (RF MEMSs). Several radio frequencies use the above functionality although due to the rapid developments of the MEMS technology and diversity of the MEMS products, there are many difficulties and complexities in MEMS packaging which cause many other problems and issues such as microstructure protection which is necessary to avoid silicon dust chip destruction, silicon wafer cutting, substrate modifications, and device interfaces problem [4].

ICs packaging and MEMS packaging at glances

In the MEMS packaging and ICs packing, there are some differences. The main issue is to support the chip physically and provide the electrical connection to the active chips, ground interconnections, power, supply signal and heat dissipation. The chip should be isolated to keep it away from the environmental effects. Fig. 1 illustrates the comparison between a MEMS pressure sensor package and a typical dual in-line package (DIP) IC package which has an opening window to sense the pressure variation. The MEMS devices need to be used under the harsh condition like automobile hoods, acids, and alkaline surrounding. The package should be strong enough to work in different and difficult situations [5–7].

* Corresponding author at: Ton Duc Thang University, Ho Chi Minh City, Viet Nam.
E-mail address: irajsadeghamiri@tdtu.edu.vn (I.S. Amiri).

https://doi.org/10.1016/j.rinp.2018.09.008
Received 10 July 2018; Received in revised form 4 September 2018; Accepted 5 September 2018
Available online 08 September 2018

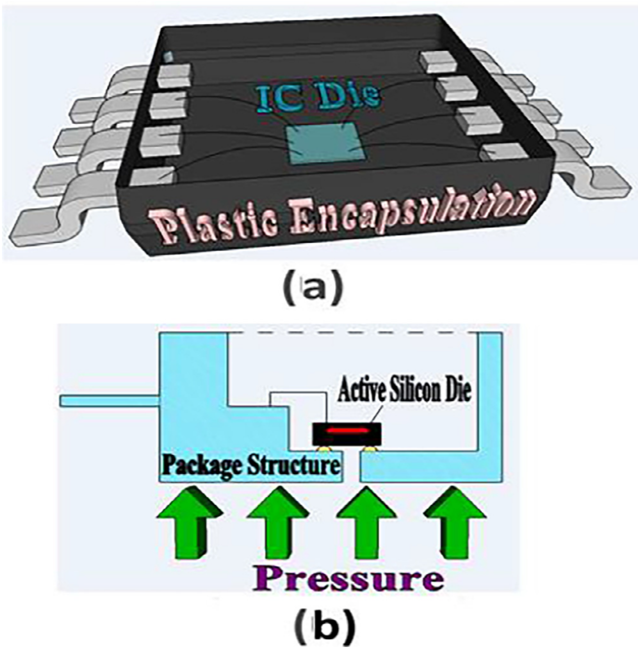

Fig. 1. (a) General IC packaging & (b) Pressure sensor using MEMS IC.

Consideration for MEMS packaging

The interconnection, protection and also other conditions would be considered in the MEMS packaging processes. The MEMS technology can provide the package for die or wafer size. Die-level packaging can be used as ordinary so that the wafer level in packaging can be a good method for MEMs technology. To decrease the stress in a packaging house the ceramic packaging would be a good option. In Table 1, the wafer level packaging and the die-level packaging have been discussed [8].

MEMS reliability, key failure mechanism, and challengers

The packaging of MEMS in some aspect can be complicated due to provide protections from the environmental conditions as in many applications such as sensors the produced device must be in contact with the environments to measure the desired parameters. Due to the very small size of the MEMS devices compared to other mechanical devices, adhesion, and friction which are kinds of source forces occurs and lead to failure of the devices. Other challenges can be keeping the device components from the contaminants, where it is very necessary in order to perform efficient device with a good response and functionality. The reliability is the key and important feature that MEMs should consider within this so that a lot of advantages would be sacrificed. Similar common methodologies could be improved by qualification and the reliability. The main issues for the failure in the MEMS can be included as [9]:

Table 1
Different between die-level packaging and wafer level packaging.

Die-level packing	Wafer level packing
Common MEMS IC packaging technology	Peculiar for MEMS IC packaging
The pack of MEMS components consists IC components that are in package housing	The extra process in fabrication requires using of micromachined for the wafer which is bonded to a second wafer thus it can make a very good cavity that etched into it
Die is attached to a package with glues The die also can be glued	This method leaves the microstructure free to move within an inert gas or atmosphere vacuum
The interconnection between die and package pads are made of wire bonding	
The package housing can also be protected by using the encapsulated or it can be sealed	

- Wear and stiction failure

Another failure in the IC system is the soldering of joints that cause the thermal cycle issues. Wear and stiction can be the most failures in MEMS packaging. The microscopic adhesion can be a failure when two surfaces are in contact which is stiction. One solution can be implemented by performing the separation on the microscopic scale.

- Environmental conditions can cause the failure

Failure due to humidity, radiation effect, shock, thermal cycling, vibration etc. are common in the case of IC packaging systems. The mechanical parts which are available in the MEMS devices can cause this sort of failure.

- Mechanical cyclic issues

This can be issued by the marital that can make some failure for membrane and comb in MEMS devices. If some stress implements during the loading, it also can make a serious failure in MEMS sensors.

- Dampening effect

This effect cannot be serious and significant, but in the case of MEMs packaging, it also can be considered, examples such as moving parts in the resonant frequency.

- Delamination

The bonding of the surface with the thin film is considered an important issue, where it can reduce the performance and system functionality, in some cases it can even change the martial characteristic [9].

Challenges in MEMS packaging

Interconnect: The MEMES technology provides highly integrated and small size that can bring the electricity to the chip due to the input and output requirements. For this feature, the complex packing can be advisable.

Protection: To connect the chip to the outside world, the issue of the fragile makes more sensitivity on it and the package should be secure enough to tolerate with such harsh conditions.

Hermiticity: As it differs from IC devices, the MEMS devices in mechanical and chemical sensors require hermetic or special ambient to operate.

Precision: The MEMS devices are fabricated to work in tough condition with less tolerance [8].

Material of MEMS packaging

The adhesive material is commonly used for attaching die onto the wiring board that is printed (PWB) in Chip on Board (COB) packaging of MEMS devices. Three kinds of adhesive materials, as well as two cap materials for COB packaging, can be considered in the MEMS microphone. Three different adhesive materials, namely 2025D, 3140RTV and SDA6501. The thickness of the adhesive material is the critical parameter to control the thermal stress in the diaphragm due to the

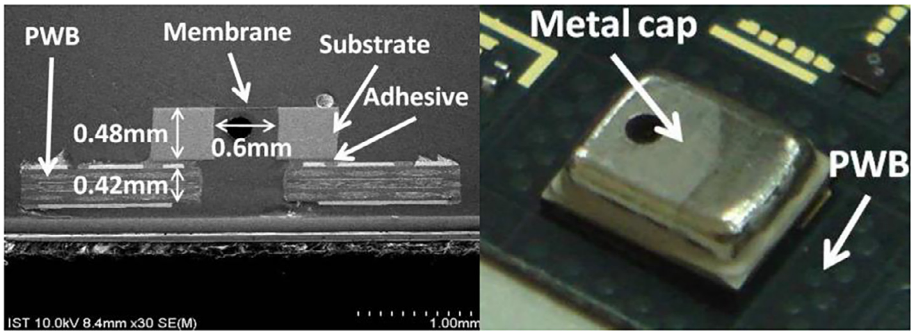

Fig. 2. Silicon microphone chip packaged by COB packing. The cross-section of the chip (b) Metal cap packing.

heating process.

Soft adhesive materials (3140RTV and SDA6501) have better mechanical isolation of PWB thermal deformation due to the buffer layer effects. On the contrary, hard adhesive material (2025D) could be affected by PCB thermal deformation by the thickness of adhesive. Consequently, a soft adhesive material with low CTE value is better for COB packaging of MEMS device with the diaphragm, such as microphones, pressure sensors and so on [10,11] (as illustrated in Fig. 2).

Methods

There are few methods as a low power oven, vacuum and silicon glass packages which are discussed in this review. The major techniques die and wafer level of packing included thin-film packing was explained.

1) *Higher performance by using the low power oven to control the vacuum in packaging*

Low-power oven controlled thermal environment as well as the vibration isolation which uses for achieving packaging approach in an efficient manner. In this way, the vacuum package has very strong isolation platform which can be used to support the MEMS devices. Therefore, the MEMS devices can be isolated from the external environment using the vacuum package either mechanically or thermally. Fig. 3 shows the structure of the package, that consist of three important components; (i) with the usage of suspensions which is 100 gm-thick glass we can provide a platform substrate in case of mechanical and thermal isolation, (ii) the flip-chip can be attached to the platform and the MEMS device, therefore, can be supported (iii) for providing the final vacuum encapsulation, the vertical feed can be incorporated with a package cap. The oven will provide the thermal stabilization which is necessary to control the device at a higher temperature than that of environment temperature. Using a new heater and also a temperature sensor posited in the isolation platform could be useful for the thermal stabilization.

In the case of utilizing high-performance micro instruments, good packaging can be provided by utilizing the low power oven-controllable vacuum package technology. Therefore, high protections from thermal and mechanical effects can be provided by using the package, where the glass isolation suspensions are utilized. In order to package a wide range of MEMS devices, the most efficient technology as the wafer-level packaging can be utilized. This type of packaging has been shown in Fig. 4.

Using the packaging shown in Fig. 4, long-term vacuum encapsulation which provides robust vertical feedthrough can be performed. Many different high-performance MEMS devices can utilize the mentioned approach which is well suitable for such devices. These devices can be such as those used in optoelectronics or photonics such as accelerometers, low power oven control devices, resonators, infrared imagers, and vacuum packaging for stable operation [12].

2) *Anodic bonding (electrostatic) for silicon glass packaging*

One of the well-known methods for bonding in MEMS is bonded between the polished silicon and glass (Pyrex 7440) with the usage of the electrostatic process it also called anodic bonding [13]. Silicon glass [14] packages with anodic (electrostatic) bonding can be used in silicon glass packaging with the use of a custom glass capsule, which is hermetically sealed with a cavity (Fig. 5).

There are a lot of advantages of using silicon glass packages. One of the usages is in biomedical, MOEMS and MEMS switches in RF [16] applications as the silicon glass are transparent to RF signals. The Pyrex type of glass is resistant, biocompatible and resistant to a lot of available corrosive around us, for example, moisture and the salted water [15].

3) *Bonded a gold ring with the silicon cap*

Vacuum packaging with the gold bonding ring and a silicon cap wafer with a polysilicon bonding ring can be developed as illustrated in Fig. 6. This type of bond can be achieved to improve more than 95% produced over the whole wafer, where the eutectic has the ability to drift over the surface that is not planar. Fig. 6 shows the isolated feed that has the transmission of signals between the sealed package and outside.

4) *Silicon and gold eutectic bonding with field-assisted*

The cleaning of the surface is necessary for this method. The interdiffusion of the two different kinds of materials can issue the intimate contact. An innovative technique has been used recently on both anodic bonding Si-Au and eutectic [16]. The Ti/Au 200 Å/10,000 Å amount will be evaporated on the specific silicon wafer. The cup wafer in addition to the platinum area, on the Si wafer, tends to be divided by ~500 µm red flags in addition to from then on located within the electronic processes and electrostatic bonder. The wafers tend to be warmed to 350 °C. The air-filled appropriate slot is often evacuated for some demand linked to 90 µ Torr. The wafers tend to be warmed more than 400 °C wherein the actual Si and also in addition to Au inter-diffuse to make Si-Au eutectic as a fluid solder. The wafers tend to be brought into a 100 N demand. The voltage associated with 100 V for a short time, 500 V for 5 moments and in addition to 1000 V for 5 times more, will be employed between the silicon wafer and the Pyrex wafer. The voltage will probably cut off; the actual appropriate slot will probably be vented to 1 atmosphere in addition to chill the area in case of temperature issues. After the temperature of the wafer goes up to 350 °C, we should be certain about the actual solder that will probably be re-solidified and the actual 100 N demand will be taken off. The production related to the thin-film solder, as well as the silicon wafer, is very strong and standard so that the wafers cannot be divided. A photograph of the bonded wafers illustrated in Fig. 7 [16].

By making use of a good anodic bias that is typically applied inside the direct Si-glass wafer holding and a normal Si-Au eutectic bond we can purchase the top improvement in case of the top quality uniformity, in addition to reproducibility [17]. This particular strategy which is completely new may make very important role to enables the wafer bonding. The electrostatic may assure to have close contact between the Si-Au solder. In addition to a glass interface regularly more big parts, which will be necessary intended for wafer-level holding also can be of

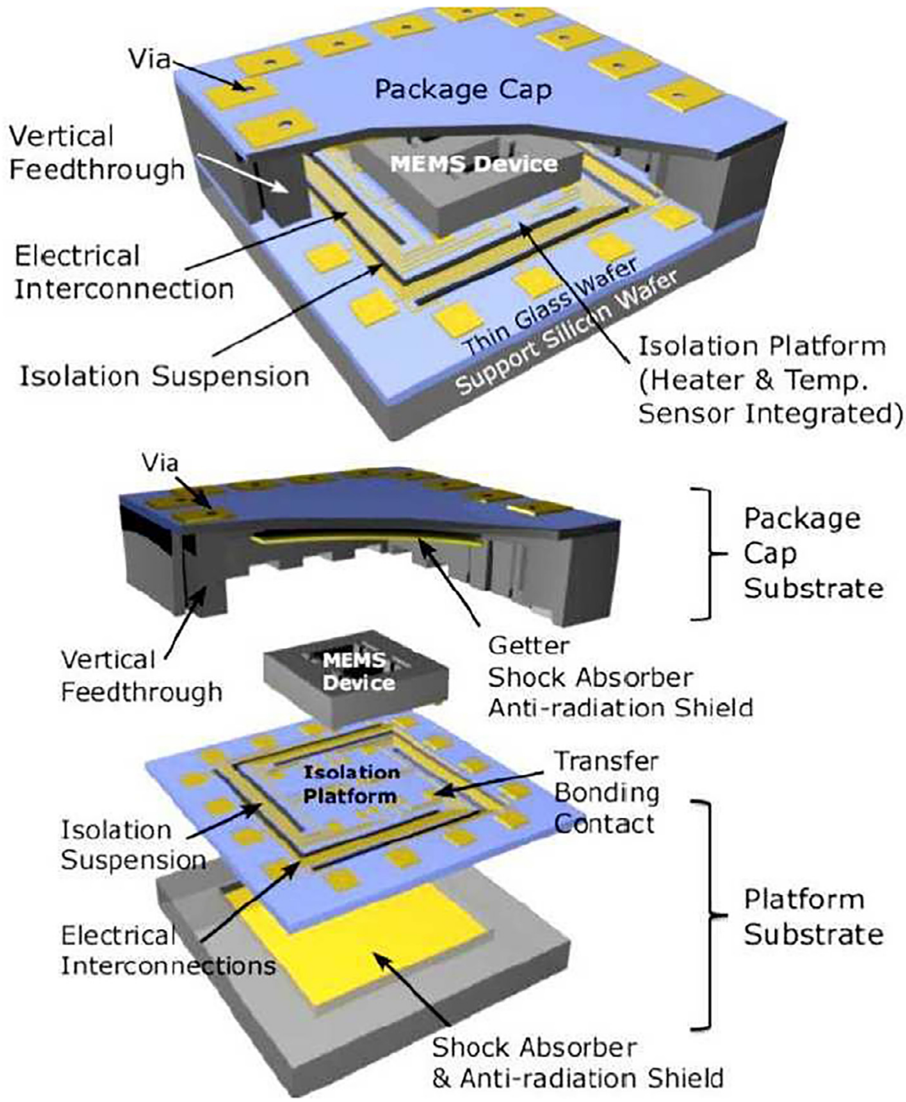

Fig. 3. A detailed exploration of the MEMS package [12].

hermetic effects [16].

5) *RF–MEMS wafer-level packaging using through-wafer interconnect*

RF MEMS Wafer Amount packaging commonly has been performed by simply rerouting the actual electric interconnect through the product wafer and the front facet, as for the bottom, the through-wafer interconnect has been utilized, therefore bonding of the actual capping substrate that is a front facet of the product wafer could be performed. Alternatively, the actual RF–MEMS engineering frequently will involve 'dirty' operations, which might be not necessary and appropriate for the conventional IC cleanroom engineering that may be used for manufacturing regarding silicon circuitry. The other handles circuitry chips are flip-chip bonded by using tooth cavity onto the actual RF–MEMS product wafer. The cavity, with appropriate pattern, could be employed as wafer-to-wafer case windows after the wafer placed. With respect to the height of the RF–MEMS gizmos, optional plasma-etched recesses from the capping wafer may be required. By linking to the packaging procedure at the wafer level, a singulation is dissipated with normal conduction to this surface-mount technology (SMT) which is an acceptable element [18]. This kind of alternative can be schematically displayed in Fig. 8.

Relating to examining function, RF–MEMS units and RF passives were created for the RF–MEMS wafers. The Plated silver had been utilized because of finishing the metallization level through which can shield to solder reflow bonding. This kind of level can be used by perishing stage hermetic shutting. High resistivity silicon (HRS) is needed for pertaining in both RF–MEMS and the capping substrate. The specific components can be finalized, where the mixed energy extension coefficients and stability are greater. The process of development was some sort of WLP remedy pertaining to RF–MEMS programs which usually permits co-integration involving in CMOS circuitry as well as on-chip passive units which are illustrated in Fig. 9 [19].

Problems in the analysis of thin-film nitride MEMS

MEMS product packaging procedures are unable to immediately comply with the procedures through the IC product packaging sector as a result of being feasible to free-standing actual physical microstructures and a substance which often is unable to make the dicing as well as pick-and-place actions prior to the sealing issue. Additionally, a few MEMS offers ought to be specially built to accommodate the functionality of the MEMS system. The thin-film fabrication will be the strategy to fabricate wafer-level bundles simply by using the micromachining technological innovation. In comparison with this technological innovation, there are several positive aspects for instance:

- Firstly, how big this sort of thin film could be to obtain the contribution with micrometers, which usually suits this trend with miniaturization from the electrical power items.

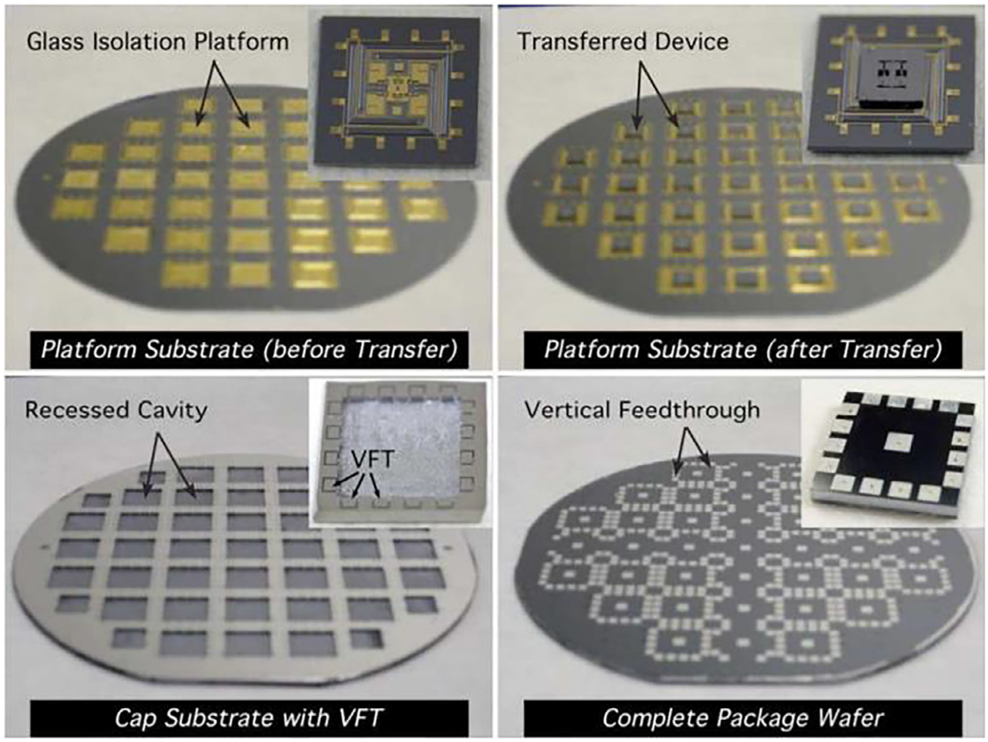

Fig. 4. Wafer- and die-level pictures of the fabricated substrates [12].

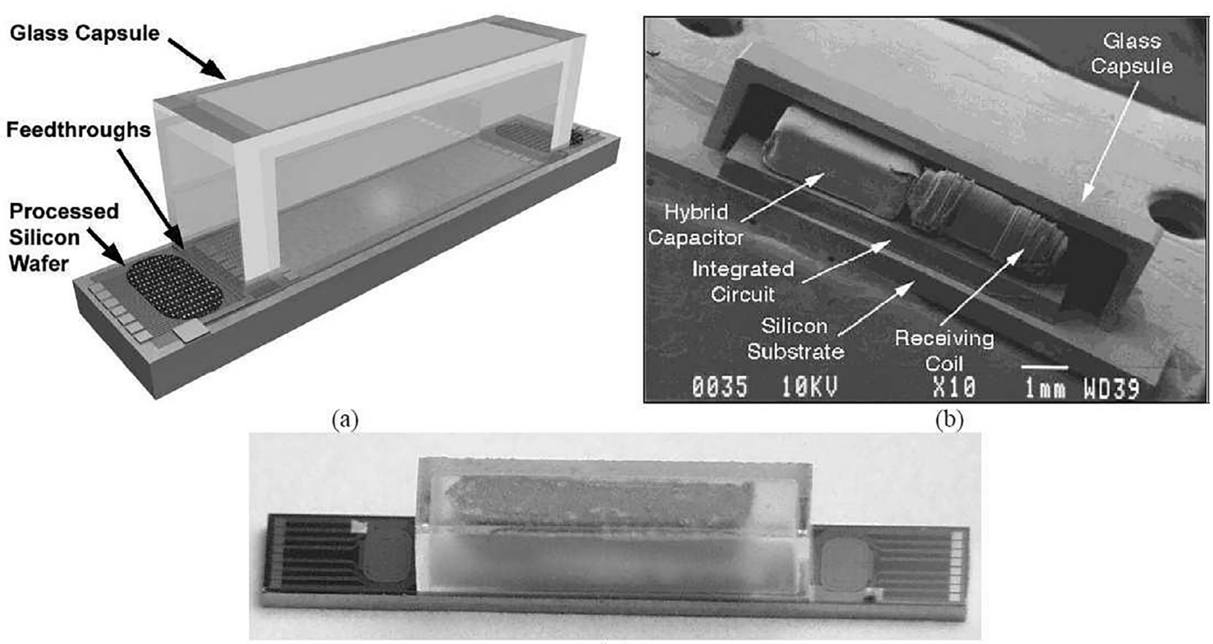

Fig. 5. The usage for biomedical with silicon glass, (a) silicon glass structure, (b) the implantable and SEM photo, (c) A finalized package [14].

- Secondly, this thin-film offer requirement as less area around the wafer in comparison to connection tactics, significantly minimizing the price. Next, most thin-film will be MEMS manufacture compatible thus it can be incorporated within the MEMS practice. The idea allows adaptability, particularly and higher efficiency at correct eradicating contaminants to that of the exterior environment. Due to the size of the thin-film that can offer, examining of a thin-film vacuum MEMS can be done simply by traditional tactics, for instance, Helium outflow test out will be tough considering that it indicates the exceedingly modest. To confirm this vacuum level inside, a built-in MEMS clamped-clamped column resonator can be used. The functionality from the MEMS resonator depends on the standard of this technique. Oxygen damping can resist this motion from the resonant aspect, as a growth of the background force will result in some sort of decrease in the product quality component (Q) from the resonator within a specific force array.

This thin-film package can be included within 3 mTorr. Nevertheless, this ensuing stress inside the package which would seem to get bigger and conclude force. The actual high stress inside the

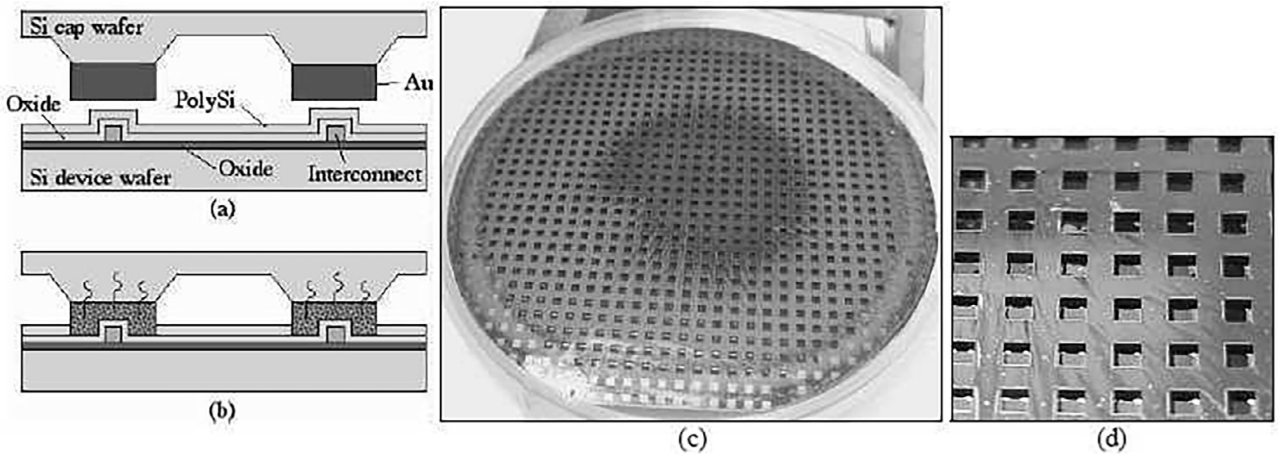

Fig. 6. (a) and (b) the diagram of Au Si that has eutectic bonding. (c) A 4 in. silicon package. (d) Photo of the dies that packaged [14].

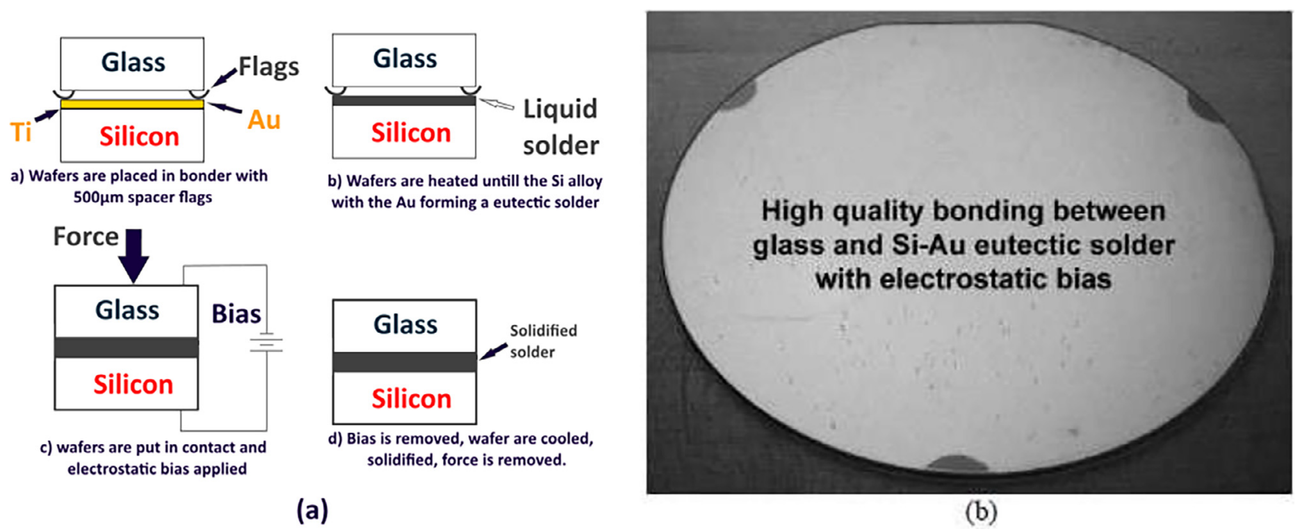

Fig. 7. (a) Glass towards the Si-Au eutectic solders anodic bonding. (b) 4 in. cup wafer bonded to the silicon wafer using the particular anodic Si-Au eutectic procedure [14].

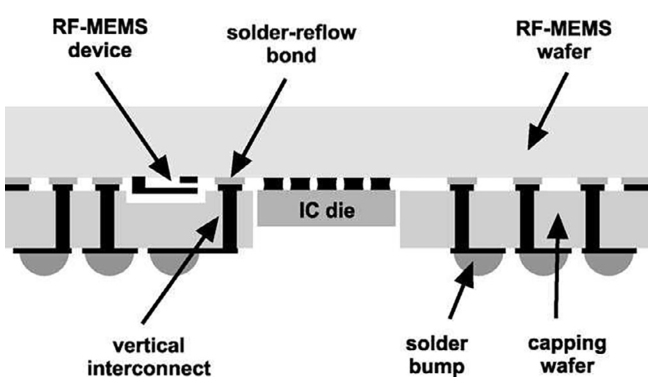

Fig. 8. A precise resistivity for silicon capping wafer [19].

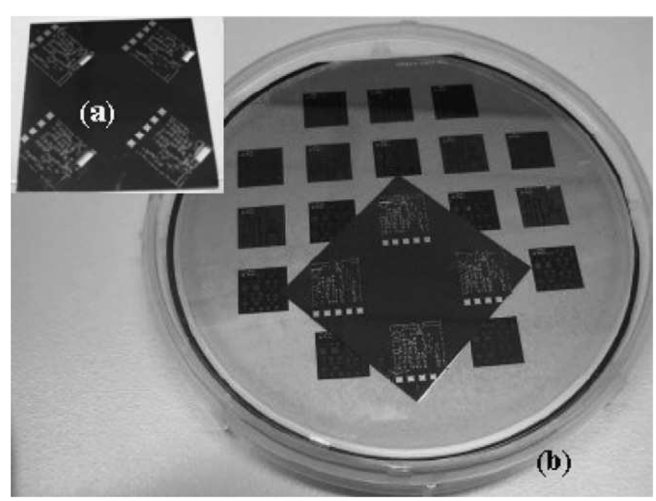

Fig. 9. Wafer-level packaging solution for RF–MEMS (a) Capping (b) after bonding to the device wafer [19].

package can be considered due to the exact outgassing of the internal silicon nitride during the nitride phase. To recognize the microstructure of thin-film nitride package, supplementary ion size spectrometry (SIMS) research of the package can be accomplished. The actual arrangement of the thin-film appearance is found by means of bombarding the surface of the package using a centered principal ion lighting order in addition to analyzing this thrown supplementary ions (Figs. 10 and 11).

The inability of a thin-film bundle is analyzed through a test. The key reason for this inability was investigated by applying SIMS research to quicker testing with the appearance substance. The explanation for

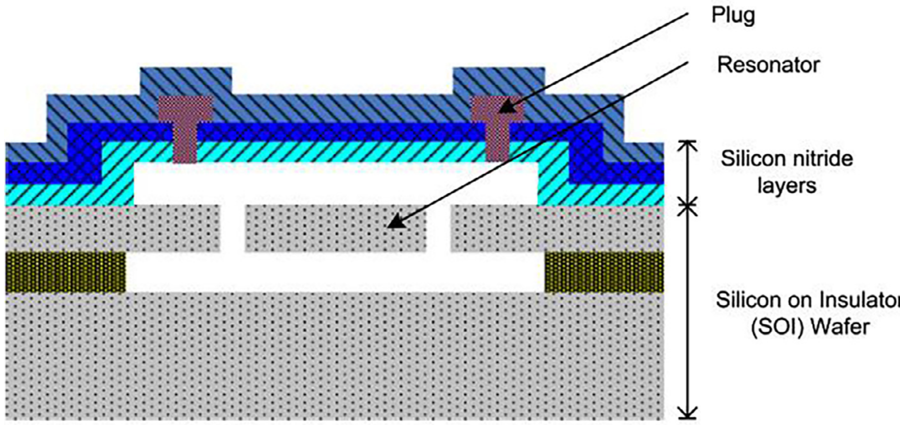

Fig. 10. Thin-film packaged resonator in cross-section [20].

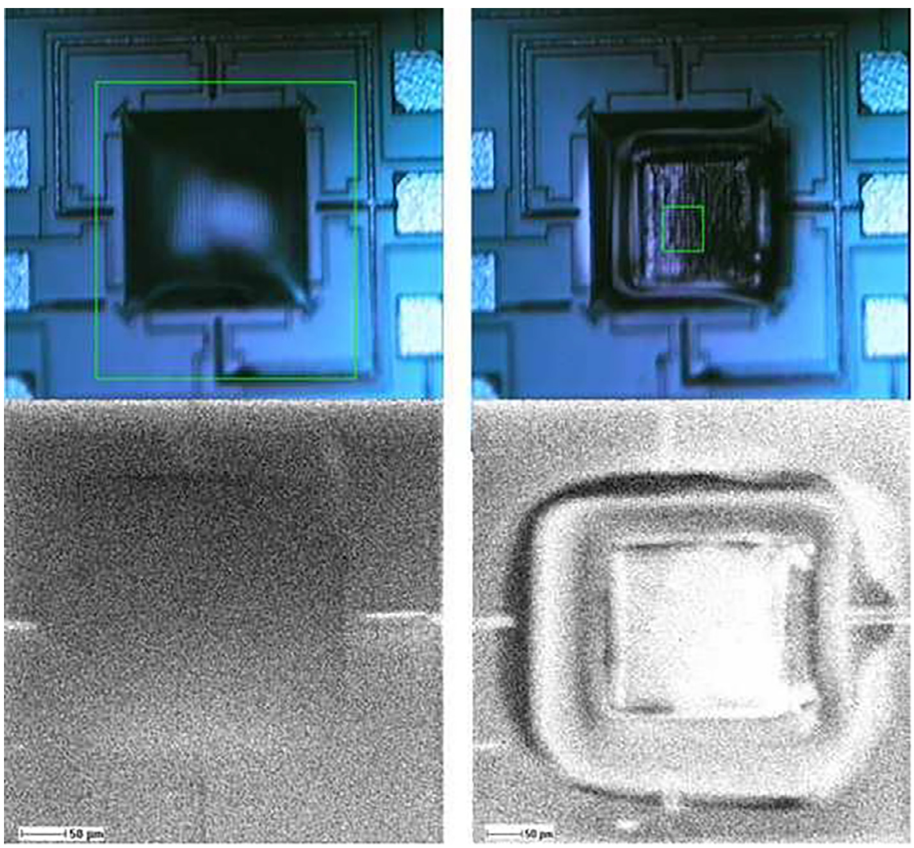

Fig. 11. Before (left) and soon after (right) depth profiling of the thin-film nitride package. Prime line: camera pics, bottom line: total ion photographs [20].

Table 2
Existing packaging parameters, challenges, and solution for MEMS.

Packaging parameters	Challenges	Solutions
Release and stiction	Stiction of devices	Freeze drying, supercritical CO_2 drying, roughening of contact surfaces, non-stick coatings
Dicing	Contamination risks	Release dice after dicing, flush chip surface to remove contaminants
Die handling	Device failure, top die face is very sensitive to contact	Fixtures that hold MEMS dice by sides rather than top face
Stress	Performance degradation and resonant frequency shifts	Low modulus die attach, annealing, the compatible coefficient of thermal expansion (CTE) match-ups
Outgassing	Stiction, corrosion	Low outgassing epoxies, cyanate esters, low modulus solder, new die attach materials, removal of outgassing vapors
Testing	Possible device failure after many assembly steps	Post-release, pre-packaged, and/or package testing

Table 3
Significant standard design troubles associated with the typical RF MEMS as well as novel design principles.

Problem	Conventional design solutions with pros/cons	Alternative design solutions, with pros/cons
Long-term plastic deformation of noncrystalline structural materials (creep)	• Using creep-resistant alloys, but it's limiting of operational conditions such as power, temperature	• Monocrystalline silicon as a mechanical material • Superior mechanical performance • High-resistivity silicon very suitable for microwave RF MEMS dielectric layers • Advanced processing techniques available • Expensive fabrication if SOI wafers are used
Power handling (heat transfer to substrate heat sink)	• Optimized heat-sink design of metallic bridges • Power limitations of thin metal bridges cannot be overcome	• Designs avoiding metallic bridges using high-resistivity monocrystalline silicon • The substrate as superior heat-sink. Potential substrate charging issues
Dielectric charging	• Complex actuation voltage shapes • Complex driving circuit • Low-voltage designs Stiction, higher risk of self-actuation • Special dielectric materials	• Dielectric-less actuators using stoppers for isolation • Eliminates charging • Lowers the maximum capacitance
Contact stiction for soft materials	• Increased passive restoring force • Requires high actuation voltage • Hard contact materials • Huge-contact force needed • High-contact reliability Low-contact performance degradation	• Active opening force, push-pull actuators, reversing active/passive functions in MEMS switch actuators • Improved recovery from stiction • Does not improve contact degradation for soft materials
Self-actuation and signal linearity for the large tuning range	• Limiting RF power and limitations in geometrical designs	• High-stiffness actuators • Unimproved tuning range • Multi-step actuators with high stiffness • Quasi-analog large tuning range • Highest stiffness at most nonlinear operating points • High reproducibility of multiple discrete tuning positions
Residual stress control for multilayer freestanding structures	• Process optimization or additional stress compensating layers • Temperature compensation is difficult • Sensitive to process parameter variation	• Symmetrical antiparallel metallization • Perfect balancing of stress gradient due to depositing layers of same thickness from opposing directions • Fully temperature compensated • Requires transfer bonding for perfect symmetry of deposition
Temperature compensation for multilayered free-standing structures	• Single-material multilayer sandwich structures • The extreme ratio of material thicknesses, e.g. thin reflection coatings • Does not allow for thick metallization for RF MEMS	• Symmetrical antiparallel metallization • Perfect balancing of stress gradient due to depositing layers of same thickness from opposing directions • Fully temperature compensated

this inability with the thin-film bundle may be discovered to get outgassing with the inner majority of appearance coating throughout the last (outermost) thin-film nitride plugging action. Plasma-enhanced chemical vapor deposition (PECVD) silicon nitride can be a proper substance regarding thin-film appearance due to its great plugging house. Nevertheless, outgassing especially in hydrogen, via increased temp is a concern to the stability through the PECVD silicon nitride thin-film packages as well as the unique IC appearance. More actions are required through the thin-film appearance substance.

Discussion

As explained above, there are different techniques which can be used, where these are summarized in Table 2 for the various packaging parameter challenges [21].

1) *Design problems in radiofrequency (RF) MEMS*

Radiofrequency (RF) MEMS tends to be MEMS gadgets which might be interacting using electric signals up to submillimeter surf, simply by moving over, modulating, tuning and selection. Common gadgets tend to be micromachined switches, mechanically tunable capacitors micromachined inductors, micromechanical resonators, filtration system, starting and tunable crammed traces intended for cycle shifters, impedance related circuits, reconfigurable antennas and three-dimensional (3D) micromachined [22]. Typical RF MEMS designs continue to present many essential complications. Slim steel links, for example, obtained in a lot of RF MEMS gadgets, like phase shifters are usually susceptible to temperature-accelerated slip and low energy, restricting the product lifetime. Important and essential design complications regarding the RF MEMS gadgets and the new design ideas handling the difficulties are demonstrated in Table 3 [23–25].

Conclusion

Reliability requirements are tough, and much fulfills requirements include heat cycling, rainy temperature, distress, and vibrations, plus a fifteen-year lifetime. The hermetic product packaging is extremely desirable because of its wetness, as well as increased voltages may cause electrode erosion, lower AR (anti-reflection) or Time (high reflection) coatings, which ultimately caused the extra insertion damage. Given that epoxy or additional normal thin films are permeable to wetness, where these are not often hermetic.

On the numbers of difficulties, many of the techniques such as mechanized tensions could be improved after the packaging procedure, which may lead to temporary centered misalignment. An analysis is essential while some software programs can be better and encountered. These kinds of tending to be conditions regarded with suitable mechanized, electrical, optical and along with Arctic packaging associated with MEMS technology.

Last but not least, the key, and infrequently the most significant trouble off is usually price. Appearance is a nominal 75% in the full merchandise price for optic parts, and that is normally definitely not unpredicted provided every one of the requirements outlined over. The important reason behind this substantial price is usually seen due to the employing place (with laser gentle through to keep an eye on connection lowering the aligning). By substantial considering that areas may move soon after the epoxy remedy.

References

[1] Ghaffarian R. Chip scale packaging guidelines distributed by ITRI. Interconnection Technology Research Institute; 2000. p. 40.
[2] Sarvar F, Hutt DA, Whalley DC. Application of adhesives in MEMS and MOEMS assembly: a review. POLYTRONIC 2002. 2nd International IEEE conference on polymers and adhesives in microelectronics and photonics, 2002. 22: IEEE; 2002.
[3] Mulloni V, Lorenzelli L, Margesin B, Barbato M, Meneghesso G. Temperature as an accelerating factor for lifetime estimation of RF-MEMS switches. Microelectron Eng 2016;160:63–7.
[4] Han L. A reconfigurable microwave equalizer with different maximum attenuations based on RF MEMS switches sensors journal. IEEE 2016;16:17–8.
[5] Weerasekera R, Zheng L-R, Pamunuwa D, Tenhunen H. Extending systems-on-chip to the third dimension: performance, cost and technological tradeoffs. ICCAD 2007. IEEE/ACM international conference on computer-aided design, 2007. IEEE; 2007. p. 212–9.
[6] Eaton WP, Smith JH. Micromachined pressure sensors: review and recent developments. Smart Mater Struct 1997;6:530.
[7] Dunn BD. Materials and processes. Springer; 2016. p. 461–500.
[8] Wang B. Considerations for mems packaging. HDP'04. Proceeding of the Sixth IEEE CPMT conference on high density microsystem design and packaging and component failure analysis, 2004. IEEE; 2004. p. 160–3.
[9] Ghaffarian R. Comparison of IC and MEMS packaging reliability approaches; 2000.
[10] Hsieh C, Ting J-M, Yang C, Chung C. The introduction of MEMS packaging technology. Proceedings of the 4th international symposium on electronic materials and packaging, 2002. IEEE; 2002. p. 300–6.
[11] Walser S, Siegel C, Winter M, Feiertag G, Loibl M, Leidl A. MEMS microphones with narrow sensitivity distribution. Sens Actuators, A 2016.
[12] Lee S-H, Cho J, Lee S, Zaman M, Ayazi F, Najafi K. A low-power oven-controlled vacuum package technology for high-performance MEMS. MEMS 2009. IEEE 22nd international conference on micro electro mechanical systems, 2009. IEEE; 2009. p. 753–6.
[13] Sterner M, Somjit N, Shah U, Dudorov S, Chicherin D, Räisänen A, Oberhammer J. Microwave MEMS devices designed for process robustness and operational reliability. Int J Microwave Wireless Technol 2011;3:547–63.
[14] Najafi K. Micropackaging technologies for integrated microsystems: applications to MEMS and MOEMS, Micromachining and Microfabrication Process Technology VIII. International Society for Optics and Photonics; 2003. p. 1–20.
[15] Hartzell AL, Da Silva MG, Shea H. MEMS reliability. Springer Science & Business, Media; 2010.
[16] Wibbeler J, Pfeifer G, Hietschold M. Parasitic charging of dielectric surfaces in capacitive microelectromechanical systems (MEMS). Sens Actuators, A 1998;71:74–80.
[17] Leester-Schädel M, Lorenz T, Jürgens F, Richter C. Microsystems for pharmatechnology. Springer; 2016. p. 23–57.
[18] Sosin S, Tian J, Bartek M. Hybrid wafer level packaging based on a capping substrate with cavities. In: Proceedings of eurosensors XX. Goteborg, Sweden; 2006. p. 17–20.
[19] Tian J, Sosin S, Iannacci J, Gaddi R, Bartek M. RF–MEMS wafer-level packaging using through-wafer interconnect. Sens Actuators, A 2008;142:442–51.
[20] Li Q, Goosen J, Van Beek J, Van Keulen F, Phan K, Zhang G. Failure analysis of a thin-film nitride MEMS package. Microelectron Reliab 2008;48:1557–61.
[21] Tao Y, Malshe AP, Brown WD. Selective bonding and encapsulation for wafer-level vacuum packaging of MEMS and related micro systems. Microelectron Reliab 2004;44:251–8.
[22] Saba N, Soin N, Khamil KN. Simulation and analysis of actuation voltage of electrostatically actuated RF MEMS cantilever switch. 2015 International conference on smart sensors and application (ICSSA). IEEE; 2015. p. 106–10.
[23] Goldsmith C, Ehmke J, Malczewski A, Pillans B, Eshelman S, Yao Z, et al. Lifetime characterization of capacitive RF MEMS switches. Microwave symposium digest, 2001 IEEE MTT-S international. IEEE; 2001. p. 227–30.
[24] Blasquez G, Favaro P. Silicon Pyrex electrostatic bonding: applicability to industrial microdevices production. In: Proceedings of the 11th international conference on solid state sensors and actuators, Munich; 2001. p. 10–4.
[25] Harpster TJ, Najafi K. Long-term testing of hermetic anodically bonded glass-silicon packages. The Fifteenth IEEE International Conference on Micro Electro Mechanical Systems, 2002. IEEE; 2002. p. 423–6.

Journal of Theoretical and Applied Physics (2018) 12:293–298
https://doi.org/10.1007/s40094-018-0308-x

RESEARCH

Temperature sensor utilizing a ternary photonic crystal with a polymer layer sandwiched between Si and SiO_2 layers

Dena M. El-Amassi[1] · Sofyan A. Taya[1] · Dhasarathan Vigneswaran[2]

Received: 22 May 2018 / Accepted: 2 November 2018 / Published online: 14 November 2018

Abstract
Recently, one-dimensional periodic ternary photonic crystals have shown outstanding properties when compared to one-dimensional periodic binary photonic crystals. In this work, a ternary photonic crystal is proposed as a temperature sensor. The structure of the ternary photonic structure is considered Si/polymer/SiO_2. The transmission spectra of the proposed ternary photonic structure are studied for different temperatures. It is observed that as the temperature increases, the transmission peak shifts toward higher wavelengths due to thermo-optic and thermal expansion coefficients of the polymer. It is found that the temperature-sensitive transmission peak shift is considerably enhanced due to the insertion of the polymer layer between Si and SiO_2 to constitute a ternary photonic crystal.

Keywords Ternary photonic crystal · Temperature sensor · Polymers

Introduction

The concept of photonic crystals and propagation of electromagnetic waves (EMW) through these structures were introduced since 1987 [1, 2]. One-dimensional photonic crystal has received an increasing interest by many researchers due to the possible use in a considerable set of applications. The most fascinating feature in photonic crystals is the appearance of photonic band gaps in which the transmission of EMW of certain wavelength is not allowed. These structures are constructed by using two or more media repeated alternatively. The width of the band gap varies with the variation of refractive indices of materials, temperature, and the incident angle [3, 4]. If these parameters are maintained fixed, then this photonic structure will have fixed predetermined bands of wavelength or frequencies. Any change in refractive index, temperature, or angle of incidence will change the photonic band gap. This is the rule of operation of a photonic crystal when acting as an optical sensor for detection variations in the index of refraction [5–11] and temperature [12, 13].

Photonic crystals can be grouped into a set of types according to the number of layers into one period. When there are two layers in a period, it is called binary, and it is known as ternary when there are three layers in a period and so on. In a recent years, photonic crystals have received an increasing attention due to exclusive performance in a set of applications such as omnidirectional reflectors [14], filters [15], and highly sensitive optical sensors [16].

In a recent work, the band gap in a photonic crystal consisting of dielectric/metal/dielectric was shown to be enlarged due to the metal layer [17]. The variation of the band gap width in a periodic photonic crystal with a negative-index material was investigated [18]. An omnidirectional photonic band gap in a photonic crystal having the structure dielectric/plasma layer/dielectric was investigated using the transfer matrix method [19]. The design of 2D photonic crystal-coupled resonating optical waveguide-based integrated optic sensor platform was proposed and investigated [20]. A binary photonic crystal consisting of metal–dielectric layers was analyzed [21]. It was shown that the metal–dielectric photonic crystal can be treated as an effective metallic medium with a well-defined effective plasma frequency [21]. Enhancement of omnidirectional total reflection in a ternary photonic crystal was theoretically proposed [22–24].

✉ Sofyan A. Taya
staya@iugaza.edu.ps

[1] Physics Department, Islamic University of Gaza, Gaza, Palestine

[2] Department of Electronics and Communication Engineering, Sri Krishna College of Technology, Coimbatore 641 042, India

The rule of operation of a photonic crystal when acting as a temperature sensor is as follows. When the surrounding temperature alters, the index of refraction of substances constituting the crystal will be altered as a result of thermo-optical effect. Moreover, the thickness of the layers in the photonic crystal will be also altered due to the thermal expansion effect. In this case, the transmission profile will be modified. By inspection the transmission spectrum changes or shifts, and a small variation in temperature can be detected. In this way, photonic crystals can be employed as efficient temperature sensors.

In this paper, a ternary photonic crystal with the structure Si/polymer/SiO_2 is studied as a temperature sensor. The characteristic matrix of a signal cell consisting of three layers is expressed in terms of the refractive indices, thicknesses, wavelength, and angles of refraction inside the media. The variation in refractive index and thickness of the layers due to the variation in temperature is considered. The transfer matrix of the whole system consisting of N–cells is derived, and the transmission coefficient is also deduced. The transmission profile is investigated at different temperatures.

Theory of scattering from a photonic crystal

One-dimensional ternary photonic crystal is assumed. It consists of three layers of indices n_1, n_2, and n_3. The layers are assumed to have the thicknesses d_1, d_2, and d_3. If we assume one period consisting of three layers, then the thickness of the period will be $d = d_1 + d_2 + d_3$.

Thickness of a substance (d) can be altered as a result of thermal expansion effect according to

$$\Delta d = \alpha d(\Delta T) \tag{1}$$

where α is the thermal expansion coefficient of the substance and ΔT is the change in temperature.

Refractive index a substance (n) can be also altered as a result of thermo-optical effect according to

$$\Delta n = \gamma n(\Delta T) \tag{2}$$

where γ is the coefficient of thermo-optic of a substance.

Consider an EMW is incident from air on the proposed photonic crystal. The incident angle is assumed θ_0. The transmission of the wave can be calculated by making use of the transfer matrix method. The transfer matrix of a single layer is given by:

$$h_i = \begin{bmatrix} \cos\beta_i & \frac{-i\sin\beta_i}{p_i} \\ -ip_i\sin\beta_i & \cos\beta_i \end{bmatrix}. \tag{3}$$

The characteristic matrix $L[d]$ of a signal period is expressed as:

$$L[d] = \prod_{i=1}^{s} \begin{bmatrix} \cos\beta_i & \frac{-i\sin\beta_i}{p_i} \\ -ip_i\sin\beta_i & \cos\beta_i \end{bmatrix} = \begin{bmatrix} L_{11} & L_{12} \\ L_{21} & L_{22} \end{bmatrix}, \tag{4}$$

where $s = 3$ and $i = 1$, 2, and 3 denote the layers of refractive indices n_1, n_2, and n_3, respectively, and β_i and p_i are given as

$$\beta_1 = \frac{2\pi(n_1 + \Delta n_1)(d_1 + \Delta d_1)\cos\theta_1}{\lambda_0}, \tag{5}$$

$$\beta_2 = \frac{2\pi(n_2 + \Delta n_2)(d_2 + \Delta d_2)\cos\theta_2}{\lambda_0}, \tag{6}$$

$$\beta_3 = \frac{2\pi(n_3 + \Delta n_3)(d_3 + \Delta d_3)\cos\theta_3}{\lambda_0}, \tag{7}$$

$$p_1 = (n_1 + \Delta n_1)\cos\theta_1, \tag{8}$$

$$p_2 = (n_2 + \Delta n_2)\cos\theta_2, \tag{9}$$

$$p_3 = (n_3 + \Delta n_3)\cos\theta_3, \tag{10}$$

with λ_0 is the wavelength in vacuum. Angles θ_1, θ_2, and θ_3 are the angles of refraction in the three layers of the cell. In terms of θ_0, they are given by:

$$\cos\theta_1 = \left[1 - \frac{n_0^2\sin^2\theta_0}{(n_1 + \Delta n_1)^2}\right]^{\frac{1}{2}}, \tag{11}$$

$$\cos\theta_2 = \left[1 - \frac{n_0^2\sin^2\theta_0}{(n_2 + \Delta n_2)^2}\right]^{\frac{1}{2}}, \tag{12}$$

$$\cos\theta_3 = \left[1 - \frac{n_0^2\sin^2\theta_0}{(n_3 + \Delta n_3)^2}\right]^{\frac{1}{2}}. \tag{13}$$

The determinant of the matrix $L[d]$ is equal to unity.

For a system consisting of N periods, the characteristic matrix is given by:

$$\begin{aligned}[L(d)]^N &= \begin{bmatrix} L_{11}T_{N-1}(a) - T_{N-2}(a) & L_{12}T_{N-1}(a) \\ L_{21}T_{N-1}(a) & L_{22}T_{N-1}(a) - T_{N-2}(a) \end{bmatrix} \\ &= \begin{bmatrix} s_{11} & s_{12} \\ s_{21} & s_{22} \end{bmatrix}\end{aligned} \tag{14}$$

where

$$s_{11} = \left(\sigma_1 - \frac{p_2}{p_1}\sigma_2 - \frac{p_3}{p_2}\sigma_3 - \frac{p_3}{p_1}\sigma_4\right), \tag{15}$$

$$s_{12} = -i\left(\frac{\rho_1}{p_1} + \frac{\rho_2}{p_2} + \frac{\rho_3}{p_3} - \frac{p_2\rho_4}{p_1 p_2}\right), \tag{16}$$

$$s_{21} = -i\left(p_1\rho_1 + p_2\rho_2 + p_3\rho_3 - \frac{p_1 p_3}{p_2}\rho_4\right), \tag{17}$$

$$s_{22} = \left(\sigma_1 - \frac{p_1}{p_2}\sigma_2 - \frac{p_2}{p_3}\sigma_3 - \frac{p_1}{p_3}\sigma_4\right). \tag{18}$$

where $\sigma_1 = \cos\beta_1 \cos\beta_2 \cos\beta_3$, $\sigma_2 = \sin\beta_1 \sin\beta_2 \cos\beta_3$, $\sigma_3 = \cos\beta_1 \sin\beta_2 \sin\beta_3$, $\sigma_4 = \sin\beta_1 \cos\beta_2 \sin\beta_3$, $\rho_1 = \sin\beta_1 \cos\beta_2 \cos\beta_3$, $\rho_2 = \cos\beta_1 \sin\beta_2 \cos\beta_3$, $\rho_3 = \cos\beta_1 \cos\beta_2 \sin\beta_3$ and $\rho_4 = \sin\beta_1 \sin\beta_2 \sin\beta_3$.

T_N are Chebyshev polynomials of the second kind given by:

$$T_N(a) = \frac{\sin\left[(N+1)\cos^{-1} a\right]}{\left[1 - a^2\right]^{\frac{1}{2}}}, \tag{19}$$

and a is given by

$$a = \frac{1}{2}\left[s_{11} + s_{22}\right]. \tag{20}$$

In terms of the elements s_{ij}, the transmission coefficient of a system consisting of N periods is given by:

$$t = \frac{2p_0}{\left(s_{11} + s_{12}p_0\right)p_0 + \left(s_{21} + s_{22}p_0\right)}, \tag{21}$$

where

$$p_0 = n_0 \lambda \text{Ƶ} \cos\theta_0 = \cos\theta_0 \quad (\text{as } n_0 = 1) \tag{22}$$

The transmissivity of the system can be written as:

$$T = |t|^2. \tag{23}$$

Results and discussion

Ternary photonic crystal is considered of the structure Si/polymer/SiO_2. In Fig. 1, we consider the polymer to be polycarbonate. The parameters of the structure are taken as [13] $n_1 = 3.3$ (Si), $n_3 = 1.46$ (SiO_2), $d_1 = 117$ nm, and $d_3 = 265$ nm. The number of the period is considered $N = 10$. The coefficient of thermo-optic (γ) of a material represents the change in the index of refraction per degree rise in temperature, whereas the coefficient of thermal expansion (α) of a material represents the change in the dimensions of a material per degree rise in temperature. In the following calculations, we take $\gamma = 1.86 \times 10^{-4}$ °C^{-1} (Si), $\gamma = 6.8 \times 10^{-6}$ °C^{-1} (SiO_2), $\alpha = 0.5 \times 10^{-6}$ °C^{-1} (Si) and $\alpha = 2.6 \times 10^{-6}$ °C^{-1} (SiO_2). The parameters of polycarbonate are taken as $n_2 = 1.5848$ and $d_2 = 10$ nm. In a recent study conducted by Zhang et al. [23] on polymers to determine their thermal coefficients for optical waveguide applications, they found that $\gamma = 0.9 \times 10^{-4}$ °C^{-1} and $\alpha = 1.7 \times 10^{-6}$ °C^{-1} for polycarbonate. The angle of incidence is considered to be $\theta_0 = 0$ (normal incidence). In Fig. 1, the transmission spectra of one-dimensional ternary photonic crystal structure are

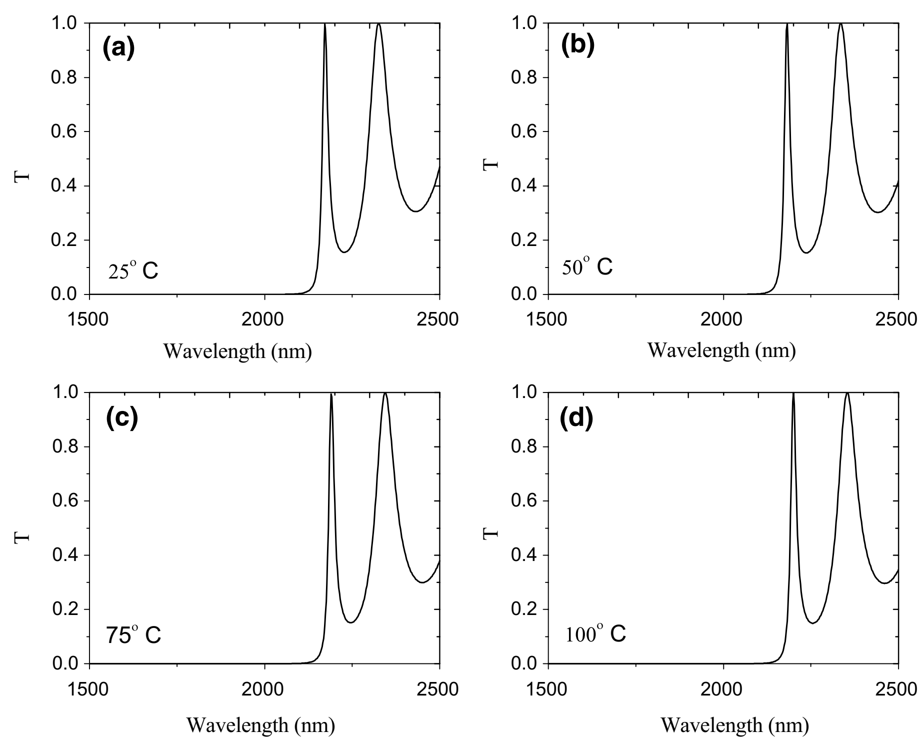

Fig. 1 Transmission spectra of one-dimensional ternary photonic crystal structure with $n_1 = 3.3$ (Si), $n_2 = 1.5848$ (polycarbonate), $n_3 = 1.46$ (SiO_2), $d_1 = 117$ nm, $d_2 = 10$ nm and $d_3 = 265$ nm, $N = 10$ at temperatures of 25 °C, 50 °C, 75 °C, and 100 °C

shown for temperatures of 25 °C, 50 °C, 75 °C, and 100 °C. Inspecting the first transmission peak at different temperatures, we find that the wavelengths corresponding to the first peak are $\lambda_1 = 2172$ nm (25 °C), $\lambda_1 = 2181.2$ nm (50 °C), $\lambda_1 = 2190.4$ nm (75 °C), and $\lambda_1 = 2199.6$ nm (100 °C). This means that for a temperature rise of 75 °C, we have a transmission peak shift of 27.6 nm. Then we have a transmission peak shift of 0.368 nm degree rise in temperature. It is worth mentioning that the shift occurs toward higher wavelengths. Moreover, the shift versus temperature of the first peak is shown in Fig. 2 for the photonic crystal containing polycarbonate. It is clear that $\Delta\lambda/\Delta T = 0.368$.

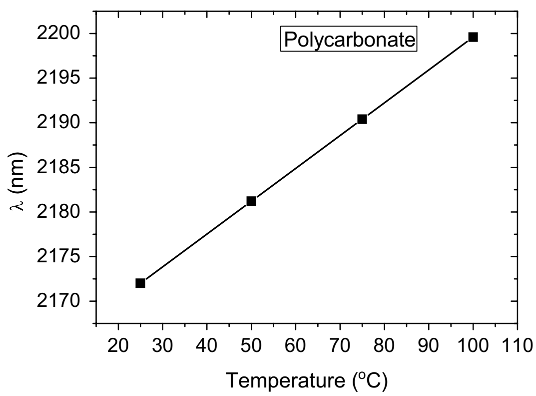

Fig. 2 Shift versus temperature of the first peak for polycarbonate

In Fig. 3, the same parameters as in Fig. 1 are adopted. The only difference between them is the polymer. We consider in Fig. 3 the polymer to be polystyrene of index of refraction $n_2 = 1.5916$. From Ref. [25], they found $\gamma = 1.2 \times 10^{-4}$ °C^{-1} and $\alpha = 2.2 \times 10^{-6}$ °C^{-1} for polystyrene. The transmission spectra of the proposed ternary photonic crystal with polystyrene layer are shown in Fig. 2 for the same values of temperature. As can be seen from the figure, the first transmission peak are found to occur at $\lambda_1 = 2172$ nm (25 °C), $\lambda_1 = 2181.5$ nm (50 °C), $\lambda_1 = 2191$ nm (75 °C) and $\lambda_1 = 2200.5$ nm (100 °C). For a temperature rise of 75 °C, there is a transmission peak shift of 28.5 nm. A transmission peak shift of 0.380 nm per degree rise in temperature. There is a preference of using polystyrene over polycarbonate because of the higher transmission peak shift.

We also show the shift versus temperature of the first peak in Fig. 4 for the photonic crystal containing polystyrene. It is clear that $\Delta\lambda/\Delta T = 0.380$.

It is worth mentioning that glass transition points of polycarbonate and polystyrene are 147 °C and 100 °C, respectively. Melting points of the two polymers are 225 °C for polycarbonate and 240 °C for polystyrene. So the proposed sensor cannot be used for temperatures higher than 100 °C especially that consisting of Si/polystyrene/SiO_2. If it is used for sensing high temperatures, shrinking of the layers may occur.

In a recent study [12], A. Banerjee compared binary and ternary photonic crystals as temperature sensors. He found that a temperature peak shift of 0.350 nm can be obtained

Fig. 3 Transmission spectra of one-dimensional ternary photonic crystal structure with $n_1 = 3.3$ (Si), $n_2 = 1.5916$ (Polystyrene), $n_3 = 1.46$ (SiO_2), $d_1 = 117$ nm, $d_2 = 10$ nm and $d_3 = 265$ nm, $N = 10$ at temperatures of 25 °C, 50 °C, 75 °C and 100 °C

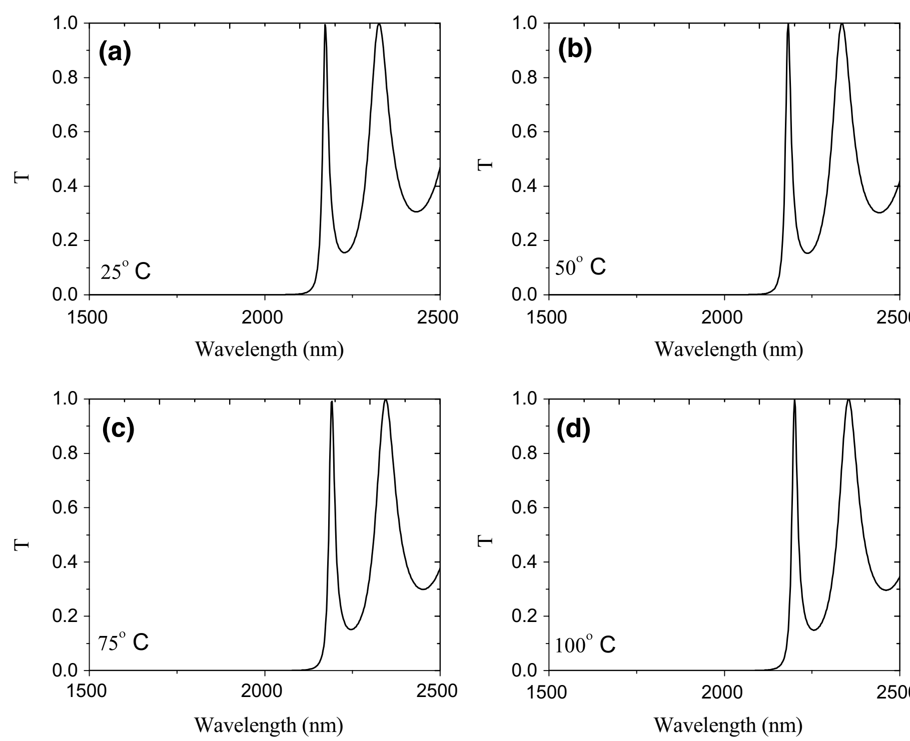

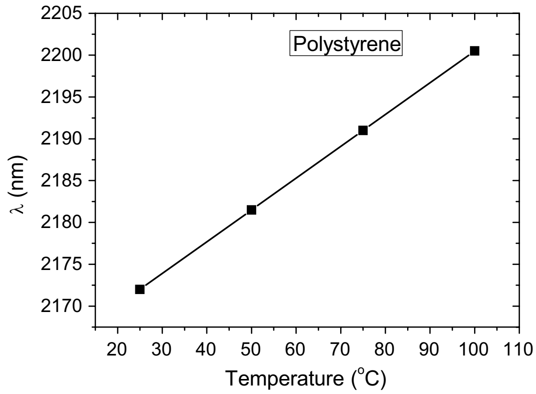

Fig. 4 Shift versus temperature of the first peak for polystyrene

with the binary structure, whereas a peak shift of 0.355 can be attained with the ternary one. In his structure, he used $Bi_4Ge_3O_{12}$ to form a ternary photonic crystal.

In this work, a much higher peak shift is obtained with the use of polymers (polycarbonate and polystyrene) instead of $Bi_4Ge_3O_{12}$.

Conclusion

Recently, binary and ternary photonic crystals were proposed in temperature sensing. The author of Ref. [12] found that with a binary photonic crystal, a temperature peak shift of 0.350 nm may be obtained, whereas with a ternary photonic crystal, a peak shift of 0.355 may be obtained. His ternary photonic crystal has a working layer of $Bi_4Ge_3O_{12}$. No doubt that this was a fascinating result. In this work, a much higher peak shift was obtained using a polymer as a working layer. The proposed ternary photonic crystal was assumed to have the structure Si/polymer/SiO_2. Transmission profile of this photonic structure was investigated at different temperatures. It was found that with the increase in temperature, the transmission peak shifts toward higher wavelengths. This can be attributed to thermo-optic and thermal expansion coefficients. When the polymer “polycarbonate” was used, a transmission peak shift of 0.368 nm per degree rise in temperature was obtained, whereas when the polymer (Polystyrene) was employed, a transmission peak shift of 0.380 nm per degree rise in temperature.

It is concluded that the temperature-sensitive transmission peak shift is considerably enhanced due to the insertion of the polymer layer between Si and SiO_2 to constitute a ternary photonic crystal.

Finally, it is worth mentioning that a ternary photonic crystal of Si/polymer/SiO_2 would involve a complicated sputtering/spin coating/sputtering procedure for N periods. In future work, we may try to find alternative transparent inorganic materials of appropriate properties.

References

1. Yablonovitch, E.: Inhibited spontaneous emission in solid state physics and electronics. Phys. Rev. Lett. **58**, 2059–2062 (1987)
2. John, S.: Strong localization of photons in certain disordered dielectric superlattices. Phys. Rev. Lett. **58**, 2486–2489 (1987)
3. Kumar, V., Suthar, B., Kumar, A., Singh, KhS, Bhargava, A.: The effect of temperature and angle of incidence on photonic band gap in a dispersive Si-based one dimensional photonic crystal. Phys. B—Condens. Matter **416**, 106–109 (2013)
4. Suthar, B., Kumar, V., Kumar, A., Singh, KhS, Bhargava, A.: Thermal expansion of photonic bandgap for 1-D photonic crystals. Prog. Electromagn. Res. Lett. **32**, 81–90 (2012)
5. Shaheen, S.A., Taya, S.A.: Propagation of p-polarized light in photonic crystal for sensor application. Chin. J. Phys. **55**, 571–582 (2017)
6. Taya, S.A., Shaheen, S.A., Alkanoo, A.A.: Photonic crystal as a refractometric sensor operated in reflection mode. Superlattices Microstruct. **101**, 299–305 (2017)
7. Alkanoo, A.A., Taya, S.A.: Theoretical investigation of five-layer waveguide structure including two left-handed material layers for refractometric applications. J. Magn. Magn. Mater **449**, 395–400 (2018)
8. Taya, S.A., Mahdi, S.S., Alkanoo, A.A., Qadoura, I.M.: Slab waveguide with conducting interfaces as an efficient optical sensor: TE case. J. Mod. Opt. **64**, 836–843 (2017)
9. Taya, S.A.: Theoretical investigation of slab waveguide sensor using anisotropic metamaterials. Opt. Appl. **45**, 405–417 (2015)
10. Taya, S.A.: P-polarized surface waves in a slab waveguide with left-handed material for sensing applications. J. Magn. Magn. Mater **377**, 281–285 (2015)
11. Taya, S.A.: Slab waveguide with air core layer and anisotropic left-handed material claddings as a sensor. Opto-Electron Rev. **22**, 252–257 (2014)
12. Banerjee, A.: Enhanced temperature sensing by using one-dimensional ternary photonic band gap structures. Prog. Electromagn. Res. Lett. **11**, 129–137 (2009)
13. Kai, T., Wei, C.W., Hui, Y.G., Quan, L.Z.: Study on temperature property of band structures in one-dimensional photonic crystals. Optoelectron. Lett. **3**, 0444–0447 (2007)
14. Awasthi, S.K., Malaviya, U., Ojha, S.P.: Enhancement of omnidirectional total-reflection wavelength range by using onedimensional ternary photonic bandgap material. J. Opt. Soc. Am. B **23**, 2566–2571 (2006)
15. Awasthi, S.K., Ojha, S.P.: Design of a tunable optical filter by using one-dimensional ternary photonic band gap material. Prog. Electromagn. Res. M **4**, 117–132 (2008)
16. Banerjee, A.: Enhanced refractometric optical sensing by using one-dimensional ternary photonic crystals. Prog. Electromagn. Res. PIER **89**, 11–22 (2009)

17. Wu, C.J., Chung, Y.H., Syu, B.J.: Band gap extension in a one-dimensional ternary metal-dielectric photonic crystal. Prog. Electromagn. Res. PIER **102**, 81–93 (2010)
18. Zare, L.Z., Gharaati, A.: Investigation of band gap width in ternary 1D photonic crystal with left-handed. Acta Phys. Pol. A **125**, 36–38 (2014)
19. Xue, F., Liu, S.B., Zhang, H.F., Kong, X.K., Wen, Y.D., Wang, L.L., Qian, S.: The theoretical analysis of omnidirectional photonic band gaps in the one-dimensional ternary plasma photonic crystals based on Pell quasi-periodic structure. Opt. Quant. Electron **49**, 19 (2017)
20. Goyal, A.K., Dutta, H.S., Pal, S.: Performance optimization of photonic crystal resonator based sensor. Opt. Quant. Electron. **48**, 431 (2016)
21. Xu, X., Xi, Y., Han, D., Liu, X., Zi, J., Zhu, Z.: Effective plasma frequency in one-dimensional metallic-dielectric photonic crystals. Appl. Phys. Lett. **86**, 091112 (2005)
22. Awasthi, S.K., Malaviya, U., Ojha, S.P.: Enhancement of omnidirectional total-reflection wavelength range by using one-dimensional ternary photonic bandgap material. JOSA B **23**, 2566–2571 (2006)
23. Dai, X., Xiang, Y., Wen, S.: Broad omnidirectional reflector in the one-dimensional ternary photonic crystals containing superconductor. Prog. Electromagn. Res. **120**, 17–34 (2011)
24. Bellingeri, M., Chiasera, A., Kriegel, I., Scotognella, F.: Optical properties of periodic, quasi-periodic, and disordered one-dimensional photonic structures. Opt. Mater **72**, 403–421 (2017)
25. Zhang, Z., Zhao, P., Lin, P., Sun, F.: Thermo-optic coefficients of polymers for optical waveguide applications. Polymer **47**, 4893–4896 (2006)

Publisher's Note Springer Nature remains neutral with regard to jurisdictional claims in published maps and institutional affiliations.

Quasi-Photonic Crystal Fiber-Based Spectroscopic Chemical Sensor in the Terahertz Spectrum: Design and Analysis

Bikash Kumar Paul, Kawsar Ahmed, Dhasarathan Vigneswaran, Fahad Ahmed, Subrata Roy, and Derek Abbott, *Fellow, IEEE*

***Abstract*— In this paper, a novel microstructure quasi-photonic crystal fiber design is proposed. Aimed at a high relative sensitivity, it is targeted for chemical sensing applications in the terahertz regime. A rigorous full-vector finite element method-based numerical investigation has been applied by employing an anisotropic perfectly matched layer for optimizing key parameters. Improved relative sensitivity responses of 78.8%, 77.8%, and 69.7% are achieved for targeted analytes ethanol, benzene, and water, respectively, at the operating frequency of $f = 1.3$ THz. Moreover, confinement loss, effective area, power fraction, and numerical aperture are analyzed from 0.8 to 2.0 THz.**

***Index Terms*— Liquid sensor, quasi photonic crystal fiber, terahertz.**

I. Introduction

TERAHERTZ waves or T-rays, typically are considered to lie in the 0.1–10 THz range. With the advancement of the technological change terahertz is reported to have several areas of applications, such as in image processing [1], astrophysics [2], security surveillance [3], medicine [4], sensing [5] and many more. To achieve the high level performance for those applications, the good directional quality of beams are required [6], [7]. Among these areas, terahertz based PCF sensors have gained much attention. Now terahertz based sensing devices are seen in medical or clinical diagnostic systems. Moreover, RNA, DNA [8]–[11], breast cancer [12], skin cancer [13] detection are some major applications in medical diagnostics. Moreover, PCF based waveguides are considered for faster communication or high bit rate data transmission. Many methods for guiding terahertz radiation have been developed such as, parallel plate [14] and bare metal wire [15] waveguides. However there is a demand for increased detection sensitivity and due to the structural diversity, photonic band-gap structures [16], low index discontinuity waveguides [17], and photonic crystal fibers (PCF) [18] have potential in this regard. Some optical materials such as Teflon [19], high density polyethylene (HDPE) [20] and TOPAS [21] have been found useful in the terahertz regime. Using these materials, terahertz PCFs consist of periodic arrangements of air holes in the center defected region. Besides, PCF offers high birefringence [22], single mode propagation [23] and design parameters that can be optimized to mitigate dispersion [24]. Due to these advantageous properties, PCF is attractive for various practical applications.

Very recently, a number of forms of temperature sensor [25], pressure sensor [26], salinity sensor [27], biosensor and chemical sensor [28]–[30] have been proposed. In 2006, Hoo *et al.* [31] presented a PCF based novel gas sensor. Then a PCF based gas detector utilizing evanescent waves [32], [33] was proposed. So far, improved fractional power of more than 30% for methane sensing has been achieved [31] and gas sensing with relative sensitivity of 4.79% and confinement loss 32.4 dB/m are attained [34]. Besides, chemical sensing using hybrid core PCF with relative sensitivity of 49.17% and confinement loss of 2.75×10^{-10} dB/m [35], a hexagonal PCF with increasing diameter of first ring cladding with relative sensitivity of 59% and confinement loss of 10^{-11} dB/m [36] has been achieved. Recently, a folded cladded PCF for chemical sensing [37] was proposed with relative sensitivity of 64.19% and confinement loss of 2.07×10^{-5} dB/m.

II. Design Theory for the Proposed Model

Fig. 1 presents the schematic end faced view of the proposed microstructure Q-PCF. The proposed Q-PCF has been engineered with: (a) quasi shape cladding and (b) porous core with circular shaped air holes. A quasi periodic pattern has been successfully employed to form the cladding region with complete unique circular shape air cavities with the diameter

Manuscript received August 23, 2018; accepted September 18, 2018. Date of publication September 28, 2018; date of current version November 16, 2018. The associate editor coordinating the review of this paper and approving it for publication was Dr. Sillas Hadjiloucas. *(Corresponding author: Kawsar Ahmed.)*

B. K. Paul is with the Department of Software Engineering, Daffodil International University, Dhaka 1207, Bangladesh, and also with the Group of Bio-photomatix, Tangail 1902, Bangladesh (e-mail: bikash.k.paul@ieee.org).

K. Ahmed is with the Department of Information and Communication Technology, Mawlana Bhashani Science and Technology University, Tangail 1902, Bangladesh, and also with the Group of Bio-photomatix, Tangail 1902, Bangladesh (e-mail: kawsar.ict@mbstu.ac.bd).

D. Vigneswaran is with the Department of Electronics and Communication Engineering, Sri Krishna College of Technology, Coimbatore 641 042, India (e-mail: dhasa.viki@gmail.com).

F. Ahmed and S. Roy are with the Department of Information and Communication Technology, Mawlana Bhashani Science and Technology University, Tangail 1902, Bangladesh (e-mail: fahad.ahmed.ict13@gmail.com; subrataxon@gmail.com).

D. Abbott is with the School of Electrical and Electronic Engineering, The University of Adelaide, Adelaide, SA 5005, Australia (e-mail: derek.abbott@adelaide.edu.au).

Digital Object Identifier 10.1109/JSEN.2018.2872892

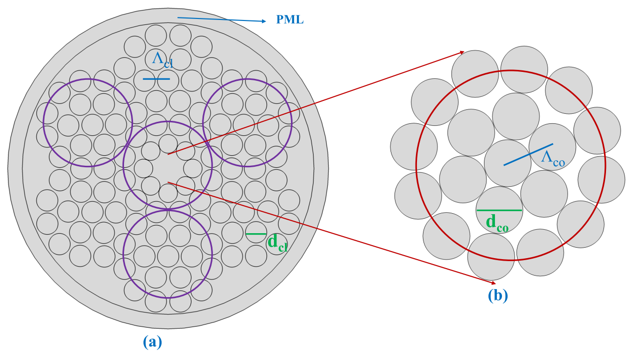

Fig. 1. The transverse cross sectional view of the proposed PCF (a) the cladding region (b) magnified view of the innermost core region.

of $d_{cl} = 303.95\ \mu$m. The exact distance from the center of one air cavity to another air cavity commonly known as the pitch (Λ) and it affects the air filling fraction (AFF). Note that an AFF of 0.94 is maintained in the cladding region, which offers flexibility in fabrication for the fiber. Moreover, the core has been constituted with circular shaped holes with $d_{co} = 85\ \mu$m and $\Lambda_{co} = 90\ \mu$m which also offers the same design flexibility. The outer boundary of the presented model has been surrounded by an A-PML with depth of the 10% of the total fiber radius. Note that TOPAS has been selected here as the base material for its optical excellence such as transparency at terahertz frequencies, high resistance to acids and alkalis, excellent bio compatibility etc. [38].

III. Synopsis of the Numerical Analysis

For electromagnetic numerical investigation several methods are available such as Gaussian beam mode analysis [6], [7], finite difference time domain (FTDT), FEM etc. But beam mode analysis is not so applicable for microstructured PCF sensor design. The full vector finite element method is the best for analyzing optoelectronic devices, furthermore it takes up less computation time. Besides this numerical method, mesh analysis is also playing a vital role. Note that FV-FEM is a very sophisticated method for analyzing electromagnetics. Because, it requires comparatively less computational time than other numerical approaches. In this paper, the full vector finite element method (FV-FEM) has been employed for finding the propagating modes of the optical fiber. The FV-FEM based commercial software package COMSOL Multiphysics version 4.2 is used to simulate the proposed structure.

The extent of interaction of light with the targeted analytes is a factor that determines sensitivity. To realize the sensing response of the proposed Q-PCF, we first calculate the relative sensitivity. Note that if a PCF acts as a sensor then the Beer-Lambert law is applicable and the relative sensitivity coefficient P can be found for a given sample. It can be evaluated by the following expression for relative sensitivity coefficient,

$$R = \frac{n_r}{n_{eff}} \times P \tag{1}$$

where, n_r and n_{eff} are the refractive index of the sample and effective refractive index the specific frequency of interest. Poynting's theorem is very convenient for determining the optical power inside the innermost core and the cladding region. It can be calculated by the following expression:

$$P = \frac{\int_{sample} R_e(E_x H_y - E_y H_x)dxdy}{\int_{total} R_e(E_x H_y - E_y H_x)dxdy} \times 100 \tag{2}$$

where, E_x, E_y represent transverse electric fields and H_x, H_y represent transverse magnetic fields of the fundamental guided mode. Mode power fraction is one of the essential factors that defines the amount of transmitted optical power propagated through the different region of the fiber. The mode power fraction [21] can be calculated using the following expression:

$$\text{Mode Power Fraction } (\eta') = \frac{\int_X S_z dA}{\int_{All} S_z dA} \tag{3}$$

here, the numerator of Equation (3) separately defines the area or region of interest and denominator uniquely defines the whole cross section region of the PCF.

One of the important forms of loss, commonly known as confinement loss, arises from the core as well as cladding porosity. Core and cladding porosity largely depend on the dielectric medium of the waveguide. Confinement loss or leakage loss lessens the optical power strength by spreading the optical power outside the core region. For each and every operating frequency for which optical signal propagates inside the core there must exist a propagation constant, β. The propagation constant comprises two parts, one is the real part that provides effective index mode and another is the imaginary part that defines confinement loss or leakage loss. The confinement loss [39] can be calculated by the following expression:

$$L_c[\text{cm}^{-1}] = \left(\frac{4\pi \text{f}}{\text{c}}\right)\text{Im}(\text{n}_{\text{eff}}) \tag{4}$$

here, f is the applied frequency and c is the velocity of light in free space respectively. The I_m is the imaginary part of the propagation constant. To determine the mode guidance of the PCF over the applied frequency spectrum, the V parameter must be evaluated. The mode guidance is separated into two regions: one is single mode and the other is multimode. The V parameter can be calculated by the following expression:

$$V = \frac{2\pi r f}{c}\sqrt{n_{core}^2 - n_{cladding}^2} \le 2.405 \tag{5}$$

where, n_{core} and $n_{cladding}$ are the effective refractive index of the core and the cladding region respectively. The f is the operating frequency and c is the velocity of light ($c = 3 \times 10^8$ ms^{-1}). It is important to know that the effective mode area is necessary for estimating the numerical aperture. The effective mode area (A_{eff}) of the propagating mode can be quantified by the following expression:

$$A_{eff} = \frac{\left[\int I(r)rdr\right]^2}{\left[\int I^2(r)dr\right]^2} \tag{6}$$

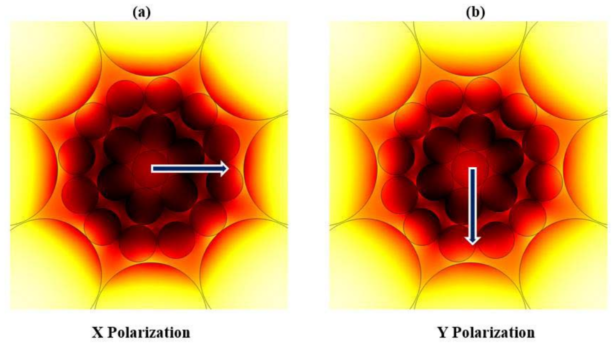

Fig. 2. Contour plot of field intensity of (a) HE_{11}^{x}; and (b) HE_{11}^{y} modes for optimized parameters at the operating frequency $f = 1$ THz.

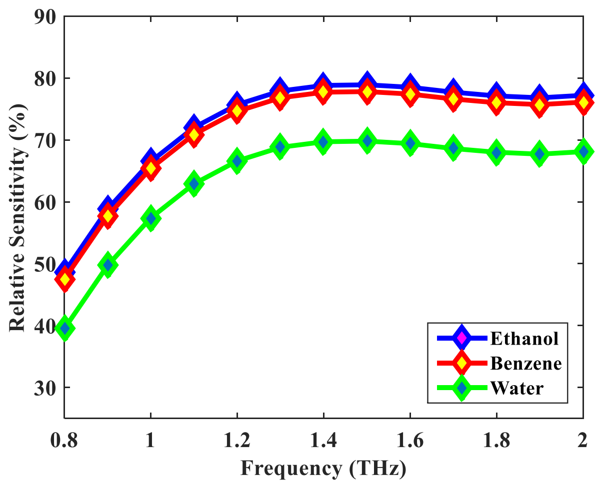

Fig. 3. Relative sensitivity as a function of frequency (f) for different targeted analytes over the wide frequency spectrum ranging from 0.80 THz to 2 THz.

here, $I(r) = |E_t|^2$ represents fiber cross sectional transverse electric field density distribution. Note that numerical aperture (NA) can be measured by the following expression:

$$\text{Numerical Aperture (NA)} = \frac{1}{\sqrt{1 + \frac{\pi A_{\text{eff}} f^2}{c^2}}} \tag{7}$$

where, A_{eff} is the effective area, f is the operating frequency and c is the velocity of light.

IV. Result and Discussion

We begin by considering the sensitivity to different targeted analytes such as water, benzene and ethanol. To conduct this study the derived numerical values for each analyte are inserted in Equation (2). The derived values are plotted using MATLAB version 2016b in Fig. 3. The proposed PCF has been investigated over a broad frequency range from 0.8 THz to 2.0 THz. From the figure it can be seen that for the frequency range 0.8 THz to 1.2 THz the sensitivity curves sharply rise after which they plateau.

Here for the lower analyets index water gives the minimum sensitivity response of 69.7% and higher index ethanol gives the maximum sensitivity response of 78.8% at the operating frequency $f = 1.3$ THz. In the meantime, the parameter of the

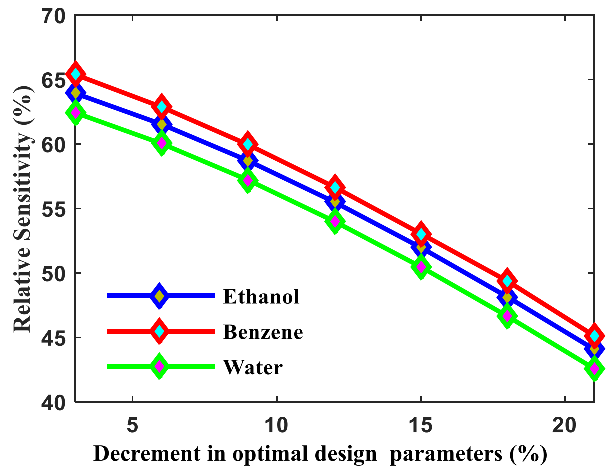

Fig. 4. Relative sensitivity as a function for different targeted analytes during the time of optimum parameter variations at pumping frequency $f = 1$ THz.

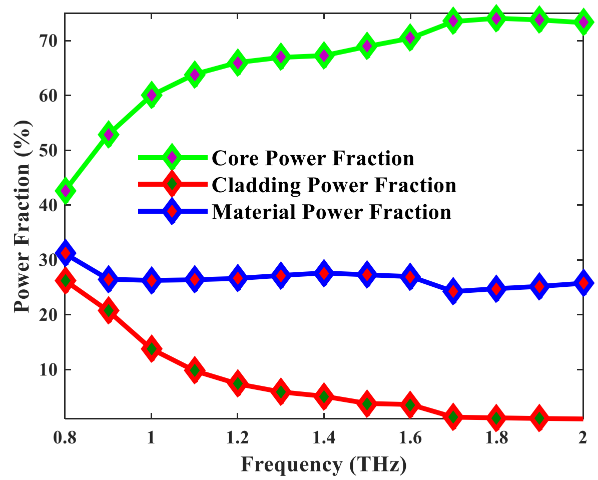

Fig. 5. Core, cladding and material power fraction as a function of applied frequency for the optimum designed parameters.

proposed PCF has been scaled from 0% to 22% and shown in Fig. 4 for same targeted analytes.

Power fraction of the PCF is now analyzed and plotted with the help of Equation (3). Here three different regions such as core region, cladding region and material region power fraction are derived. The power fraction curves of the core region, cladding region and material are separately shown in Fig. 5 with green, red and blue colored. From the figure it can be easily inferred that the green colored curves rise, which accords with the aforementioned sensitivity curve of Fig. 3. This is because higher core power fraction implies that greater optical interaction occurs. Besides cladding and material power fraction are negligible for the consideration of sensitivity calculation. Nevertheless, in Fig. 6, power fraction curves for core, cladding and material have been plotted in the case of the for a decrement in the optimized parameter values of the designed PCF. In Fig. 4, it refers the slope of core power fraction as negative, which implicitly satisfies the Fig. 6. These results are carrying the stronger impact of the proposed structure for installing as a sensing application.

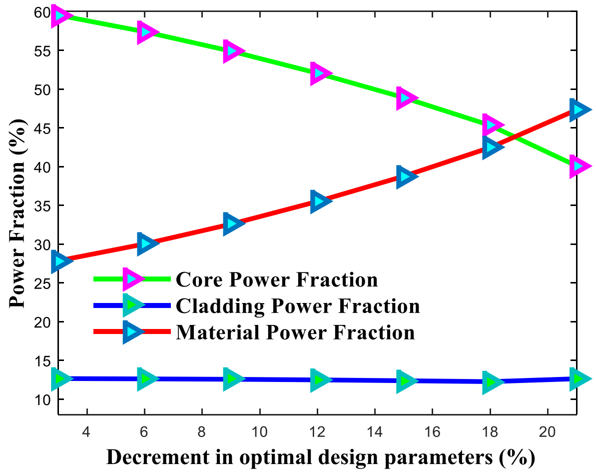

Fig. 6. Core, cladding and material power fraction as a function of applied frequency $f = 1$ THz versus the scaling of optimum designed parameters.

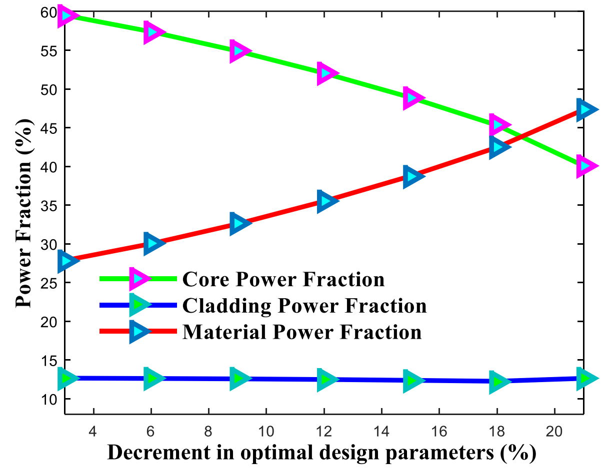

Fig. 8. Confinement loss as a function for different targeted analytes during the time of optimum parameter variations at frequency $f = 1$ THz.

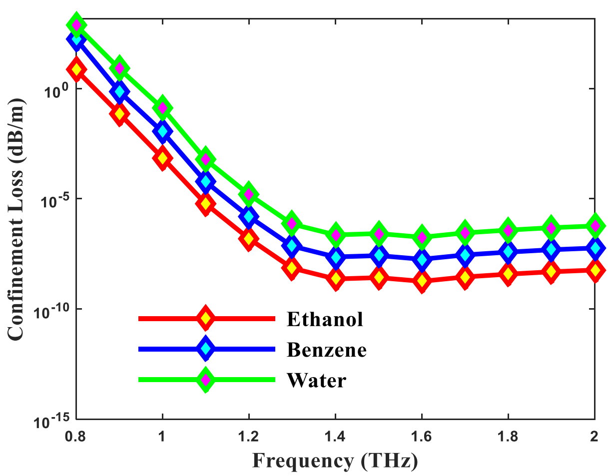

Fig. 7. Confinement loss as a function of frequency f for different targeted analytes over the wide frequency spectrum ranging from 0.8 to 2 THz.

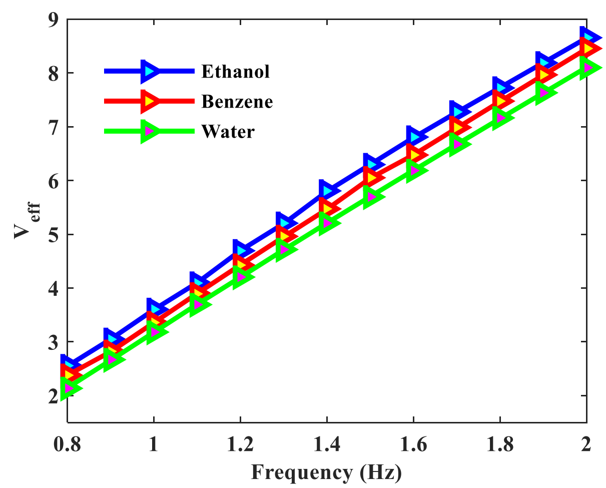

Fig. 9. Relationship of V parameter and applied frequency from 0.8 THz to 2 THz.

Confinement loss (CL) of the suggested PCF is computed by employing Equation (4). The CL for the investigated analytes water, benzene and ethanol is shown in Fig. 7 as a function of operating frequency. Here CL curve for all targeted analytes is falling sharply in the frequency range of 0.8 THz to 1.2 THz. But after 1.2 THz CL curves persist steadily. It is very interesting that for the whole operating frequency range lower index water carrying comparatively higher loss than ethanol. The maximum CL for water, benzene and ethanol are 7.51×10^2 dB/m, 1.80×10^2 dB/m and 7.15×10^2 dB/m respectively at $f = 0.8$ THz. Besides, the minimum CL for water, benzene and ethanol are 5.34×10^{-8} dB/m, 5.83×10^{-9} dB/m and 5.81×10^{-10} dB/m respectively in the flat 1.2 to 2.0 THz range. Moreover, these outcomes strongly accord with the sensitivity curve, which is plotted in Fig. 3. Here, it can be concluded that as CL reduces there is increased confinement and hence greater interaction with the analyte, thus explaining why sensitivity accordingly increases. Moreover, CL is investigated for the variation of the optical parameters at $f = 1$ THz. Here, it is found that a decrement in the optimal design parameters highly affects the CL curve. The higher decrement the higher the loss as shown in Fig. 8.

The mode parameter of the fiber is computed using Equation (4). In Fig. 9, it is noticed that proposed PCF exhibits the multimode behaviors through the whole region of 0.8 THz to 2 THz. Since the V_{eff} value of this operating region is greater than 2.405.

Lastly, for the NA of the proposed PCF is studied. A fiber with a high NA is in high demand for noninvasive medical imaging applications. For the study of NA, it is prerequisite to determine the effective mode area. The effective mode area and NA of the mentioned PCF is calculated with the help of Equations (6) and (7) respectively. Effective mode area versus frequency is depicted in Fig. 10 for investigating analytes. From the same figure, it can be easily inferred that when the frequency is shifted to the higher region then the transmitted optical pulse is more tightly confined into the innermost part of the PCF. The tighter confinement of the optical pulse into the core region produces a smaller effective mode area. These results entirely reflect in the Fig. 10. The NA versus frequency

TABLE I

COMPARISON OF THE PROPOSED Q-PCF WITH THE PREVIOUS PUBLISHED PCFS FOR VARIOUS OPTICAL PARAMETERS

Ref.	Operating point	Relative sensitivity	Confinement loss (dB/m)	NA	Base material
Ref. [39]	1.33 μm	53.22%	-	-	Silica
Ref. [36]	1.33 μm	49.17%	2.75×10^{-10}	-	Silica
Ref. [43]	1.33 μm	43.84%	2.07×10^{-06}	-	Silica
Ref. [44]	1.33 μm	62.19%	5.56×10^{-11}	-	Silica
Ref. [45]	1.33 μm	56.75%	5.05×10^{-13}	-	Silica
This work	230 μm	78.80%	2.19×10^{-10}	0.41	TOPAS

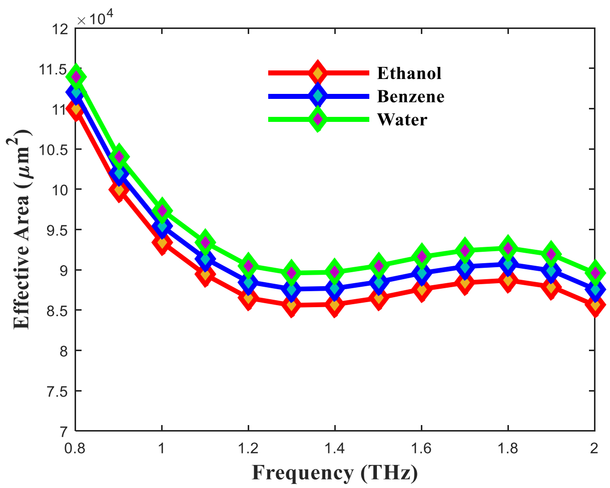

Fig. 10. Measurement of effective mode area with respect to applied frequency from 0.8 THz to 2 THz for different targeted analytes.

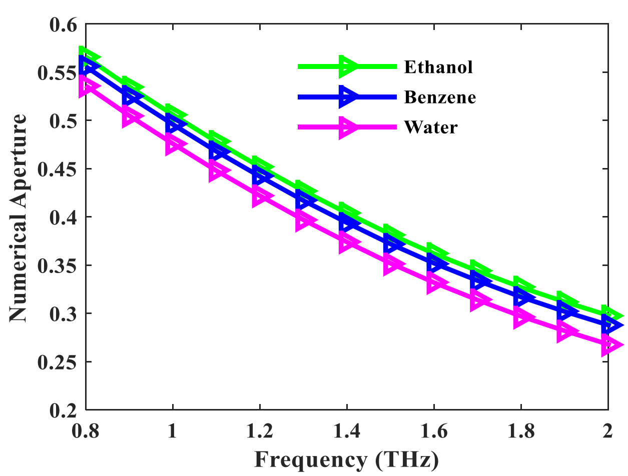

Fig. 11. Numerical aperture as a function of frequency of the proposed optimum designed structure.

has been depicted in Fig. 11. It is notable that the NA of silica based PCF more than 0.4 is rare [40]. But the proposed Q-PCF provides the high value of NA for ethanol, benzene and water are 0.57, 0.56 and 0.54 respectively at operating frequency $f = 0.8$ THz. Investigated results have been verified with the previous published standard articles [41], [42].

Beam divergence is the measurement of how rapidly the beams spreads from the beam waist. It also is a way of characterizing the beam quality. A low value of beam divergence leads to high beam quality or beam focusing. The decrement of beam divergence increases the beam intensity. The beam divergence is calculated following the article [40]. From Fig. 12, it is nicely exhibited that the beam divergence is below than 20 degrees.

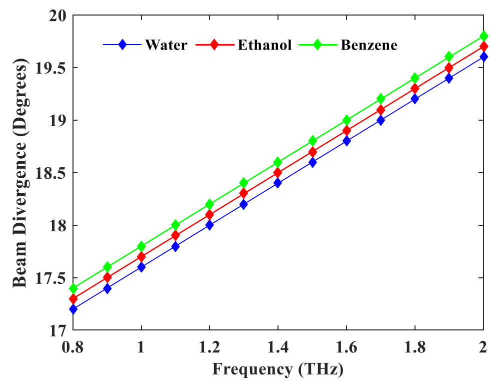

Fig. 12. Beam divergence as a function of frequency of the proposed optimum designed structure.

From Table 1, it is noted that the proposed PCF has superior optical properties than others standard articles those are already published. Note that although we have optimized geometric parameters in the PCF design, there is also a trade-off involved in selecting values appropriate for fabrication.

V. CONCLUSION

In this study, a Q-PCF has been presented for chemical sensing applications in the terahertz regime. The maximum sensing response occurs from the proposed model at $f = 1.3$ THz when the target analyte is ethanol. Furthermore, an extraordinary NA of 0.57 is also found from the same model when $f = 0.8$ THz, which may assist applications based on optical coherence tomography (OCT) as well as medical imaging applications.

REFERENCES

[1] L. Ho, M. Pepper, and P. Taday, "Terahertz spectroscopy: Signatures and fingerprints," *Nature Photon.*, vol. 2, pp. 541–543, Sep. 2008.

[2] B. Pradarutti *et al.*, "Multichannel balanced electro-optic detection for terahertz imaging," *Opt. Express*, vol. 15, no. 26, pp. 17652–17660, 2007.

[3] N. Laman, S. S. Harsha, D. Grischkowsky, and J. S. Melinger, "7 GHz resolution waveguide THz spectroscopy of explosives related solids showing new features," *Opt. Express*, vol. 16, no. 6, pp. 4094–4105, 2008.

[4] C. J. Strachan *et al.*, "Using terahertz pulsed spectroscopy to quantify pharmaceutical polymorphism and crystallinity," *J. Pharmaceutical Sci.*, vol. 94, no. 4, pp. 837–846, 2005.

[5] D. Abbott and X.-C. Zhang, "Special issue on T-ray imaging, sensing, and retection," *Proc. IEEE*, vol. 95, no. 8, pp. 1509–1513, Aug. 2007.

[6] D. H. Martin and J. W. Bowen, "Long-wave optics," *IEEE Trans. Microw. Theory Techn.*, vol. 41, no. 10, pp. 1676–1690, Oct. 1993.

[7] R. J. Wylde and D. H. Martin, "Gaussian beam-mode analysis and phase-centers of corrugated feed horns," *IEEE Trans. Microw. Theory Techn.*, vol. 41, no. 10, pp. 1691–1699, Oct. 1993.

[8] B. M. Fischer *et al.*, "Terahertz time-domain spectroscopy and imaging of artificial RNA," *Opt. Express*, vol. 13, no. 14, pp. 5205–5215, Jul. 2005.

[9] A. G. Markelz, A. Roitberg, and E. J. Heilweil, "Pulsed terahertz spectroscopy of DNA, bovine serum albumin and collagen between 0.1 and 2.0 THz," *Chem. Phys. Lett.*, vol. 320, nos. 1–2, pp. 42–48, Mar. 2000.

[10] A. G. Markelz, J. R. Knab, J. Y. Chen, and Y. He, "Protein dynamical transition in terahertz dielectric response," *Chem. Phys. Lett.*, vol. 442, nos. 4–6, pp. 413–417, 2007.

[11] A. B. M. Fischer, M. Walther, and P. U. Jepsen, "Far-infrared vibrational modes of DNA components studied by terahertz time-domain spectroscopy," *Phys. Med. Biol.*, vol. 47, no. 21, pp. 3807–3814, Nov. 2002.

[12] C. Yu, S. Fan, Y. Sun, and E. Pickwell-MacPherson, "The potential of terahertz imaging for cancer diagnosis: A review of investigations to date," *Quant. Imag. Med. Surg.*, vol. 2, no. 1, pp. 33–45, Mar. 2012.

[13] J. S. Drukteinis, B. P. Mooney, C. I. Flowers, and R. A. Gatenby, "Beyond mammography: New frontiers in breast cancer screening," *Amer. J. Med.*, vol. 126, no. 6, pp. 472–479, 2013.

[14] R. Mendis and D. Grischkowsky, "THz interconnect with low-loss and low-group velocity dispersion," *IEEE Microw. Wireless Compon. Lett.*, vol. 11, no. 11, pp. 444–446, Nov. 2001.

[15] K. Wang and D. M. Mittleman, "Metal wires for terahertz wave guiding," *Nature*, vol. 432, no. 7015, pp. 376–379, 2004.

[16] E. Yablonovitch, "Photonic band-gap structures," *J. Opt. Soc. Amer. B, Opt. Phys.*, vol. 10, no. 2, pp. 283–295, 1993.

[17] M. Nagel, A. Marchewka, and H. Kurz, "Low-index discontinuity terahertz waveguides," *Opt. Express*, vol. 14, no. 21, pp. 9944–9954, Oct. 2006.

[18] H. Han, H. Park, M. Cho, and J. Kim, "Terahertz pulse propagation in a plastic photonic crystal fiber," *Phys. Med. Biol.*, vol. 47, no. 21, pp. 2634–2636, 2002.

[19] M. Goto, A. Quema, H. Takahashi, S. Ono, and N. Sarukura, "Teflon photonic crystal fiber as terahertz waveguide," *Jpn. J. Appl. Phys.*, vol. 43, no. 2B, Feb. 2004, Art. no. L317.

[20] M. Skorobogatiy and A. Dupuis, "Ferroelectric all-polymer hollow Bragg fibers for terahertz guidance," *Appl. Phys. Lett.*, vol. 90, no. 11, Mar. 2007, Art. no. 113514.

[21] K. Nielsen, H. K. Rasmussen, A. J. L. Adam, P. C. M. Planken, O. Bang, and P. U. Jepsen, "Bendable, low-loss topas fibers for the terahertz frequency range," *Opt. Express*, vol. 17, no. 10, pp. 8592–8601, May 2009.

[22] Y. S. Sun, Y.-F. Chau, H.-H. Yeh, L.-F. Shen, T.-J. Yang, and D. P. Tsai, "High birefringence photonic crystal fiber with a complex unit cell of asymmetric elliptical air hole cladding," *Appl. Opt.*, vol. 46, no. 22, pp. 5276–5281, Aug. 2007.

[23] J. C. Knight, T. A. Birks, P. S. J. Russell, and D. M. Atkin, "All-silica single-mode optical fiber with photonic crystal cladding," *Opt. Lett.*, vol. 21, no. 19, pp. 1547–1549, Oct. 1996.

[24] K. Saitoh, M. Koshiba, T. Hasegawa, and E. Sasaoka, "Chromatic dispersion control in photonic crystal fibers: Application to ultra-flattened dispersion," *Opt. Express*, vol. 11, no. 8, pp. 843–852, Apr. 2003.

[25] N. Ayyanar, R. V. J. Raja, D. Vigneswaran, B. Lakshmi, M. Sumathi, and K. Porsezian, "Highly efficient compact temperature sensor using liquid infiltrated asymmetric dual elliptical core photonic crystal fiber," *Opt. Mater.*, vol. 64, pp. 574–582, Feb. 2017.

[26] N. Ayyanar, D. Vigneswaran, M. Sharma, M. Sumathi, M. S. M. Rajan, and S. Konar, "Hydrostatic pressure sensor using high birefringence photonic crystal fibers," *IEEE Sensors J.*, vol. 17, no. 3, pp. 650–656, Feb. 2017.

[27] D. Vigneswaran, N. Ayyanar, M. Sharma, M. Sumathi, M. Rajan, and K. Porsezian, "Salinity sensor using photonic crystal fiber," *Sens. Actuators A, Phys.*, vol. 269, pp. 22–28, Jan. 2018.

[28] H. Thenmozhi, M. M. Rajan, V. Devika, D. Vigneswaran, and N. Ayyanar, "D-glucose sensor using photonic crystal fiber," *Optik-Int. J. Light Electron Opt.*, vol. 145, pp. 489–494, Sep. 2017.

[29] A. A. Rifat *et al.*, "Surface plasmon resonance photonic crystal fiber biosensor: A practical sensing approach," *IEEE Photon. Technol. Lett.*, vol. 27, no. 15, pp. 1628–1631, Aug. 1, 2015.

[30] M. F. H. Arif, S. Asaduzzaman, M. J. H. Biddut, and K. Ahmed, "Design and optimization of highly sensitive photonic crystal fiber with low confinement loss for ethanol detection," *Int. J. Technol.*, vol. 6, pp. 1068–1076, Jan. 2016.

[31] Y. L. Hoo, W. Jin, H. L. Ho, D. Wang, and R. S. Windeler, "Evanescent-wave gas sensing using microstructure fiber," *Opt. Eng.*, vol. 41, no. 1, pp. 8–10, Jan. 2002.

[32] C. M. B. Cordeiro *et al.*, "Microstructured-core optical fibre for evanescent sensing applications," *Opt. Express*, vol. 14, no. 26, pp. 13056–13066, Dec. 2006.

[33] T. M. Monro, D. J. Richardson, and P. J. Bennett, "Developing holey fibres for evanescent field devices," *Electron. Lett.*, vol. 35, no. 14, pp. 1188–1189, Jul. 1999.

[34] S. Olyaee, A. Naraghi, and V. Ahmadi, "High sensitivity evanescent-field gas sensor based on modified photonic crystal fiber for gas condensate and air pollution monitoring," *Optik-Int. J. Light Electron Opt.*, vol. 125, no. 1, pp. 596–600, Jan. 2014.

[35] X. Yu, Y. Sun, G. B. Ren, P. Shum, N. Q. Ngo, and Y. C. Kwok, "Evanescent field absorption sensor using a pure-silica defected-core photonic crystal fiber," *IEEE Photon. Technol. Lett.*, vol. 20, no. 5, pp. 336–338, Mar. 1, 2008.

[36] S. Asaduzzaman, K. Ahmed, T. Bhuiyan, and T. Farah, "Hybrid photonic crystal fiber in chemical sensing," *SpringerPlus*, vol. 5, Art no. 748, Dec. 2016.

[37] F. H. Arif, K. Ahmed, S. Asaduzzaman, and A. K. Azad, "Design and optimization of photonic crystal fiber for liquid sensing applications," *Photon. Sensors*, vol. 6, no. 3, pp. 279–288, Sep. 2016.

[38] K. Ahmed *et al.*, "Ultrahigh birefringence, ultralow material loss porous core single-mode fiber for terahertz wave guidance," *Appl. Opt.*, vol. 56, no. 12, pp. 3477–3483, 2017.

[39] M. S. Islam *et al.*, "Liquid-infiltrated photonic crystal fiber for sensing purpose: Design and analysis," *Alexandria Eng. J.*, to be published, doi: 10.1016/j.aej.2017.03.015.

[40] H. Ebendorff-Heidepriem, J. Schuppich, A. Dowler, L. Lima-Marques, and T. M. Monro, "3D-printed extrusion dies: A versatile approach to optical material processing," *Opt. Mater. Express*, vol. 4, no. 8, pp. 1494–1504, 2014.

[41] B. K. Paul, K. Ahmed, S. Asaduzzaman, and M. S. Islam, "Folded cladding porous shaped photonic crystal fiber with high sensitivity in optical sensing applications: Design and analysis," *Sens. Bio-Sens. Res.*, vol. 12, pp. 36–42, Feb. 2017.

[42] S. Chowdhury, S. Sen, K. Ahmed, and S. Asaduzzaman, "Design of highly sensible porous shaped photonic crystal fiber with strong confinement field for optical sensing," *Optik-Int. J. Light Electron Opt.*, vol. 142, pp. 541–549, Aug. 2017.

[43] M. F. H. Arif and M. J. H. Biddut, "Enhancement of relative sensitivity of photonic crystal fiber with high birefringence and low confinement loss," *Optik-Int. J. Light Electron Opt.*, vol. 131, pp. 697–704, Feb. 2017.

[44] K. Ahmed, M. S. Islam, and B. K. Paul, "Design and numerical analysis: Effect of core and cladding area on hybrid hexagonal microstructure optical fiber in environment pollution sensing applications," *Karbala Int. J. Mod. Sci.*, vol. 3, no. 1, pp. 29–38, Mar. 2017.

[45] K. Ahmed, M. Morshed, S. Asaduzzaman, and M. F. H. Arif, "Optimization and enhancement of liquid analyte sensing performance based on square-cored octagonal photonic crystal fiber," *Optik-Int. J. Light Electron Opt.*, vol. 131, pp. 687–696, Feb. 2017.

Bikash Kumar Paul received the B.Sc. Engineering degree in information and communication technology from Mawlana Bhashani Science and Technology University, Tangail, Bangladesh, in 2017. He joined the Department of Computer Science and Engineering, Ranada Prasad Shaha University, Narayanganj, in 2017, as a Faculty Member. He is currently a full-time Faculty Member with the Department of Software Engineering, Daffodil International University, Dhaka. He is an Active Research Member of the Group of Bio-photomatix. He has authored and co-authored over 25 international scientific papers and conference presentations. His current research interests are the development of surface plasmon resonance-based sensors, fiber-optic sensors, biophotonics, and low-loss terahertz waveguide. He is a member of the Society of Photographic Instrumentation Engineers and the Optical Society of America.

Kawsar Ahmed received the B.Sc. and M.Sc. Engineering degrees in information and communication technology from Mawlana Bhashani Science and Technology University, Tangail, Bangladesh. He joined the Information and Communication Technology Department and the Software Engineering Department, Daffodil International University, as a Lecturer. He is currently an Assistant Professor with the Department of Information and Communication Technology. He is also a Research Coordinator of the Group of Bio-photomatix. He has over 100 publications in IEEE, IET, the Optical Society of America (OSA), Elsevier, Springer, ISI, and PubMed indexed journals. He has published two books on bioinformatics and photonic sensor design. His research interests include sensor design, biophotonics, nanotechnology, data mining, and bioinformatics. He is a member of the Society of Photographic Instrumentation Engineers (SPIE) and OSA. He holds top position at his department as well as the university and is fourth top researcher in Bangladesh, in 2017 (Scopus indexed based). He received Gold Medals from the Engineering Faculty for both the B.Sc. (Eng.) and M.Sc. (Eng.) degrees from the Mawlana Bhashani Science and Technology University for his academic excellence. His research group received the SPIE Travelling Award and the Best Paper Award from the IEEE WIECON ECE-2015 Conference.

Dhasarathan Vigneswaran received the B.E. degree in electronics and communication from the Kamaraj College of Engineering and Technology and the Master of Engineering degree in optical communication from the Alagappa Chettiar College of Engineering and Technology. He is currently working on funded projects provided by the Department of Science Technology, India. He has published 35 journal articles and more than 25 conference articles. He is also carrying out experimental research with various international research industry partners. His major research area is photonics for communication, sensing, and switching applications.

Fahad Ahmed received the B.Sc. (Eng.) degree in information and communication technology from Mawlana Bhashani Science and Technology University, Bangladesh. He has several publications in reputed journals. His research interests include photonics, terahertz communication, chemical sensing, sensor design, photonics, biophotonics, nanotechnology, data mining, and bioinformatics.

Subrata Roy received the B.Sc. (Eng.) degree in information and communication technology from Mawlana Bhashani Science and Technology University, Bangladesh. His research interests include photonics, terahertz communication, chemical sensing, biophotonics, bioinformatics, and data mining.

Derek Abbott (M'85–SM'99–F'05) was born in London, U.K., in 1960. He received the B.Sc. (Hons.) degree in physics from Loughborough University, Loughborough, U.K., in 1982, and the Ph.D. degree in electrical and electronic engineering from The University of Adelaide, Adelaide, SA, Australia, in 1995, under the supervision of K. Eshraghian and B. R. Davis. From 1978 to 1986, he was a Research Engineer with the GEC Hirst Research Centre, London, U.K. From 1986 to 1987, he was a VLSI Design Engineer with Austek Microsystems, Australia. Since 1987, he has been with The University of Adelaide, where he is currently a Full Professor with the School of Electrical and Electronic Engineering. He coedited *Quantum Aspects of Life* (London, U.K.: Imperial College Press, 2008) and co-authored the book *Stochastic Resonance* (Cambridge, U.K.: Cambridge University Press, 2012) and *Terahertz Imaging for Biomedical Applications* (New York, NY, USA: Springer-Verlag, 2012). He holds over 800 publications/patents and has been an invited speaker at over 100 institutions. His interests are in the area of multidisciplinary physics and electronic engineering applied to complex systems. His research programs span a number of areas of stochastics, game theory, photonics, biomedical engineering, and computational neuroscience. Dr. Abbott is a Fellow of the Institute of Physics. He has received a number of awards, including the South Australian Tall Poppy Award for Science in 2004, the Premiers SA Great Award in Science and Technology for outstanding contributions to South Australia in 2004, the Australian Research Council Future Fellowship in 2012, The David Dewhurst Medal in 2015, and The Barry Inglis Medal in 2018. He has served as an Editor and/or a Guest Editor for a number of journals including the IEEE JOURNAL OF SOLID-STATE CIRCUITS, the *Journal of Optics B*, the *Microelectronics Journal*, *Chaos*, *Smart Structures and Materials*, *Fluctuation and Noise Letters*, PROCEEDINGS OF THE IEEE, IEEE PHOTONICS JOURNAL, and *PLOS One*. He is on the editorial boards of *Scientific Reports* (Nature), IEEE ACCESS, *Royal Society Online Science*, and *Frontiers of Physics*.

Accepted Manuscript

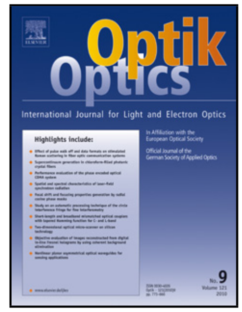

Title: Design of a Modified Single-negative metamaterial structure for sensing application

Authors: K. Srinivasan, Naim Ben Ali, Youssef Trabelsi, M.S. Mani Rajan, Mounir Kanzari

PII: S0030-4026(18)31936-3
DOI: https://doi.org/10.1016/j.ijleo.2018.12.012
Reference: IJLEO 62028

To appear in:

Received date: 2 December 2018
Accepted date: 4 December 2018

Please cite this article as: Srinivasan K, Ali NB, Trabelsi Y, Mani Rajan MS, Kanzari M, Design of a Modified Single-negative metamaterial structure for sensing application, *Optik* (2018), https://doi.org/10.1016/j.ijleo.2018.12.012

Design of a Modified Single-negative metamaterial structure for sensing application

K. Srinivasan[1], Naim Ben Ali[2,3], Youssef Trabelsi[3,4], M.S. Mani Rajan[5*] and Mounir Kanzari[3]

[1]Department of Electronics and Communication, Sri Krishna college of Technology, Coimbatore, India 641 042.

[2]College of Engineering of Hail, Industrial Engineering Department , University of Hail, 2440-Haïl City , Saudi Arabia

[3]University of Tunis EL Manar, Laboratory of Photovoltaic and Semiconductor Materials (LPMS), ENIT Tunis, 1002, Tunisia.

[4]King Khaled university, College of Arts and Sciences in Mahayel Aseer, Physics Department, KSA.

[5]Department of Physics, University College of Engineering, Anna University, Ramanathapuram 623513, India.

Abstract

A new topology of modified negative effective permeability material (NEPM) are studied by adding a small similar form with different angles to the basic single split-ring resonators. we report our work conducted on the design, simulation and micro-fabrication of sensing system based on a modified split-ring resonator (MSRR) structure around 140 GHz operation frequency. Once the NEPM cells are excited, the reflection and transmission coefficients from the excitation mechanism can be measured by using quasi-optical technique with normal incidence. It has been shown that our proposal NEPM exhibits a high resonant frequency which is extraordinarily sensitive to the changes of the geometries and the properties of metal shape. By applying the new design of square Plus symbol (+) curve to the SRRs, more condensed size and higher sensitivity can be attained compared to conventional SRRs. Furthermore, the enhancement of sensitivity of the new design is also exposed. The considered sample double defect corner square modified form (DCD^2) is fabricated in our lab using a conventional printed circuit board process with 2µm aluminum and validated by comparing simulated profiles with measurements.

Keywords: Metamaterial, Resonators, Modified split ring resonators, sensors.

1 Introduction

Metamaterials belong to the class of ordered composites that reveal special properties which are not readily observed in nature. This type of materials comprises a wide set of artificially structured composites with tunable μ_{eff} and ε_{eff} that are inaccessible or difficult to obtain with natural materials. In recent years, the propagation of electromagnetic waves in this periodic artificial composite material has gained a great deal of attentions [1–4]. Left-handed materials can be commonly classified as double-negative metamaterials (DNM) and single-negative metamaterials (SNM). DNM is a new type of artificial, electromagnetic materials that have both the effective permittivity and permeability are negative. It would possess unique properties such as negative index of refraction, reversed Cherenkov radiation (RCR), and Reversed Doppler Effect [5,6].

On the other hand, single-negative metamaterials (SNM) have either negative permittivity or negative permeability. Similarly, many studies based on different modified split ring resonator (m-SRR) shapes have been recently made to investigate interesting resonant properties and new behaviors have been discovered which are not achievable by conventional SRR [7-12]. Hence, the insert of defect of metamaterial cell can be crucially developed to change the properties of SRRs [13-17].

Indeed, it has been pointed out that changing of the type and properties of thin film put under or a top of planar metallic SRR can be used effectively to control the sensitivity of SRR. The phenomena of resonance of the circular SRR are due to the interaction between the electromagnetic fields and the metallic strips. Indeed, it is result of two effects: a capacitive response due to the presence of gaps between wires and an inductive effect due to the interaction of the magnetic field with the ring shaped strips.

In this paper, we investigate a new shape of SRR based on deformation of the four corners of the conventional SRR. The specific topology of modified SRR is designed to exhibit negative permeability behavior in the mm-wave frequency range, precisely at D-band frequency. The characteristics of the new model are studied and the typical measurements of the transmission and refection coefficients using quasi-optical technique with normal incidence were extracted using the vector network analyzer. The effect of different geometrical restrictions and the order of the modified design on the performances are investigated.

2 Modified metamaterial for Single corner Defect structure

The current structure is constructed on a 350μm-thick on Quartz substrate with a dielectric constant of 3.78, a loss tangent of 0.0027 and the metal array layer is aluminum with the thickness of 8μm. The incident wave propagates at normal incidence with the mutually orthogonal electric and magnetic fields lying completely on the parallel plane to the metal. A thin film are put a top of the substrate. The structure is placed inside the D-band waveguide with dimensions of 0.5 mm × 0.5 mm × 0.3mm.The polarization of the microwave electric field is perpendicular to the capacitive gap (Figure1).

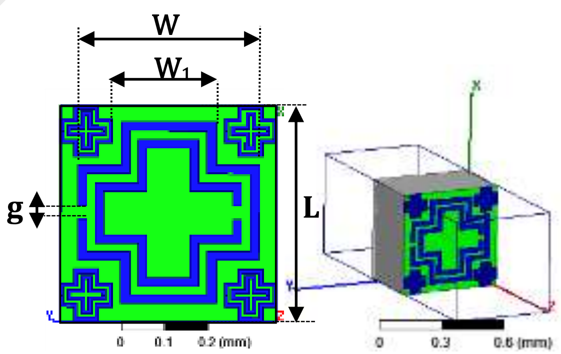

Figure 1: Geometrical configuration of Single corner defect (SCD) modified metamaterial slab. Parameters are: W=400μm, L=500μm, W_1=140μm, g=30μm.

The figure 2 show respectively that the spectrum clearly depends on the thicknesses of the thin film d(μm) and thicknesses of metal t (μm). It is clear that the resonance frequency shifts upwards to higher values for an increase in d[μm] due to essentially of a decrease of coupling SRR capacitance. Whatever, the position of the LC resonance frequency can usually be described by a simple expression, $f_0 = \frac{1}{\sqrt{LC}}$, where L and C are the effective inductance and capacitance of the individual SRR. Nevertheless, it is observed that the resonant frequency shift further downward gradually as the thicknesses of aluminum decreases and reaches 141 GHz for t=8μm (Fig.2-b). Thus, the high dip of resonance in the spectrum appear for a highly conductive metallic ring which correspond essentially to a lower value of SRR capacitance compare to the rest of thicknesses.

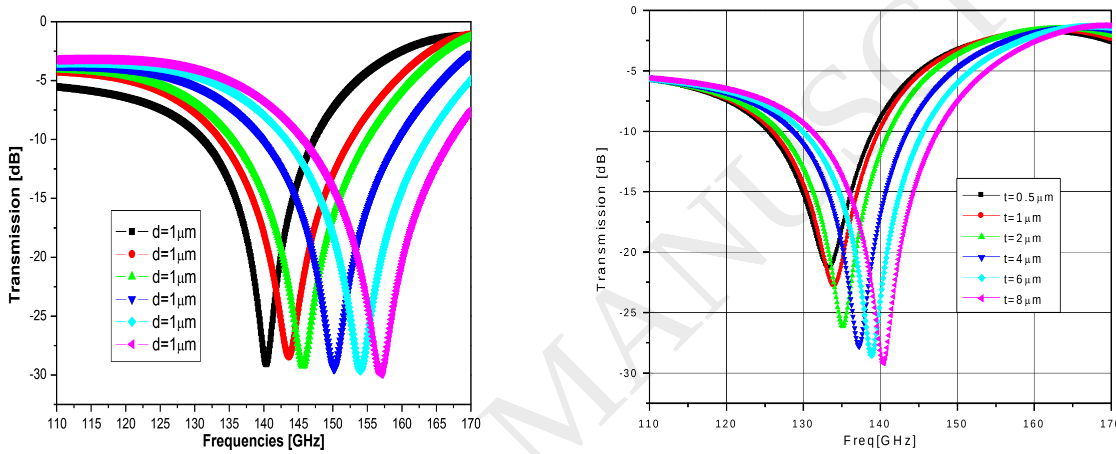

(a) (b)

Figure 2: Transmissions Spectrum of the SCD split ring resonator unit cells for (a): different thin films deposited on the upper surface of Quartz substrate d(μm), (b): different aluminum thicknesses t(μm).

3. Double Defect corner (DCD) Modified Negative Effective Permeability Metamaterial (NEPM) structures and simulation results.

All the SRRs materials studied here have been fabricated using a conventional printed circuit board process with 8 μm-thick aluminum patterns on 300 μm thick Quartz glass dielectric substrates with respectively dielectric constant ε_r =3.78 and a dissipation factor tan δ=0.027 at 10 GHz. The changes in the transmission resonances are examined upon variation of modified geometries inside the basic DCD split ring resonator cell.

The geometric parameters are as following: w =420μm, g=30μm and c=d=20μm, where w is the patch width, g is the gap width, d is the DCD width and c is the ring spacing between two SRRs.

w_1 and w_2 are respectively the length of new bending engender by the modification of sample square equal respectively : w_1=340μm and w_2=220μm.
For the design procedure, one unit cell of the metamaterial was positioned inside a waveguide with the setting of PEC and PMC boundary conditions at its side-walls to support a constant profile transverse electromagnetic wave. Waveguide ports were placed at the entrance and exit of the waveguide, serving as source and detector, respectively. The incident electromagnetic wave propagates along x direction, while the electric field (E) is kept along y direction and the magnetic field (H) is kept along the z direction (Figure 3).

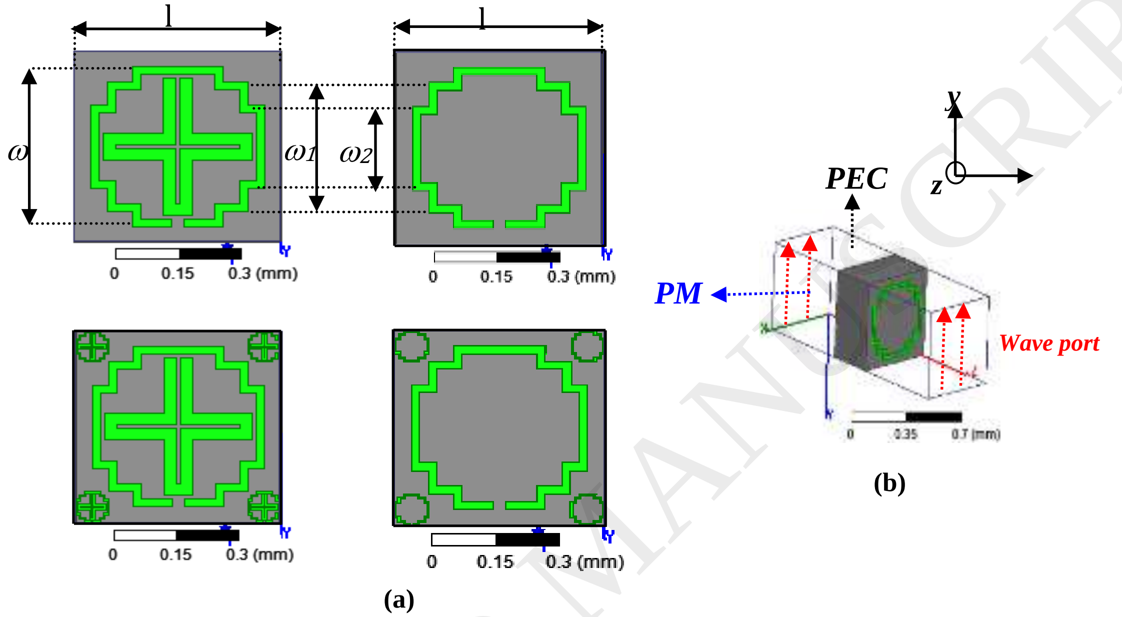

Figure 3: (a): Schematic view of Double corner defect of NEPM ,(b): Three dimensional Double Corner Defect Load configuration and boundary conditions.

It is known that the single SRRs behave as an LC circuit. The metallic ring works as a coil or inductance (L) and the split in the ring generates a parallel plate capacitor (capacitance C). The resonance appears in the SRR when the electric energy stocked in the capacitor is balanced with the magnetic energy stored in the inductor. The exchange in capacitance or inductance due to dielectric loading from dielectric samples leads to a significant shift in the resonant frequency. The resonant frequency is given by:$f_0 = \frac{1}{\sqrt{LC}}$.
The overall capacitance consists mainly of three capacitors: the gap capacitance (Cg), the coupling capacitance formed between the ring and its neighbors and the surface capacitance formed between the ring and the substrate. These three capacitors are supposed to be connected in parallel.
As shown in Figure 4 that the coupling capacitors of SRR are C_1, C_2 and C_3 while SCD has C_a, C_b and C_c. However, adding corner defects to the convention square SRR, as in SCD, works as splitting up the coupling capacitor C_3 to three smaller capacitors (C_{c1}, C_{c2} and C_{c3}). Also, the coupling capacitors C1 and C2 of SRR are divided into smaller capacitors (C_{a1}, C_{b1}) and (C_{a2}, C_{b2}) respectively. However, the splitting process decreases the coupling capacitors which reduce the overall capacitance of the ring which in turn increases the resonant frequency.

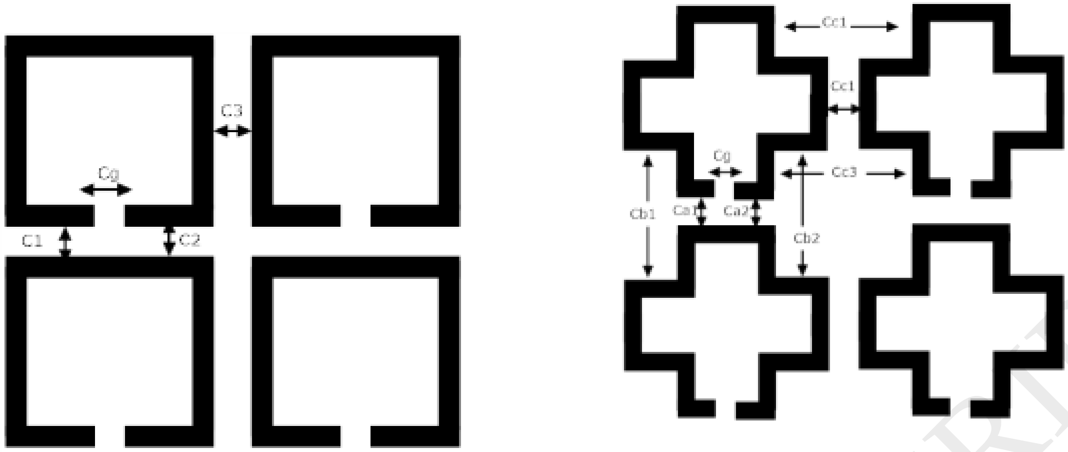

(a) (b)

Figure 4: The coupling capacitors of a) SRR and b) SCD

3.1 Thin film DCD modified split ring resonator

To explore the characteristic of dielectric sensing, transmission spectrum was simulated for a variation of thicknesses thin film under the aluminum modified metamaterial shape. The spectrum clearly depends on the thicknesses of the thin film of silicon with permittivity $\varepsilon_r = 11.9$. By increasing the thicknesses, the resonance shifts downwards as show in figure 6, when the thickness is $2\mu m$ the SRR resonate at 151 GHz.

It was found that in the frequency vary of 139 GHz to 165 GHz; the peak position of the resonant mode shifted to lower frequencies range with increase the thicknesses of thin film. It was noted that the cutoff mode is dependent on the resonance, since the peak position changes with the thin film.

Another interesting aspect, which is visualized in figure 5, is the fact that the transmission responses for different thin film are progressively shifted towards left, but their peaks are not consistent with the variation thicknesses constant increase.

The results show that the peak frequency of transmission coefficient S_{21}depends critically on the permittivity of the sample in the detecting zone, while the amplitude of S_{21} is a complicated function of the permittivity and topological structure of the coupled metamaterial.

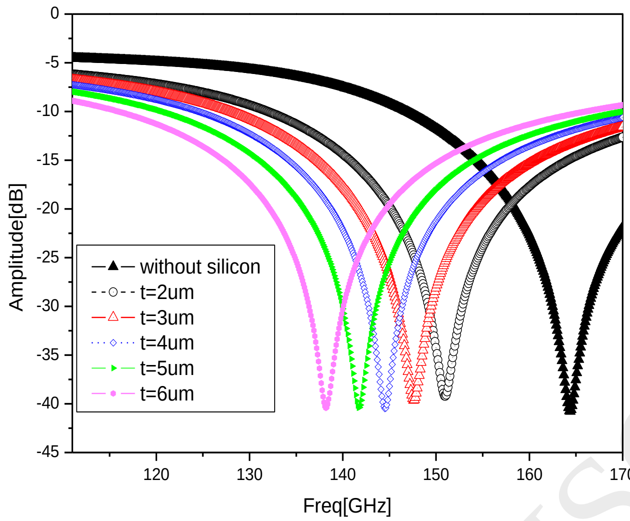

Figure 5 : Transmission spectrum in [dB] versus frequency for different thicknesses silicon thin film put under aluminums DCD split ring resonator modified Form.

3.2 Effect of insertion of compact small double defect corner (DCD) metamaterials cell

Different insertion of small double defect corner cells inside and around the basic modified metamaterials show and improves respectively the shift of resonant frequency towards left where the number of small corners defect increase. It can be seen that in the figure 6 the resonance frequency is very sensitive to the variation of the number of small DCD around and inside the basic DCD cell. Wherever, the fundamental frequency of the resonator has changed into 156 GHz from 162 GHz. Therefore, by adding a new small defect corner for each step an external field excitation on the alignment of LCs, the typical modified metamaterial structure studied m-SRR structure provides a good tenability on the frequency shift of the magnetic resonant response. In fact, increasing the number of small DCD causes a decrease of distributed capacitive effect (C_{add}).

Overlapping conducting strips are printed on the substrate. Consequently, the m-SRR structure resonates at lower frequencies for the amplifying of value of small DCD cells noted N. As N increases, however, C_{add} decreases with increasing in resonance frequency of the m-SRR structure. This means also a strongly concentrate external magnetic field penetrates through the rings by the metal in structure which contain a great number of small DCD cells and induced a powerfully current which responsible for resonant transmission. This shift in the resonance is attributed to an increase in capacitance as well as change in inductance of the resonator surface. It should be clear that the magnetic resonance frequency could be further increased by reducing the net capacitance.

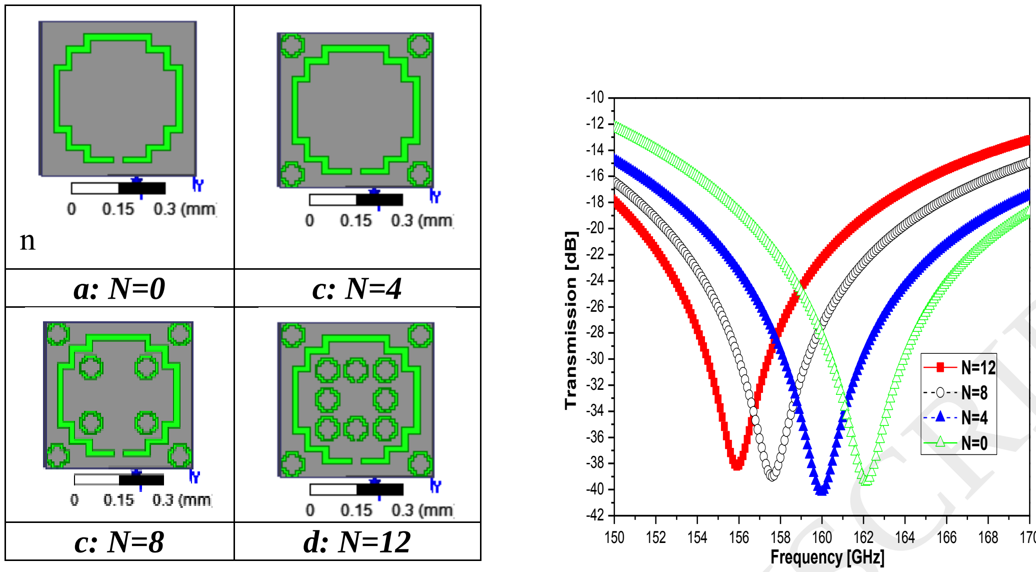

Figure 6: Transmission spectrums of the basic double corner defect (DCD) cells with different insert small DCD cells noted N for: Basic DCD without small insert cell without DCD (N=0), Four small DCD insert cells (N=4), (c) Eight small DCD insert cells (N=8), (d): Twelve small DCD insert cells (N=12).

4. Theoretical formulation of retrieval effective parameters

Equations 1and 2 express respectively the S parameters which are the plane wave reflection and transmission coefficients for a planar slab with a complex impedance Z and complex wave number γ [18] .

$$S_{11} = \frac{\Gamma(1-T^2)}{1-\Gamma^2 T^2} \qquad (1)$$

$$S_{21} = \frac{T(1-\Gamma^2)}{1-\Gamma^2 T^2} \qquad (2)$$

where, Γ and T are respectively the reflection coefficient of the air sample interface and transmission coefficient. Γ and T can be written in the following form:

$$\Gamma = \left(\frac{Z-1}{Z+1}\right) \; and \;\; T = e^{-\gamma d} \qquad (3)$$

In equation (3) Z and γ are respectively the normalized characteristic impedance and propagation constant of sample and d represent the thickness of sample. They are related to ε and μ by the following relationships:

$$Z = \sqrt{\frac{\mu}{\varepsilon}} \;\; ; \quad \gamma = \gamma_0 \sqrt{\epsilon\mu} \qquad (4)$$

γ_0 represent the propagation constant of free space written in the following form : $\gamma_0 = j\frac{2\pi}{\lambda_0}$, where λ_0 is the free space wavelength. From (1) and (2) one may derive that:

$$\Gamma = k \pm \sqrt{(k^2-1)}\,; \qquad T = \frac{S_{11}+S_{21}\text{-}\Gamma}{1-(S_{11}+S_{21})\Gamma} \tag{5}$$

Where, $k = \frac{S^2{}_{11}\text{-}S^2{}_{21}+1}{2S_{11}}$.

The propagation constant γ is can be related to the transmission T by the following form $\gamma=\ln(\frac{1}{T})/d$. From the equation (3) and (4), we can extract that:

$$\sqrt{\frac{\mu}{\varepsilon}} = \frac{1+\Gamma}{1-\Gamma} \tag{6}$$

The effective permittivity and effective permeability take the forms 7:

$$\varepsilon = \frac{\gamma}{\gamma_0}\frac{1-\Gamma}{1+\Gamma}\ \ ;\ \mu = \frac{\gamma}{\gamma_0}\frac{1+\Gamma}{1-+\Gamma} \tag{7}$$

5. Results and Fabrication process

The fabrication process has been through using negative photolithography. Firstly, we put at surface substrate Quartz a thin aluminum layer. After that a light sensitive photoresist is spun onto the wafer forming a thin layer on the surface. The resist is then selectively exposed by brilliant light done a mask which contains the design information for the specific being fabricated. The resist is then developed which completes the pattern transfer from the mask to the wafer.

The full steps are clarified by the following step:

1. Surface substrate Quartz covers by aluminum (cleaned and dray wafer by aluminum metal).
2. Applying the photoresist (Spin coat a thin layer photoresist on surface with several 1.000 rounds per minute (rpm) distributes few ml of resist over the substrate. The thicknesses created of photoresist is around are 1.4µm.
3. Soft bake : Practical evaporation of photoresist solvent by heating at 120 (The temperatu re rise starts at bottom of wafer and works upward, more thoroughly evaporating the coati ng solvent.
4. Alignment and exposure (precise alignment of mask particle and exposure of photoresist by Mg (λ=365nm). The 1 Karl Suss MJB3 is used for mask alignment and exposure. The exposure time is between 0 s and 30 min for2” diameter wafers.

The material consists of a two-dimensional array of repeated unit cells of aluminium strips and split ring resonators on interconnecting and disconnecting strips of standard circuit material. The considered fractal SRR metamaterial was fabricated by Liftoff micro-fabrication techniques. 400nm metal thick SRRs structures made of Aluminium were patterned on Quartz glass with thickness of 350µm.The complex relative permittivity of fused Quartz is assumed as 3.78-j0.0006. The thicknesses Quartz plate is 314µm while the aluminum plate thicknesses are 4770 Å.

The considered sample double defect corner square modified form (DCD^2) is fabricated in our lab using a conventional printed circuit board process with 2µm aluminum thick patterns on 314µm thick of quartz substrate with dielectric constant ε_r=3.78+0.0006i and a dissipation factor δ=0.027 at 10 GHz (Figure 7). The fabrication process has been performed using the negative photolithography.

A thin aluminum was placed on the surface of quartz substrate, after that a light sensitive photoresist is spun onto the wafer forming a thin layer on the surface. The spin coating has been made on surface with 1.000 rounds per minute (rpm) to distribute a few ml of resist over the substrate. The thicknesses created of photoresist are about 1.4 µm.

In the next step, the surface is exposed by brilliant light a mask which contains the design formation, then the resist is developed which completes the pattern transfer from the mask to the wafer. The final step is the soft baking. In this steps a practical evaporation of photoresist solvent by heating at 120°C.The temperature rise starts at bottom of wafer and works upward, more thoroughly evaporating the coating solvent. In addition, the alignment of mask particle is assured by the mask gasket and the exposure of photoresist is assured by brilliant light (λ=365nm).

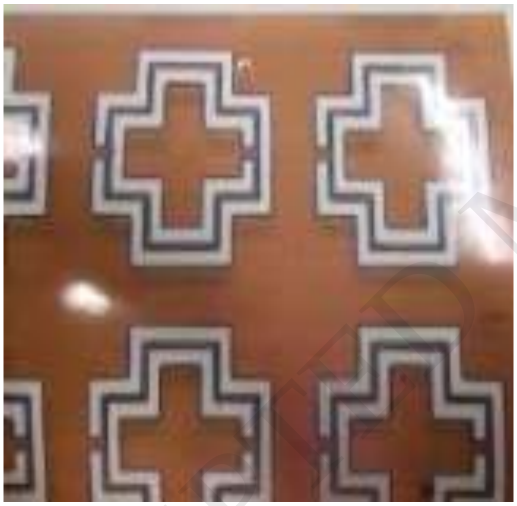

(a)

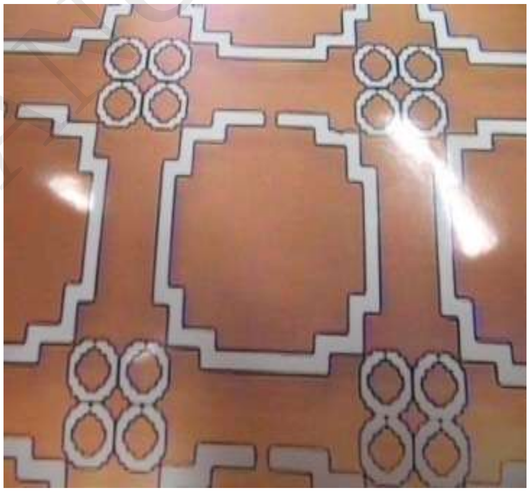

(b)

Figure 7: Photograph of all modified SRR : a- SRR with single corner defect and b- SRR with double defect corner square (DCD^2) cells based on transparent quartz substrate Microscopic image of the DCD^2 structure.

The material consists of a two-dimensional array of repeated unit cells of aluminum strips and split ring resonators on interconnecting and disconnecting strips of standard circuit material. By measuring the transmission and spectrum through a m-SRRs aluminum stroked at a top of Quartz substrate, we determine the effective n, appropriate to relation: $Z = \mu\ \varepsilon$.

The millimeter wave measurements were carried out by using an ABMM network analyzer. First, the signal from the network analyzer was converted up in frequency to the 110-170 GHz range by using a multiplier source unit. The signal was transmitted by a horn antenna. The transmission

through a stack of samples was measured by a second horn antenna and mixing detector combination. The resonance by DCD^2 split ring resonator was verified simply by measuring the transmission spectrum. Transmission measurements were performed by using two waveguides as a transmitter and a receiver, which were connected to the vector network analyzer AB millimeter 8-350-2 (VNA)[19] in the frequency range of 110 to 170 GHz as shown in figure 8-a.
Figure 8-b presents the calculated real and imaginary parts of the permeability from the measured data using the NRZ retrieval procedure. A m-SRRs system can be described by a resonant effective permeability, which is regularly followed by a negative permeability regime. One way to trace the negative permeability regime in SRRs systems is over transmission measurements or simulations, where this regime appears as a transmission dip. The figure shows the negative permeability of the DCD^2 around the resonant frequency and precisely at 135 GHz. As expected, the resonant frequency highly depends on the effective permittivity and permeability.

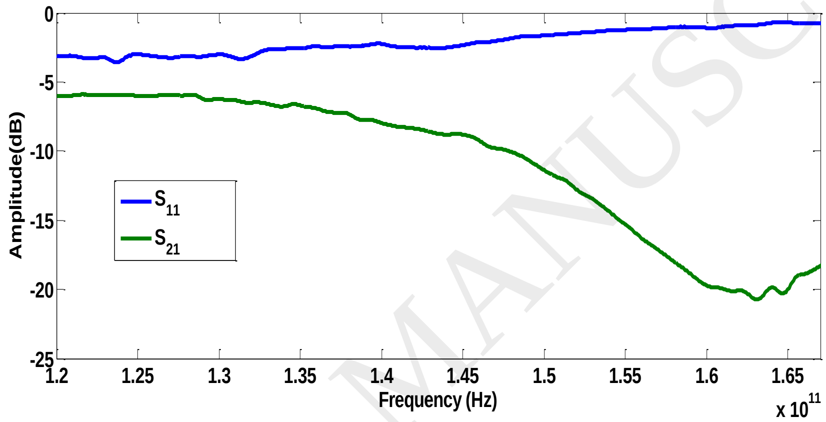

(a)

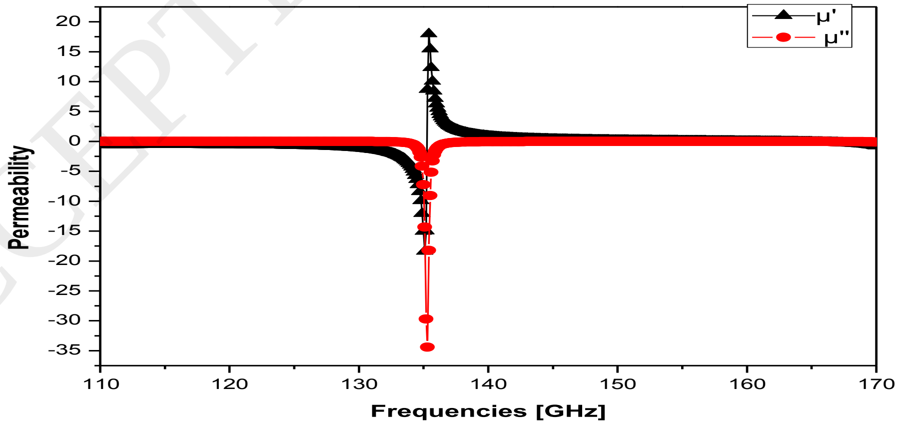

(b)

Figure 8 : (a) : Measured reflection (S_{11}) in blue line and transmission (green line) of (DCD^2) structure , (b) : The retrieved results for the real and imaginary parts of the effective permeability Re (μ') (Black line) and Im (μ) (red line) of the (DCD^2) split ring resonator.

6. Conclusions

New modified negative-permeability designs that have negative refraction index were developed in the mm-wave frequency range. The basic structure is composed by adding corner defects to the conventional square split ring. We found out that the resonance frequency is sensitive to the variation of geometric parameters, numbers of cells and properties of the substrate materials.

In addition to the additional capacitance and inductance of the rings, the cells were fabricated using a lithography technique process. The transmission spectrum was measured in the frequency range of 110 to 170 GHz. The simulations were compared with the measurements. Furthermore, the model can be used with enough accuracy to analyze the behavior of the modified split-ring resonator structures and it can be used for different application such as filtering and sensing.

References

[1] J.B. Pendry and D. R. Smith, “Reversing Light with Negative Refraction,” Phys. Today **57**(6),(2004).

[2]N. Seddon and T. Bearpark, “Observation of the inverse Doppler effect,”*Science*, **302**(5650) , (2003).

[3] O. Turkmen1, E. Ekmekci1 and G. Turhan-Sayan1, “A new multi-ring SRR type metamaterial Design with Multiple magnetic resonances ,” Progress In Electromagnetics Research Symposium Proceedings, Marrakesh, Morocco,2011.

[4]E. Ekmekci, K. Topalli, T. Aki, and G. Turhan-Sayan, “A tunable multi-band metamaterial design using micro-split SRR structures,”*Opt. Express***17**(18),(2009).

[5]A. Ishimaru, S. Jaruwatanadilok and Y. Kuga, “Generalized surface plasmon resonance sensors using metamaterials and negative index materials,”*Progress In Electromagnetics Research***51**(2005).

[6]Z.Y. Duan, B.I. Wu, J. Lu, J. A. Kong, and M. Chen, “ Reversed Cherenkov radiation in unbounded anisotropic double-negative metamaterials,” *Journal of Phy. D: App. Phys*.**42,** 185102(2009).

[7] A. C. Strikwerda, Maksim Zalkovskij, Dennis Lund Lorenzen, Alexander Krabbe, Andrei V. Lavrinenko, and Peter UhdJepsen , “Metamaterial composite bandpass filter with an ultra-broadband rejection bandwidth of up to 240 terahertz,” *App. Phys. Letters***104**(2014).

[8] R. Singh, I.A.I Al-Naib, M. Koch, and W. Zhang, "Asymmetric planar terahertz metamaterials, " *Opt. Society of America***18**(12),(2010).

[9] Y. Ma, H. Zhang, Y. Li, Y. Wang and W. Lai , “Terahertz sensing application by using fractal geometries of split-ring resonators,” *Progress In Electromagnetics Research*, **138** (2013).

[10] O. Paul, R. Beigang and M.Rahm , “Highly Selective Terahertz Bandpass Filters Based on Trapped Mode excitation,” *Opt. Express*, **17**(21), (2009).

[11] M. Gregor, and K.M. Hock, “Complementary split-ring resonator-based deflecting structure,”*American Physical Society***16**(2013).

[12] Y. Huang, G. Wen, and J. Li, “Systematical analysis for the mixed couplings of two adjacent modified split ring resonators and the application to compact micro strip band pass filters ,” *AIP ADVANCES* **4**(2014).

[13] A. H. Reja, S. N. Ahmad and M. A. Alqaisy, "Study the Effect of SRRs on Broadband Microwave parallel-coupled band-pass filters, "*International Journal of Computer and Electrical Engineering***6** (2014).
[14] Y. Liu, X.Tang, Z. Zhang, and X.Huang , "Novel nested split-ring-resonator (SRR) for compact filter application,"*Progress In Electromagnetics Research***136**(2013).
[15] Q. Shen, B. Hou, Z. Chen, and Z. Wang, " Effect of gap width on enhanced magnetic optical fields in metallic split ring resonators",*AIP Advances* **2**,(2012).
[16]P. Koziol , A. J. Antonczak , P. E. Szymczyk , B. Stępak , L. Lazarek , M. R. Wojcik , M. Walczakowski and K. M. Abramski, "Split-ring resonators manufactured on conductive layer by selective laser ablation,"*Proc. SPIE* **9286**, 92860Y (2014)[doi:10.1117/12.2063665].
[17] H. J. Lee, J.H.Lee , S. Choi , I.S. Jang, J.S. Choi and H. Jung, " Asymmetric split-ring resonator-based biosensor for detection of label-free stress biomarkers ," *App. Phys. LETT.***103**(2013).
[18] R. W. Ziolkowski, , "Propagation in and scattering from a matched metamaterial having a zero index of refraction ," *Phys. Rev.E* 70, (2004).
[19] AB millimetre, available at: http://www.abmillimetre.com.

Journal of Superconductivity and Novel Magnetism
https://doi.org/10.1007/s10948-018-4716-6

ORIGINAL PAPER

Superconductor Nanometallic Photonic Crystals as a Novel Smart Window for Low-Temperature Applications

Arafa H. Aly[1] · Ayman A. Ameen[2] · D. Vigneswaran[3]

Received: 23 April 2018 / Accepted: 27 April 2018

Abstract

The control of electromagnetic wave propagation has played an essential role in recent technology. In this paper, we present a novel type of smart window using one-dimensional superconductor nanometallic photonic crystals. The present idea depends on the control of the transmittance values based on the angle of incidence of the electromagnetic waves. We have investigated the transmittance of the proposed novel smart window based on a two-fluid model and a characteristic matrix method. We also obtained the effect of the operating temperature, number of periods, and thicknesses of the constituent materials. Finally, the proposed design promises for useful applications such as space exploration, satellites, and low-temperature applications.

Keywords Smart window · Photonic crystals · Superconductor · Transmittance

1 Introduction

Photonic crystals (PCs) are periodic structures in which the refractive indices of the constituent materials are changing periodically [1–3]. PCs are particularly designed to control the electromagnetic wave propagation. The periodicity of refractive indices in these structures produces frequency regions that are not allowed for the incident electromagnetic waves to propagate due to Bragg scattering at the interfaces. These forbidden frequencies are called photonic band gaps (PBG) [4–8] and predicted for the first time by Yablonovitch [9] and John [10]. Many papers are published in one-dimensional (1D), two-dimensional (2D), and three-dimensional (3D) photonic crystals [11–18].

Though initially, PCs were designed from dielectrics [19]. Later, the dispersive media like metals, semiconductors, superconductors, and plasma topped the scene for the design and fabrications of PCs because of their peculiar optical characteristics [20–27]. Moreover, the optical properties of these materials could be controlled by using many external influences such as magnetic field [28], electric field [29], pressure, and the density of charge carriers [25].

Meanwhile, the permittivity of superconductors has a clear adoption of the temperature and magnetic field [30–32]. Due to these properties, superconductors found its way toward PC design because of its ability to investigate wider PBGs, lower losses, and lower dispersion compared with dielectric or normal metal ones [33–36].

The possibility of controlling the electromagnetic wave propagation reliance on PCs paved the way to solve hard problems such as biomedical applications [37–39] and processing information [40, 41].

In this paper, a novel smart window is designed by using one-dimensional superconductor metallic PCs. Numerical results have been explored based on the two-fluid model and the characteristic matrix method. The current design essentially depends on the transmittance properties by changing the angle of incidence. The effects of many parameters such as the thicknesses of the constituent materials, the number of periods, and the operating temperature are considered.

✉ Arafa H. Aly
arafa.hussien@science.bsu.edu.eg; arafa16@yahoo.com

1 Physics Department, Faculty of Sciences, Beni-Suef University, Beni-Suef, Egypt

2 Physics Department, Faculty of Sciences, Sohag University, Sohag, Egypt

3 Department of ECE, Sri Krishna College of Technology, Coimbatore, 641042, India

2 Theoretical Model

In this section, we introduce the theoretical model of the proposed smart window. The cornerstone of this analysis is mainly based on interaction between the incident electromagnetic radiation and the present periodic structure. Such interaction can be described based on the well-known characteristic matrix method [20–27]. As mentioned before, the current smart window is designed by using one-dimensional superconductor metallic PCs in the form of $(AB)^N$. Whereas, the superconducting material is labeled as layer A with thickness d_1 and the metal is denoted as layer B with thickness d_2. Then, the periodicity of the structure is set for N times as shown in Fig. 1. The refractive index of the superconductor layer is frequency dependent and varies with its operating temperature (T) according to the two-fluid model [23]:

$$n = \sqrt{\varepsilon_r} = \sqrt{\left(1 - \frac{c^2}{\omega^2 \lambda_L^2}\right)} \tag{1}$$

where λ_L is London penetration depth which can be given by:

$$\lambda_L(T) = \frac{\lambda_0}{\sqrt{1 - \left(\frac{T}{T_c}\right)^2}} \tag{2}$$

where T_c is the critical temperature and λ_0 is the penetration depth at 0 K. In this analysis we assumed that the incident electromagnetic waves propagate in x-direction as indicated in Fig. 1 and electric field component is written according to the characteristic matrix method as:

$$E = E_j(z)\exp(\omega t - \sigma x) \tag{3}$$

where ω is the angular frequency of the electromagnetic waves and σ is the component of the wave vector in

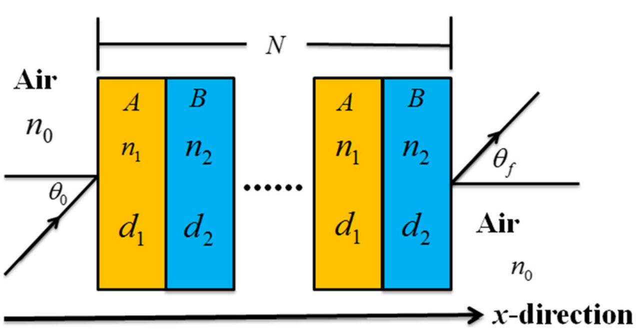

Fig. 1 Schematic diagram of the one-dimensional superconductor metallic PCs which consists of layers A and B for N periods. Then, the whole structure is immersed through air

x-direction Then, the electric and magnetic fields through a given layer j can be written as:

$$\begin{aligned} E_j(z) &= A_j \exp(-ik_j x) + B_j \exp(ik_j x) \\ H_j(y) &= -\frac{k_j}{k_0}(A_j \exp(-ik_j x) - B_j \exp(ik_j x)) \\ k_j &= k_0 n_j = (\omega/c) n_j \end{aligned} \tag{4}$$

therefore, the interaction among the incident electromagnetic waves and each layer in our periodic structure is described using the following matrix:

$$M_j(k,\delta) = \begin{pmatrix} \cos(k_j\delta_j) & -(i/p_j)\sin(k_j\delta_j) \\ -ip_j\sin(k_j\delta_j) & \cos(k_j\delta_j) \end{pmatrix} \tag{5}$$

where $M_j(k,\delta)$ is the characterized matrix for the jth layer, $\delta_j = d_j n_j \cos\theta_j$ and $p_j = n_j\cos(\theta_j)$ for TE mode, $p_j = \frac{\cos(\theta_j)}{n_j}$ for TM mode and θ_j is the angle of incidence.

Thus, we can describe the interaction between the whole periodic structure and the incident electromagnetic waves using the upcoming matrix:

$$M = \begin{pmatrix} M_{11} & M_{12} \\ M_{21} & M_{22} \end{pmatrix} = (M_A M_B)^N \tag{6}$$

Then, the transmittance values due to this interaction could be described as:

$$T = \frac{p_f}{p_0}\left|t^2\right| \tag{7}$$

where $\left(p_{0,f} = \sqrt{\frac{\varepsilon_0}{\mu_0}} n_{0,f}/\cos\theta_{0,f}\right)$ and t is transmittance coefficient that can be described as a function of the matrix elements of (5) as:

$$t = \frac{2p_0}{(M_{11} + M_{12}p_f)p_0 + (M_{21} + M_{22}p_f)} \tag{8}$$

3 Results and Discussions

In this section, the numerical results of the novel smart window are executed to work at the wavelength regions from visible to near infrared (IR). Here, the numerical results summarize the transmittance values due to the interaction between the incident electromagnetic waves and the current structure for oblique incidence. In the one-dimensional superconductor metallic PCs, layer A is set to be $YBa_2Cu_3O_7$ [23] with thickness $d_1 = 230$ nm, critical temperature $T_c = 93$ K, operating temperature $T = 92$ K and $\lambda 0 = 145$ nm. The second layer is designed from silver (Ag) [42] with thickness $d_2 = 2$ nm, and the number of periods is equal to 5.

Now, we present the numerical results of our design as follows: first we demonstrate the effect of the angle of incidence on the transmission properties of our structure.